Self-Commissioning and Testing of Synchronous Reluctance Motor Drives

by

Diego Fernando Valencia García

Submitted to the Department of Electrical Engineering, Electronics, Computers and Systems
in partial fulfillment of the requirements for the degree of

Erasmus Mundus Master Course in Sustainable Transportation and Electrical Power Systems

at the

UNIVERSIDAD DE OVIEDO

September 2017

Author . . . .

Certified by . . . .

Sérgio Cruz
Assistant Professor
Universidade de Coimbra
Thesis Supervisor

Certified by . . . .

Fernando Briz
Professor
Universidad de Oviedo
Thesis Supervisor

Self-Commissioning and Testing of Synchronous Reluctance Motor Drives

by

Diego Fernando Valencia García

Submitted to the Department of Electrical Engineering, Electronics, Computers and Systems
on September 1, 2017, in partial fulfillment of the
requirements for the degree of
Erasmus Mundus Master Course in Sustainable Transportation and Electrical Power Systems

Abstract

The self-commissioning of synchronous reluctance motor (SynRM) drives was studied in this work. The main objective was the analysis of standstill identification strategies of the magnetic model of SynRMs. Two experimental techniques based on current injection were adopted and tested for the calculation of the apparent and incremental inductances, considering saturation and cross-saturation effects. Sinusoidal and square wave current injection techniques were applied to two 3 kW SynRMs from different manufacturers, in laboratory conditions, based on a predictive current control strategy. The motors were fed by an inverter with a sequence of sinusoidal and square wave current pulses that are first applied on the rotor d- and q-axes separately, at different dc currents on the q- and d-axes, respectively. The procedure exploits a quasi-standstill condition obtained by imposing fast torque oscillations. The stator flux linkage was estimated by integrating the motor induced voltages. Using the current and flux samples, a polynomial representation of the flux as a function of the current was defined, which allows to calculate apparent and incremental inductances by operating the polynomial functions.

The accuracy of the obtained inductance values was evaluated experimentally in a test rig, running the SynRM drives in torque control mode by a predictive current control (PCC) strategy. The performances of the drives using the parameters from the two self-commissioning strategies was compared based on the current prediction error and the THD of the motor supply currents. Results were not considerably different using either the inductance profile obtained from sinusoidal current injection or square wave current injection tests, but the test and post-processing were more challenging using square waveforms. Sinusoidal current injection test was then chosen as the technique to be applied to a 11 kW ABB SynRM due to its simpler procedure and accurate results. The 11 kW motor was tested under no-load condition and considering restrictions given its higher rated power and current. The adopted strategy is simple and can be performed at stand-still by injecting a proper current stimulus.

Moreover, it does not require any additional hardware and the motor can be coupled or not to the mechanical load. Finally, the thesis concludes with future prospects for further investigation.

Key words

Synchronous reluctance motor drives, Predictive current control, Self-commissioning, Apparent and incremental inductances, Saturation and cross-saturation, Current injection test.

Thesis Supervisor: Sérgio Cruz
Title: Assistant Professor
Universidade de Coimbra

Thesis Supervisor: Fernando Briz
Title: Professor
Universidad de Oviedo

Acknowledgments

I would first like to thank my thesis supervisors, Prof. Sérgio Cruz and Prof. Fernando Briz, for their support and guidance. I am very grateful to Prof. Sérgio Cruz for his constant feedback and for his steering in the right direction whenever he thought I needed it; the door of his office was always open whenever I ran into a trouble spot or had a question about my research or writing. My gratitude to Prof. Fernando Briz for his detailed revision, meticulous comments and constructive feedback of the thesis document.

Besides my advisors, I would like to thank Hazem Hadla for his constant help, suggestions and clarification about my thesis topic. Every result described in this thesis was accomplished with his help and support. I greatly benefited from his keen scientific insight, his knack for solving practical difficulties and, specially, his ability to put complex ideas into simple terms.

Finally, I must express my very profound gratitude to my friends and family who supported me during my master thesis. To my friends José Pablo, Milos and Froy for their help, suggestions, the stimulating discussions and for all the fun we have had in the last two years. To my Mom, Dad, to Adriana and Melissa, for providing me with unfailing support and continuous encouragement throughout my years of study and through the process of researching and writing this thesis. This accomplishment would not have been possible without them.

Contents

List of Figures

List of Tables

Chapter 1

INTRODUCTION

1.1 Definition and relevance of self-commissioning

Self-commissioning of an electric drive is defined as the ability of the control strategy to identify the machine connected to it without any user intervention or additional equipment [1]. Machine identification refers to the accurate calculation of the parameters by the control itself prior to the normal drive operation. It is useful in situations where the machine and the drive are made by different manufacturers. It is also applicable when one of the elements, machine or power converter, presents a failure and needs to be replaced. In these cases, the time and resources spent before the drive starts or returns to normal operation will depend on the ability of the control strategy to recognise the connected motor. This ability to track regularly the parameters of the machine makes self-commissioning also applicable in fault detection. If some of these parameters change significantly, an early fault condition can be detected. Moreover, any closed-loop control strategy and its performance will rely on the accurate knowledge of these parameters. For instance, a torque control loop, especially used for traction applications such as electric and hybrid electric vehicles, depends on the torque estimation since torque sensors are not commonly used in drive systems [2]. Thus, the process of calculating the parameters is a critical issue in any electric drive system.

In the case when electrical parameters for a certain machine are previously known from the manufacturer or obtained by traditional commissioning tests, it is well-known that they change according to the ambient and working conditions such as the power source, the harmonic content, load conditions, temperature, age and so on. Therefore, these parameters need to be known through techniques sensitive enough to determine variations even in motors with the same nameplate data, and they must be determined in the specific operative conditions, that is, using on-site identification methods.

On-site identification tests present practical restrictions such as the spent amount of time and resources, along with the need of additional equipment or measurement devices and the impossibility to uncouple the machine from the load [3]. Therefore, the drive would have to perform this test without user intervention or additional equipment, in an automatic way; that is, the drive has to apply a self-commissioning test, while guaranteeing a fast, reliable and efficient parameters tracking.

Fig. 1.1 shows a classification proposed in [4] for different parameter identification techniques. It is worth to notice that on-line estimation is also applicable for practical on-site parameter estimation, and it is used during continuous operation, but it requires higher computational load. This thesis project is only concerned about offline self-commissioning applied at standstill and with no power flow between the machine and the load. The off-line methods are classified according to the software and hardware required. The self-commissioning relies only in the own power converter to complete the task. Its main advantages, as stated, are the fast and accurate adjust-

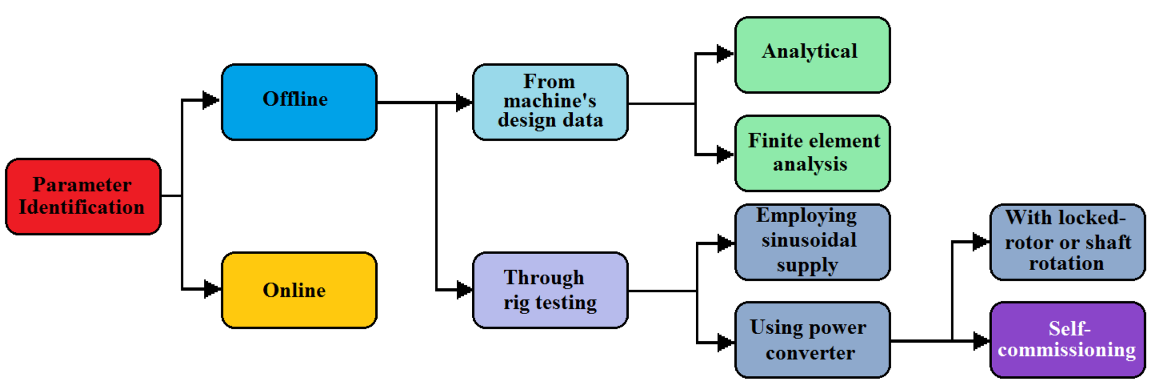

Figure 1.1. Classification of parameter identification techniques of PMSMs [4]

ment of the drive parameters used by the control system, with no special knowledge about machine construction nor additional hardware [5].

1.2 Synchronous reluctance motors

Despite induction motors (IMs) have been the most popular choice for commercial and industrial applications, new technologies and applications, such as hybrid and electric vehicles, are directing more attention in the use of interior permanent magnet synchronous motors (IPMSMs). These machines offer superior properties, particularly higher efficiency, constant power operation and wide speed range. However, they contain NdFeB permanent magnets with rare-earth materials such as neodymium and dysprosium. China holds monopoly, producing 90 % of the rare-earth permanent magnets, and it has approximately 50 % of the earth's known Nd reserves [6]. Therefore, there is a possibility of limited supply or very high cost of these magnets that could make IPMSMs unavailable or too expensive [7]. In addition, permanent magnets can suffer demagnetisation at high temperatures, and they are fragile under high stress due to centrifugal forces, making IPMSMs less robust for high speed or overloading operation.

Over the past few years, the search for an intermediate option between the high efficiency and high power density of IPMSMs and the low cost and high robustness of IMs have attracted growing attention towards synchronous reluctance motors (SynRMs). In contrast to IPMSMs, SynRMs do not use permanent magnets, and therefore the material costs are lower while the dependence of rare-earth magnets is eliminated. Moreover, the enhanced rotor robustness avoids concerns about demagnetisation at high temperatures and withstands higher centrifugal forces [8]. In comparison with IMs, SynRMs rely on the elimination of copper losses which results in higher rated torque for a given size. They also permit a higher overload capability, power density and operation with high efficiencies. However, to achieve these performance characteristics a high saliency ratio must be obtained from the rotor construction, increasing the complexity in the manufacture process [9–15].

Another important issue of SynRMs is the increased control complexity due to their highly non-linear flux linkage to current relationship, caused by magnetic saturation. To represent this non-linear magnetic behaviour, the model must include not only the saturation of the direct (d) and quadrature (q) inductances with the self axis current, but also the sensitivity to the cross-axis current called cross-saturation [8]. An accurate representation of these phenomena can enhance the controller performance, allowing the SynRM to work with optimum torque density, efficiency, dynamic response and flux weakening capability. Therefore, it is important that end users have the possibility to identify this model, to include the inductances behaviour within the control system when the motor is sold as a separate entity from the drive. Moreover, to maintain the use of SynRMs attractive, this identification process should not represent an additional investment in equipment or human resources, and it should be easy to implement with enough accuracy. These requirements match with the concept of self-commissioning, which can be adapted to identify the magnetic parameters in SynRMs.

1.3 Thesis outline

The thesis work presents the self-commissioning of SynRM drives controlled using a predictive control strategy. Signal injection methods are adopted based on sinusoidal current injection and square wave current injection tests. These current injection techniques are applied to identify the flux linkage to current relationship by taking advantage of the current minimisation approach in predictive current control.

Cross-magnetisation characteristic is also considered during the test by the injection of cross-axis dc currents, allowing to obtain different flux curves per each applied dc current value. Estimated flux curves are represented by polynomials in order to determine easily the inductance profiles. The methods are applied to two different synchronous reluctance motors, and the apparent, self-incremental and cross-incremental inductances for each motor are identified. The accuracy of the inductance profile obtained with each technique is evaluated experimentally in laboratory conditions with a test rig. Each motor is run in torque control mode by a predictive current control strategy set with the obtained parameters. This evaluation is done based on the the effects of accuracy in the parameters on the prediction error of the d and q-axis currents as well as the total harmonic distortion during the drive operation. The results within the two current injection techniques are compared in terms of the accuracy and complexity of the test. One technique is chosen and applied to a 11 kW SynRM to be used for traction applications.

The organisation of the thesis per chapter follows the next guideline:

Chapter 2 introduces the concepts and brief history of SynRMs. Mathematical model of SynRM is then described along with the equivalent circuit representation and the non-linear magnetic characteristics. Here, the concepts of apparent, self-incremental and cross-incremental inductances are defined. In addition, a brief description of control techniques applied to SynRMs is done, and the main concepts of predictive control are defined, highlighting the predictive current control (PCC) strategy used in the thesis.

Chapter 3 presents the state-of-the-art of self-commissioning applied to SynRMs. Two methods allowing an accurate inductance identification at standstill are adopted. The application of the chosen techniques based on a PCC strategy is described along with the details of the flux estimation method. Post-processing methodology regarding the polynomial representation of flux curves and calculation of inductances is also explained.

Chapter 4 describes the implementation of the adopted self-commissioning techniques in laboratory conditions. Sinusoidal and square wave current injection tests of two 3 kW SynRMs are described along with the post-processing for flux estimation and inductances calculation. The experimental accuracy evaluation of the obtained parameters on the test rig is explained detailing the setup for operating the motor in torque control mode. This test is aided by an auxiliary drive operating in speed control mode. Finally, sinusoidal current injection technique is chosen to be applied to a 11 kW SynRM. Given the higher rated values in the motor nameplate, hardware limitations and restrictions are considered for the test. Results and preliminary accuracy evaluation are explained.

Chapter 5 presents the conclusions of the thesis and summarises main recommendations for self-commissioning of SynRM drives. It also makes suggestions for future work.

Chapter 2

THEORETICAL BACKGROUND AND CONTROL OF SynRMs

The concept of a SynRM was initially presented by J. K. Kostko in 1923. It was known as a reaction synchronous machine with a reluctance torque and sinusoidal magnetomotive force (MMF) produced by means of the same stator of induction motors [16]. Originally, even though SynRMs had the potential to overhaul IMs, they were not considered for practical applications because a cage winding for the start-up was needed under grid connection. This cage caused a reduction on the saliency ratio, power factor and efficiency of the machine, thus, reverting its main benefits over other kind of AC machines [17].

Later, developments in semiconductors and solid-state inverter technologies revealed the possibility to overcome the above-mentioned drawbacks, making SynRM an interesting target for research. Different works led to improvements in design and control techniques such as closed-loop control of SynRM, in such a way that it was operated with relatively high power and torque density values [9–11, 18–20]. This brought new possibilities in the application of SynRMs for actual technologies, making them more attractive in terms of cost and power density. Nowadays, SynRM drives can be considered a strong option for applications such as HEVs and EVs due to their power density advantage over IMs, and due to their rotor structure without rare-earth magnets [2, 21, 22].

To take advantage of the improved features of SynRMs, a good control strategy is necessary. This implies an accurate knowledge of its parameters under different operating conditions. Therefore, a mathematical model of the SynRM must be accurately defined considering different non-linearities present during its operation.

2.1 Operation principle and dynamic model of SynRMs

SynRMs follow an operational principle similar than the one in conventional salient pole synchronous motors, considering a sinusoidal rotating magnetic field produced in the stator windings, which links the rotor through the airgap. The difference is in the rotor construction, which does not have windings but steel segments with small flux barriers, as it is shown in Fig. 2.1. It is designed to have rotor paths for the flux with different reluctances, one avoiding all flux barriers, with high permeability and low reluctance, the direct (d) axis (Fig. 2.1(a)). The axis in quadrature (q-axis) has low permeability and higher reluctance (Fig. 2.1(b)) due to the flux barriers. Both define the dq reference frame, as shown in Fig. 2.1(c) [8, 23].

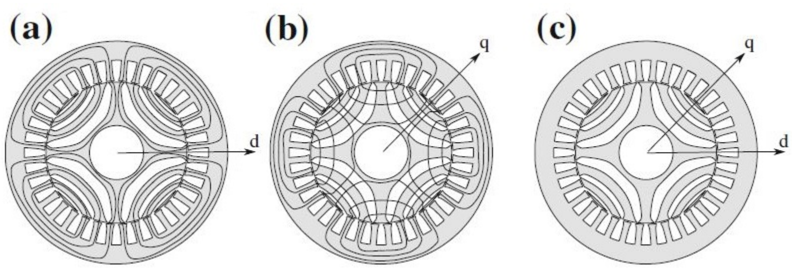

Figure 2.1. Schematic representation of a synchronous reluctance motor: (a) d-axis flux lines; (b) q-axis flux lines and (c) dq reference frame [8]

The objective with this construction is to increase the reluctance torque by increasing the difference between the two magnetising inductances, $(L_d - L_q)$ of the dq-axis in a rotor reference frame; this difference depends on the rotor construction, which is defined by a factor called the saliency ratio, represented by (2.1) [14].

$$\xi = L_d/L_q \tag{2.1}$$

SynRMs are attempted to have high saliency ratios to improve the torque generation capacity along with the torque density and efficiency, thus, different shapes of the rotor laminations are considered for the construction of its anisotropic structure. A traditional rotor structure is illustrated in Fig. 2.2(a) while Fig. 2.2(b) shows one rotor geometry to increase the magnetic saliency above the levels achievable with conventionally-laminated machines. This consists on laminate it in the axial direction using ferromagnetic strips that are separated by thin layers of insulating material [8]. Its major advantage is the possibility to increase significantly the amount of flux barriers per pole and the magnetic saliency, achieving ratios higher than 10 [14]. Unfortunately, iron losses specially affect axially laminated construction, limiting the efficiency advantages of the SynRM itself. In addition, the manufacture process is challenging and expensive, reducing their commercial possibilities.

As a solution, Fig. 2.2(c) shows a transversally laminated anisotropic (TLA) rotor design. This rotor is easier to manufacture and generates relatively low iron losses, being generally preferred for automotive applications even when the saliency ratio $\xi < 10$ [14].

The dynamic model of the SynRM is represented by the voltage model in a dq reference frame, synchronous to the rotor. This is presented in (2.2).

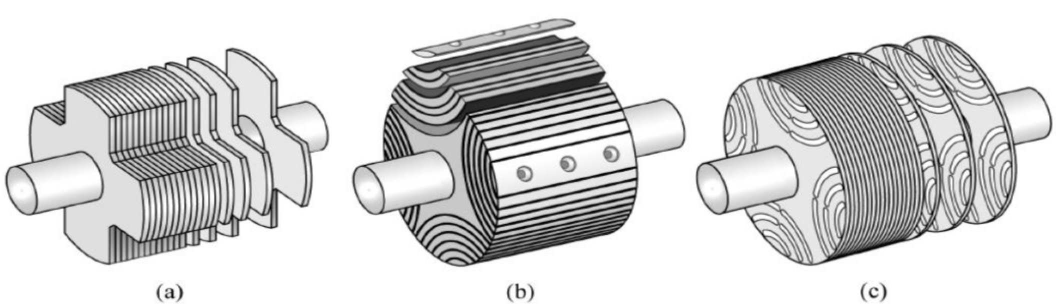

Figure 2.2. Different anisotropic structures of the rotor in SynRMs: (a) traditional lamination, (b) axially laminated anisotropic rotor, (c) transversally laminated anisotropic rotor (TLA) [14].

$$
\begin{aligned}
v_d &= R_s i_d + \frac{d\lambda_d}{dt} - \omega_e \lambda_q \\
v_q &= R_s i_q + \frac{d\lambda_q}{dt} + \omega_e \lambda_d,
\end{aligned}
\tag{2.2}
$$

where v_d and v_q are the stator voltages, i_d and i_q the stator currents, λ_d and λ_q the stator flux linkages, and ω_e the electric angular rotor speed. Fig. 2.3(a) shows the equivalent circuit based on (2.2), but only reported for the d-axis, while the equivalent q-axis representation can be obtained in similar way. This model represents the effects of copper losses through the stator resistance R_s, but neglects iron losses due to hysteresis and eddy currents for simplicity. The influence of the iron losses on the transient behaviour of the motor is usually neglected, but it is important to consider that its effect, for the commissioning task, might lead to inaccuracies for inductance calculation. Fig. 2.3(b) shows an equivalent circuit representation including an additional resistance for iron losses representation [24].

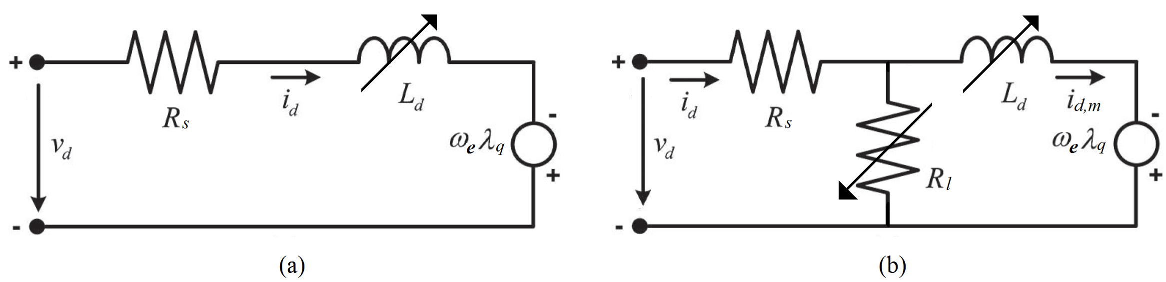

Figure 2.3. SynRM d-axis equivalent circuit: (a) with copper losses only; (b) with copper and iron losses

The rotor mechanical rotation is related to the number of poles of the motor, given by (2.3)

$$\theta_e = p\theta_m, \tag{2.3}$$

where θ_e is the electric rotor angle, θ_m is the rotor angle and p is the number of pole pairs of the machine. This derives into (2.4)

$$\omega_e = p\omega_m, \tag{2.4}$$

where ω_m is the rotor angular speed.

Based on (2.2), the torque produced in the electromechanical energy conversion process is given by (2.5)

$$T_e = \frac{3}{2}p(\lambda_d i_q - \lambda_q i_d), \tag{2.5}$$

To complete the overall modelling of the machine, the mechanical model is given by (2.6)

$$T_e = J\frac{d\omega_m}{dt} + B\omega_m + T_L, \tag{2.6}$$

where J is the constant of inertia, B is the viscous friction coefficient and T_L is the load torque.

Conventionally, a first approximation of the model given in (2.2) involves the assumption of a linear model representing the magnetic circuit. In practice, the iron core can sustain a certain flux level beyond which it saturates, and any increase in the current will not produce significant flux increments. It means that the flux linkage and the current can only be accurately represented by a non-linear relationship. In addition, the currents in the two orthogonal axes interact through a common ferromagnetic core, affecting the flux and, hence, inductance in the perpendicular axis; this causes redistribution of flux due to core saturation and is called the *cross-saturation* effect [3]. Thus, the flux cannot be modelled by means of a single-variable-dependent function. In fact, each one of the fluxes λ_d and λ_q is dependent on both dq current components at the same time, establishing the 2-dimensional general relations in (2.7) [8, 25, 26].

$$\begin{aligned} \lambda_d &= \lambda_d(i_d, i_q) \\ \lambda_q &= \lambda_q(i_d, i_q) \end{aligned} \tag{2.7}$$

The magnetic model can also be represented by an alternative form, by introducing specific inductance concepts, suitable for control purposes due to the easiness of the mathematical formulation. First, the apparent inductance L^{app} is introduced and defined by (2.8).

$$L^{app} = \begin{bmatrix} L_d^{app}(i_d, i_q) & L_{dq}^{app}(i_d, i_q) \\ L_{qd}^{app}(i_d, i_q) & L_q^{app}(i_d, i_q) \end{bmatrix} = \begin{bmatrix} \frac{\lambda_d(i_d,i_q)}{i_d} & \frac{\lambda_d(i_d,i_q)}{i_q} \\ \frac{\lambda_q(i_d,i_q)}{i_d} & \frac{\lambda_q(i_d,i_q)}{i_q} \end{bmatrix} \tag{2.8}$$

The main-diagonal terms in (2.8) define the apparent inductances as the ratio between the flux linkage and the corresponding current on the same axis, specified for a given operating point. The apparent inductances represent the magnetic flux level of the machine in a specific operating point defined by (i_d, i_q) and, therefore, they are used for large-signal representations of the SynRM electromagnetic circuit [27]. The off-diagonal terms in (2.8) demarcated as a ratio between the flux linkage and the current on the orthogonal axis, L_{dq}^{app} and L_{qd}^{app}, represent the effect of cross-saturation over the inductances; they are called cross-apparent inductances and can be neglected due to their low values with respect to the self-apparent inductances L_d^{app} and L_q^{app}. Alternatively, the effects of these inductances can be included in $L_d^{app}(i_d, i_q)$ and $L_q^{app}(i_d, i_q)$.

The substitution of (2.8) in (2.2) leads to:

$$\begin{aligned} v_d &= R_s i_d + \left[\frac{\partial \lambda_d(i_d, i_q)}{\partial i_d}\frac{di_d}{dt} + \frac{\partial \lambda_d(i_d, i_q)}{\partial i_q}\frac{di_q}{dt}\right] - \omega_e\left(\lambda_q(i_d, i_q) + \lambda_{qd}(i_d, i_q)\right) \\ v_q &= R_s i_q + \left[\frac{\partial \lambda_q(i_d, i_q)}{\partial i_d}\frac{di_d}{dt} + \frac{\partial \lambda_q(i_d, i_q)}{\partial i_q}\frac{di_q}{dt}\right] + \omega_e\left(\lambda_d(i_d, i_q) + \lambda_{dq}(i_d, i_q)\right) \end{aligned} \tag{2.9}$$

This allows to define the partial derivatives of the flux linkage components as the *incremental inductances* according to (2.10).

$$L^{inc} = \begin{bmatrix} l_d^{inc}(i_d, i_q) & l_{dq}^{inc}(i_d, i_q) \\ l_{qd}^{inc}(i_d, i_q) & l_q^{inc}(i_d, i_q) \end{bmatrix} = \begin{bmatrix} \frac{\partial\lambda_d(i_d,i_q)}{\partial i_d} & \frac{\partial\lambda_d(i_d,i_q)}{\partial i_q} \\ \frac{\partial\lambda_q(i_d,i_q)}{\partial i_d} & \frac{\partial\lambda_q(i_d,i_q)}{\partial i_q} \end{bmatrix} \tag{2.10}$$

The incremental inductances represent the rate of change of the magnetic flux of the motor with respect to the two variables i_d and i_q in a specific operating point. Thus, they carry the information on the small-signal or transient behaviour of the motor [27].

Fig. 2.4 shows a typical flux curve along with the graphical representation of apparent and incremental inductances. The apparent inductance is illustrated as the slope of the linearised characteristic of flux linkage versus current, which goes through the origin and a given operating point, while the incremental inductance is represented as the slope of the line tangent to the operating point.

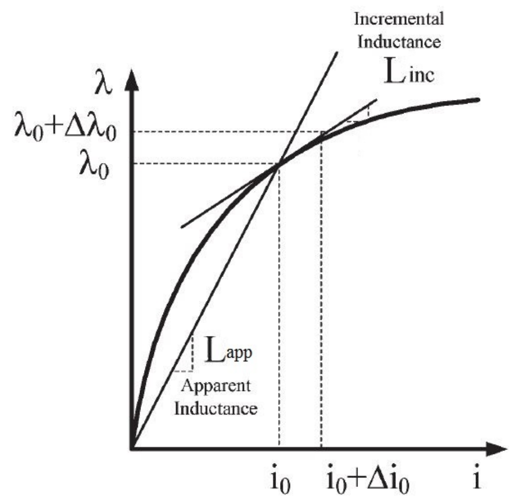

Figure 2.4. Definition of apparent and incremental inductances [28]

Considering the definition in (2.10) and neglecting the cross-apparent inductances, the expression (2.9) can be written as [29]:

$$\begin{aligned} v_d &= R_s i_d + l_d^{inc}(i_d, i_q)\frac{di_d}{dt} + l_{dq}^{inc}(i_d, i_q)\frac{di_q}{dt} - \omega_e\left(L_q^{app} i_q\right) \\ v_q &= R_s i_q + l_{qd}^{inc}(i_d, i_q)\frac{di_d}{dt} + l_q^{inc}(i_d, i_q)\frac{di_q}{dt} + \omega_e\left(L_d^{app} i_d\right) \end{aligned} \tag{2.11}$$

The previous definitions allow to define the torque equation as a function of the apparent inductances as (2.12).

$$T = \frac{3}{2}p(L_d^{app} - L_q^{app})i_d i_q \tag{2.12}$$

Although the equivalent circuit of SynRMs is simpler than the one of conventional induction motors due to the absence of rotor currents, there is a challenge in the characterisation of their magnetic model. It is characterised by the difference between the d- and q-axis inductances. Moreover, these inductances are not constant, and apparent and incremental inductances should be considered, as well as the self- and cross-saturation phenomena in each of them. These components influence directly the performance of a dq axis-based control scheme and the accurate prediction for the output torque, power factor and stable region of operation, in particular, for those applications centred in a constant-power speed range such as EVs [30]. Given that the relationship between flux linkage and currents is highly nonlinear, accurate control techniques cannot be adopted without taking it into account, otherwise, it could cause significate errors in the prediction of torque capability compared with the real motor [30–33].

2.2 Predictive control of SynRMs

Regarding control strategies for electric drives, the most common are linear PI controller based rotor field oriented control (RFOC) and hysteresis based direct torque control (DTC). Field oriented control is a method for controlling ac machines by representing their dynamic behaviour by a dc equivalent system. The main complexity in RFOC lies in estimating the rotor flux angle for coordinate transformation based on the model of the machine which is very sensitive to the machine parameters. Furthermore, the dynamic response is limited by the bandwidth of inner current loop and the cascaded structure demands tuning to achieve good performance [34]. Meanwhile, direct torque control is based on the bind of torque and flux errors in hysteresis bands by selecting the switching states of the inverter. The hysteresis band invariably leads to variable switching frequency operation. The drawback of DTC in the digital implementation is the need of very high sampling frequency to prevent high torque ripples that could affect the motor lifetime [35]. Recently, new control schemes such as fuzzy logic, neural networks, sliding mode control and predictive control have been considered based on a technological impulse from more powerful microprocessors.

A predictive control strategy uses a model of the system to predict the future behaviour of the controlled variables and obtain an optimal response according to a defined criterion. The predictive control methods can be classified in deadbeat control, hysteresis based control, trajectory based control and model predictive control (MPC) [36]. This thesis work is based in a MPC strategy previously implemented in [34]. This strategy uses a more flexible optimisation-based approach which computes the next control action by the minimisation of a cost function. This cost function is the difference between the predicted output of a system and the specified reference. This can take two different schemes: MPC with continuous control set or MPC with finite control set. The focus here is over the latest scheme, which predicts the system response for all possible switching states in the power converter given their discrete nature. Then, it generates the switching pulses corresponding to the voltage vector that minimises the cost function and applies them in the next sampling instant. Consequently it does not require a modulator and hence presents a variable switching frequency [37, 38].

The implemented MPC uses predictive current control (PCC) by setting the stator currents in the dq synchronous rotor reference frame as control variables. The block diagram of this control strategy is shown in Fig. 2.5. Unit delay compensation is applied to reduce torque and flux ripples caused by the delay in the processor due to the large number of calculations involved [39]. The estimated currents at instant $(k+1)$ are represented by $\hat{i}_d$ and $\hat{i}_q$ based on a forward Euler discretisation according to (2.13) [40, 41].

$$\begin{aligned}\hat{i}_d(k+1) &= i_d(k) + \frac{T_s}{\delta l^{inc}}(v_d(k) - R_s i_d(k) + \omega_e \lambda_q(k)) \\ &\quad - \frac{T_s}{\delta l^{inc}} \frac{{l_{dq}}^{inc}}{{l_q}^{inc}}(v_q(k) - R_s i_q(k) + \omega_e \lambda_d(k)) \\ \hat{i}_q(k+1) &= i_q(k) + \frac{T_s}{l_q^{inc}}(v_q(k) - R_s i_q(k) - \omega_e \lambda_d(k)) \\ &\quad - \frac{T_s}{{l_q}^{inc}} \frac{{l_{dq}}^{inc}}{T_s}(\hat{i}_d(k+1) - i_d(k)),\end{aligned} \tag{2.13}$$

where $i_d(k)$ and $i_q(k)$ are the measured stator currents, v_d and v_q are the voltage vectors applied at instant k, T_s is the sampling period and δl^{inc} is defined in (2.14). The applied voltage is not measured directly but calculated from the measured DC

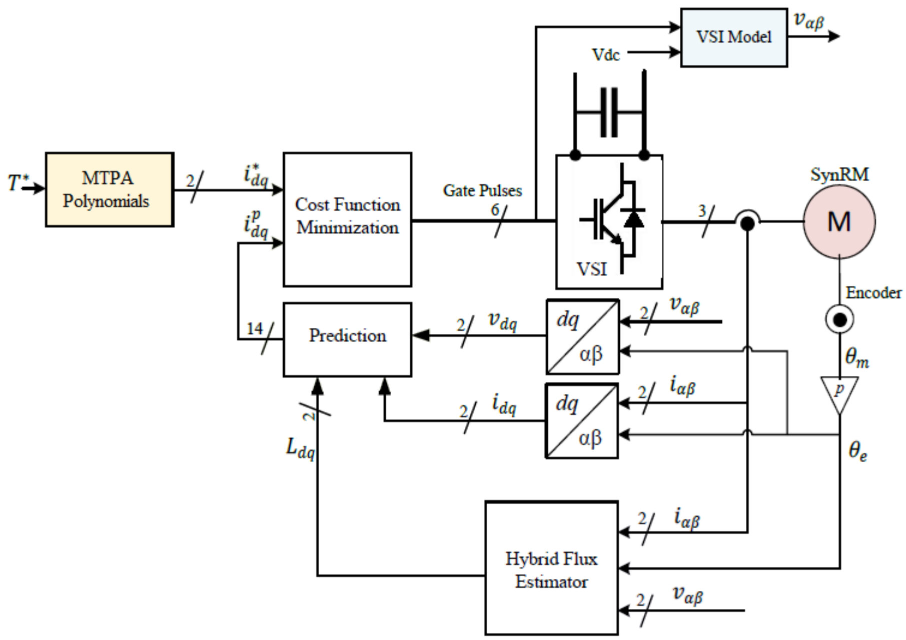

Figure 2.5. Predictive current control block to use in the self-commissioning tests [34]

link voltage and switching state of the inverter.

$$\delta l^{inc} = l_d^{inc} - \frac{l_{dq}^{inc} l_{qd}^{inc}}{l_q^{inc}} \tag{2.14}$$

The currents for instant *k+2* are predicted then for each one of the different voltage vectors that can be applied to the motor, using the equations presented in (2.13)-(2.14), shifted one sample ahead.

The cost function for the predictive current control is defined in (2.15). It consists of the squared error between the predicted stator currents, i_d^p and i_q^p, and the reference values, i_d^* and i_q^*, for the d- and q-axis. The voltage vector that minimises the cost function is chosen and the corresponding switching pulses are sent to the inverter at the next sampling instant.

$$G = (i_d^* - i_d^p(k+2))^2 + (i_q^* - i_q^p(k+2))^2 \tag{2.15}$$

The hybrid flux estimator in Fig. 2.5 is used to estimate the flux based on both a voltage model and a current model with the inductance values used in look-up tables (LUTs). This was implemented in [34] because the flux estimation with voltage model is robust at high speeds, but the smaller magnitude of the back-EMF makes the use of the current model a preferred option at low speeds. Therefore, the hybrid flux estimator is developed to exploit the merits of both methods based on the operating speed, avoiding discontinuous transitions between the voltage and current models.

It is worth to notice how the prediction and optimisation process is highly dependent on the accuracy of the parameters, especially of the inductances due to their non-linear behaviour. It highlights the importance of self-commissioning prior the optimal performance of this control strategy.

Chapter 3

SELF-COMMISSIONING OF SynRM DRIVES

This chapter briefly reviews the state-of-the-art of self-commissioning strategies for SynRMs. Given the high nonlinearity of these motors regarding the flux linkage behaviour, the focus is on the calculation of apparent and incremental inductances considering saturation and cross-saturation phenomena. The determination of these inductances is critical for the controller operation because they can significantly vary with respect to the current. It is expected to obtain a smooth decrease in the d-axis inductance (L_d^{app}, l_d^{inc}), while the q-axis inductances (L_q^{app}, l_q^{inc}) are expected to present larger decrease at lower levels of current. The stator resistance is also considered, which is directly measured with an ohmmeter.

3.1 State-of-the-art on self-commissioning for SynRMs

Different identification procedures for the parameters of SynRMs have been considered. Since saturation phenomena is presented in both PMSMs and SynRMs, whatever the type of machine, the magnetic model is generally represented as flux linkage look-up tables, and most of the techniques applied to PMSMs can be adapted to SynRMs. This section considers a literature review of the parameter identification methods applied to SynRMs and some of the latest focused on IPMSMs, which are suitable for SynRMs considering a null PM flux linkage.

Online parameter estimation is commonly used to track continuously the parameter variations during motor normal operation. The control schemes presented in [42–46], for instance, rely on online estimation methods, thus evidencing their main advantage on performance improvement in sensorless control applications.

Regarding the offline methods, according to the classification proposed in [47], the magnetic model of synchronous machines can be identified via finite element analysis (FEA), locked rotor tests, free shaft at constant speed test and high frequency injection.

FEA is commonly applied for parameter identification at an early design stage of the machine. In [48], for instance, various methods to calculate the magnetic model of an IPMSM though FEA are examined. Apparent and incremental inductances are considered, but they do not consider both self-axis and cross-saturation components for the apparent and incremental inductances, or require several nonlinear FEA solutions for each load condition, and therefore, a high computational load and running time. Recently, [23] analytically calculated the electric and magnetic parameters of a SynRM, as a part of a sizing methodology for traction applications; FEA was considered in the validation procedure for the proposed analysis. In [49], the authors applied FEA to determine the self- and cross-coupling components of apparent inductances but neglected the incremental inductances. In general, the main disadvantage of FEA is the requirement of a detailed knowledge about the geometry and magnetic properties of the machine, information which is usually not provided by manufacturers, making this technique impractical for on-site applications. In addition, FEA simulations are not always accurate enough, and they must be eventually validated by experiments [8].

Locked rotor tests simplify the voltage expressions in (2.2) by fixing the shaft speed equal to zero. These methods involve the application of a square-wave voltage in self-axis while a constant current is applied in the orthogonal axis, as it was performed in [50]. In this study, a controlled VSI provided a constant value for d- or q- axis currents, requiring a closed loop control system. At the same time, the current of the opposite axis was changed in a stepwise manner. In this way, saturation and cross-saturation effects on apparent inductances were considered. Incremental inductances were calculated later by the approximation of partial derivatives, considering both self-axis and cross-coupling components. Moreover, stator resistance was computed using the data corresponding to voltage and current in steady-state for each step change. Later, authors in [51] applied this technique by blocking and detecting the initial rotor position, injecting AC current excitation in the self-axis, and short-circuiting the orthogonal axis for computing the apparent inductances with self- and cross-axis components. Differential inductances were also determined by means of high frequency voltage injection.

On the other hand, constant speed methods can estimate the parameters while the motor is running at steady-state, therefore, when the voltage equation is represented in rotor reference frame, considering the derivative terms in (2.2) equal to zero [52]. Then, flux linkages in dq axes can be computed. In the same way as the locked rotor method, the motor under test is dq current-controlled and the currents in d- and q-axes are increased from zero to a maximum value, looking for a complete exploration of the λ versus i relationship [8]. This technique has been applied to SynRMs in [53], in which an analytical model, including core losses and cross-saturation, was tested. In [54], a special sequence of currents feeding the machine was proposed. Thermal variation during the test was suppressed by running the motor in a subsequent motor-brake operation. Nevertheless, since steady-state was considered, incremental inductance effects were neglected. The method was also applied in [12], in which an analytical expression was proposed. The authors run the motor at constant speed and determined the flux linkage as a function of $i_d - i_q$, computing the respective inductances. Then, these inductance values fed a cost function to be minimised fitting the parameters of the proposed model.

Other approach sets the operation point through a pattern of closed-loop-controlled currents as a reference to get a constant motor acceleration [47]. The ramp speed response corresponds to a steady-state torque value and dq constant flux linkage, which causes the derivatives in (2.2) to become zero. The speed response is set to ramp up and down by reversing the i_q current component when maximum speed is reached. This accomplishes the condition of the machine working as a brake and motor, which allows to estimate symmetrically the flux linkage and allows to reduce the errors from terminal voltages estimations and stator resistance.

The main disadvantage of constant speed tests is the need for specific extra hardware, including a controlled prime mover, sometimes a wattmeter, the measurement of pulse-width-modulated machine voltages, etc., according to the adopted technique [55]. In fact, all methods for parameter identification previously mentioned do not meet the requirements and restrictions suitable for self-commissioning, in which it is expected that the parameters are estimated at standstill, with no special arrangements. Thus, the inspection method of the machine impedance considering the aforementioned restrictions has been recently adopted as an advantageous methodology for parameter estimation of SynRM on site [1, 8, 47].

In [3] a self-commissioning method including the effect of saturation and cross-saturation on apparent inductances is presented. The method involves high frequency sinusoidal injection test, with signals that are closed-loop-controlled by a PI current controller tuned *a priori*. Given that conventional PI controllers would require a high bandwidth to handle high frequencies, a PI plus resonant controller (PI-RES) substituted it. In addition, the method requires information about initial rotor position. Stator resistance is computed through a dc injection test along the d-axis, preventing machine rotation; inverter nonlinearity is compensated by applying two levels of current and calculating resistance from the voltage difference.

The high frequency injection method starts by determining the self-axis apparent inductance by injecting the high frequency sinusoidal current in one axis while the other is fed by zero reference. Cross-saturation is computed by applying the same high frequency reference in the self-axis while a dc current is applied to the cross-axis. To prevent rotation during the d-axis test, dc current is replaced by square wave with lower frequency than sinusoidal for the cross-axis reference. Thus, possible shaft rotation is avoided during the test due to the torque generation caused by i_q. Incremental inductances are not mentioned within the developed method.

This technique was later improved in [56] by injecting an ac + dc-biased current in one axis, while the other is set to zero. Cross-saturation is considered correspondingly with the previous methods, by applying a dc signal in the orthogonal axis. Moreover, authors claimed that the method is immune to both stator resistance error and inverter dead-time. The addition of a dc-biased ac injected current is intended to divide the magnetic characteristic curve into infinitesimal sections, analysing each section under the assumption of local linearity. So, inductance is calculated in each section as the slope of the curve caused by the ac waveform. DC-biased component value controls the magnetising state. It improves the overall estimation accuracy of the results compared with the previous method. Incremental inductances are not considered explicitly during the modelling.

In [27], authors claimed, after experimental tests, that the magnetic model proposed in previous works cannot be represented through small-signal injection for the identification of incremental inductances given the inaccuracies appearing when iron losses and other nonlinearities are neglected, even with a high increase in the test voltage amplitude. Instead, a method applying square-wave voltages to the self-axis and constant values to the orthogonal axis is proposed. In this case, square-wave is applied also to the axis with lower magnetic reluctance or largest inductance. Self-axis and cross-saturation components in apparent and incremental inductances were considered.

In 2016, *Bedetti, et. al.* [55] proposed a technique in which the linear least squares (LLS) method was used to fit a piecewise-defined mathematical model to the measured samples. The cross-saturation effect is taken into account by dividing the cross-axis into segments, each of which has its own saturation curve and a set of fitted parameters. The self-commissioning test is thought to avoid the current bias injection and to replace the PI controllers since they require a previous knowledge of drive parameters for a proper tuning. Instead, a hysteresis control is applied, and proper voltage stimulus is injected in each of the two axes separately. The supply current is set with a null average, high frequency (to create a pulsating torque which prevents rotation) and sufficient amplitude to cover the whole current range of the machine. Fig. 3.1(a) shows the square wave voltage applied in d-axis with a zero q-axis current and the correspondent current and estimated flux, while Fig. 3.1(b) illustrates the square wave voltage applied in q-axis with a higher frequency and lower amplitude. During the test, flux linkage at standstill is estimated and a group of cumulative-sum terms are fed for the saturation region. The procedure avoids the storage of all flux and current samples, but it deals with the storage of cumulative-sum terms and post-processing. In addition, an initial guess must be done about the threshold current which determines when the curve starts entering into the saturation region.

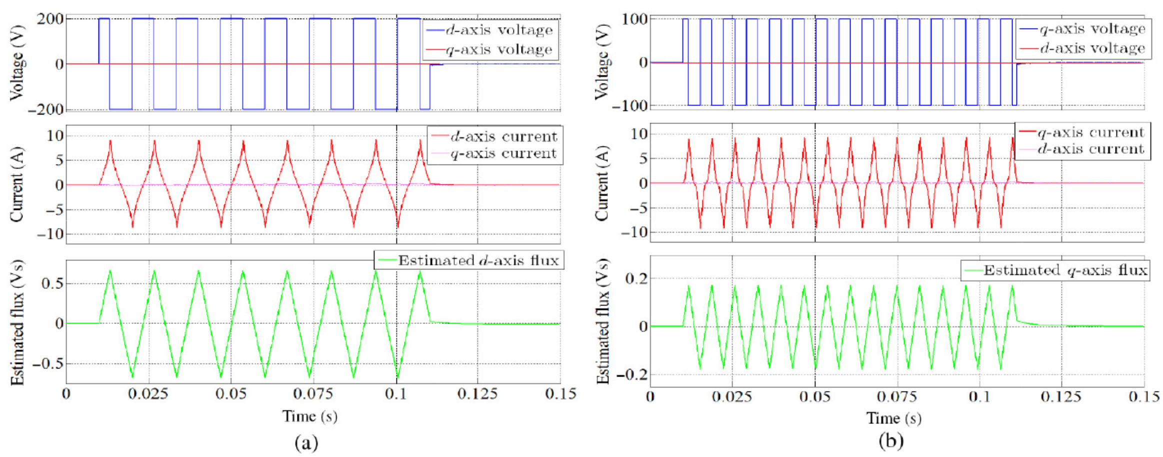

Figure 3.1. Signal sequence adopted for identification of flux curves in [55]. (a) d-axis identification (b) q-axis identification.

In [57], a self-commissioning method is proposed, this includes a similar excitation as the one in figure 3.1, but instead of using the same magnetic model than the one applied in [55], it fits the results to the algebraic magnetic model proposed in [12]. The magnetic model is initially represented, for the d-axis, through a self-axis model by the polynomial function:

$$i_d(\lambda_d) = (a_{d0} + a_{d1}|\lambda_d| + ... + a_{dn}|\lambda_d|^n)\lambda_d, \tag{3.1}$$

where $a_{d0}...a_{dn}$ are the coefficients and n is the highest exponent. The model is simplified in the same way as [12]:

$$i_d(\lambda_d) = (a_{d0} + a_{dd}|\lambda_d|^S)\lambda_d, \tag{3.2}$$

where a_{d0} is the inverse of the unsaturated inductance, S is a positive exponent determining the shape of the saturation characteristics, and a_{dd} is a nonnegative coefficient. Authors chose to fix $S = 5$ arguing it fits the best to the saturation curve representation.

The main benefit of (3.2) is that it can be represented also as an inductance function, which can be eventually differentiated to find the incremental inductances. In the case of the d-axis characteristic, it is:

$$L_{app,d}(\lambda_d) = \frac{\lambda_d}{i_d(\lambda_d)} = \frac{1}{a_{d0} + a_{dd}|\lambda_d|^S} \tag{3.3}$$

$$L_{inc,d}(\lambda_d) = \frac{\partial \lambda_d}{\partial i_d(\lambda_d)} = \frac{1}{a_{d0} + (S+1)a_{dd}|\lambda_d|^S}. \tag{3.4}$$

The aforementioned procedure is also considered for the q-axis case, but applying the equation:

$$i_q(\lambda_q) = (a_{q0} + a_{qq}|\lambda_q|^T)\lambda_q. \tag{3.5}$$

In this case, authors mentioned that since the effective airgap is large along the q-axis, the exponent $T = 1$ is typically used with appreciable accuracy.

For the inclusion of cross-saturation in the algebraic equation, the cross-coupling components are added to the self-axis expressions previously defined, according to:

$$\begin{aligned} i_d(\lambda_d, \lambda_q) &= i_d(\lambda_d, 0) + a'_{dq}|\lambda_d|^U|\lambda_q|^{V'}\lambda_d \\ i_q(\lambda_d, \lambda_q) &= i_q(0, \lambda_q) + a'_{qd}|\lambda_d|^{U'}|\lambda_q|^V\lambda_q, \end{aligned} \tag{3.6}$$

where a'_{dq} and a'_{qd} are nonnegative coefficients and U,U',V and V' are nonnegative exponents. The functions $i_d(\lambda_d, 0)$ and $i_q(0, \lambda_q)$ describe the self-axis saturation characteristics. Applying reciprocity condition, it can be turned into:

$$
\begin{aligned}
i_d(\lambda_d, \lambda_q) &= (a_{d0} + a_{dd}|\lambda_d|^S + \frac{a_{dq}}{V+2}|\lambda_d|^U|\lambda_q|^{V+2})\lambda_d \\
i_q(\lambda_d, \lambda_q) &= (a_{q0} + a_{qq}|\lambda_q|^T + \frac{a_{qd}}{U+2}|\lambda_d|^{U+2}|\lambda_q|^V), \lambda_q
\end{aligned}
\tag{3.7}
$$

where a_{d0}, a_{dd}, a_{q0}, a_{qq}, and a_{dq} are nonnegative coefficients and S,T,U, and V are nonnegative exponents. There are three parameters for the d-axis, three for the q-axis, and three for the cross-saturation. The exponents S,T,U and V were experimentally fitted by the authors for each motor under test. This lets only five parameters remaining, which are estimated using the standard LLS method, reducing the estimation problem to solve a set of linear equations. The inverter nonlinearities are claimed to be omitted since the method is accurate enough without that compensation. The effect of stator resistance is clearly analysed showing the reduced effect over the magnetic model, affecting the hysteresis behaviour. Results showed how the signal injection generates a quasi-standstill condition in the motor, since the rotor did not displace more than 30 electrical degrees.

3.2 Self-commissioning with current injection

The state-of-the-art on self-commissioning of SynRMs deals with current injection along the rotor dq-axes to identify the flux curves representing the magnetic model. These techniques tend to avoid the use of PI controllers due to inaccuracies and time spent during the tuning process. Thus, signal injection method is adopted in this thesis given the advantage of having a system with a predictive current control (PCC) with current minimisation strategy [34]. This is especially convenient for self-commissioning based on signal injection, because additional control tuning is not required. Response based on PCC uses the stator currents in the synchronous reference frame as control variables. These are used to estimate and predict the currents in the instants $k+1$ and $k+2$, and to minimise a cost function consisting on the squared error between the predicted stator currents ($i_d(k+2)$ and $i_q(k+2)$) and the corresponding reference values. Although this control strategy relies on accurate parameters to guarantee motor performance, the errors in current reference tracking are negligible if a rough estimation in the parameters is available.

Two current injection techniques are tested: sinusoidal and square wave current injection.

3.2.1 Sinusoidal current injection

The signal injection test sets a current in one of the d- or q-axes to identify the characteristics of flux linkage in the excited axis. Sinusoidal waveform is chosen for this test because it has a zero-average value. This feature voids to produce a zero-averaged pulsating torque which can avoid rotor movement if the frequency is high enough. In addition, sinusoidal current injection along one of the coordinated axis produces a smooth and continuous response in the flux linkage and therefore allows to calculate continuous values for apparent and incremental inductances. Estimation of the flux linkage assumes that iron losses are negligible, thus representing the coordinated axes by the equivalent circuit in Fig. 2.3(a).

This test considers also the cross magnetisation phenomenon. The sinusoidal current is injected in a chosen axis and, simultaneously, a dc-current is injected in the orthogonal axis. The test is repeated for different values of the dc-current. This allows to obtain one flux curve per applied dc-current level and to reconstruct a flux surface (flux as a function of both d- and q-axis currents) by interpolating the obtained curves.

3.2.2 Square wave current injection

A self-commissioning method based on current injection and including iron losses in the equivalent circuit of Fig. 2.3 is adopted based on [27]. The objective is to apply a current injection method considering that iron losses cannot be neglected in the inductance identification process. This would make inaccurate the flux estimation from the injection of sinusoidal currents. Instead, the injection of a square wave current would allow to make the approximation of $i_d = i_{d,m}$ in the circuit of Fig. 2.3(b) as long as the steady-state condition is reached in the flux estimation. The amplitude of the applied square wave current defines the only discrete points along the flux curve, therefore different amplitudes must be considered to explore the whole identification range. Then, the flux curve is reconstructed by connecting the different points calculated before.

Cross-magnetisation is considered using the same process as the sinusoidal current injection test. The flux curves for different cross-axis dc currents are calculated and the flux surfaces are reconstructed by interpolation between the curves. In other words, the estimation of the λ_d is obtained with square-wave current references for i_d and constant references for i_q, while the estimation of λ_q is obtained with square-wave current references for i_q and constant references for i_d.

3.2.3 Flux linkage estimation

Once it is possible to make the system following a reference current in a rotor reference frame, it is necessary to determine the variation of flux linkage along both d- and q-axes. For this, an approximate voltage model is considered according to the SynRM mathematical model, considering a standstill condition. This condition allows to neglect the speed transients components and to compute the flux as the integral of the voltage minus the voltage drop across the stator resistance, as shown in the block diagram of Fig. 3.2.

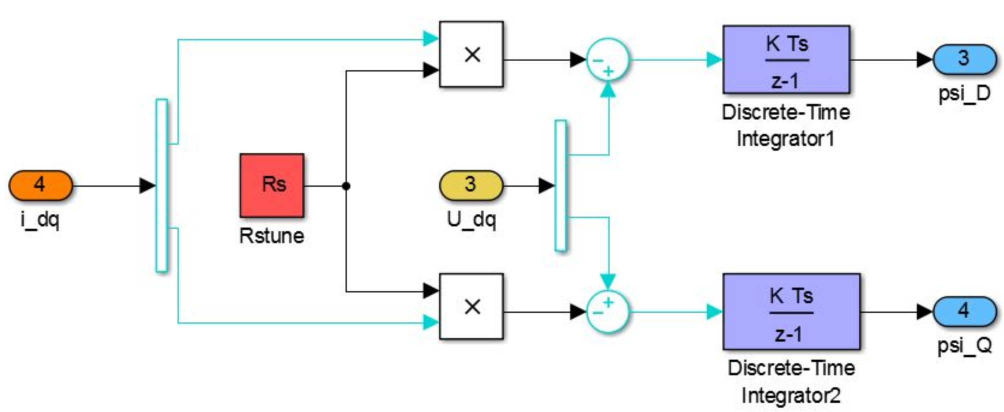

Figure 3.2. Stator flux estimation using a voltage model

3.2.4 Identification of apparent and incremental inductances using polynomial representations

Once the fluxes and currents in each d- and q-axes have been identified, it is possible to determine the apparent inductances based on its definition in section 2. However, the use of (2.8) causes a division by zero problem for low values of currents. To avoid this problem, the flux surfaces are approximated by polynomials according to (3.8) [58].

$$\begin{aligned}\lambda_d(i_d, i_q = const) &= a_0(i_q = const) + \sum_{k=1}^{n} a_k(i_q = const) i_d^k \\ \lambda_q(i_d = const, i_q) &= b_0(i_d = const) + \sum_{k=1}^{m} b_k(i_d = const) i_q^k,\end{aligned} \tag{3.8}$$

where a_0,, a_k, b_0 and b_k are the polynomial coefficients. From (2.8) and (3.8), the polynomial representation of the parameters is given in (3.9).

$$\begin{aligned}\lambda_d = \lambda_{d,0} + L_d i_d &= a_0(i_q = const) + \sum_{k=1}^{n} a_k(i_q = const) i_d^k \\ \lambda_q = \lambda_{0,q} + L_q i_q &= b_0(i_d = const) + \sum_{k=1}^{m} b_k(i_d = const) i_q^k,\end{aligned} \tag{3.9}$$

where $\lambda_{d,0}$ and $\lambda_{0,q}$ are the d- and q-axis current dependent flux for $i_q = 0$ and $i_d = 0$ respectively. These values are theoretically zero for SynRMs while depends on the magnet flux for PMSMs. Then, the polynomial representation can be split as (3.10) to get the apparent inductance in (3.11).

$$\begin{aligned}L_d i_d &= \sum_{k=1}^{n} a_k(i_q = const) i_d^k \\ L_q i_q &= \sum_{k=1}^{m} b_k(i_d = const) i_q^k\end{aligned} \tag{3.10}$$

$$
\begin{aligned}
L_d(i_d, i_q = const) &= \sum_{k=1}^{n} a_k(i_q = const) i_d^{k-1} \\
L_q(i_d = const, i_q) &= \sum_{k=1}^{m} b_k(i_d = const) i_q^{k-1}.
\end{aligned}
\tag{3.11}
$$

Incremental inductances can be calculated from 3.9 by the derivative with respect to the correspondent i_d, i_q values.

Chapter 4

ANALYSIS AND APPLICATION OF SELF-COMMISSIONING STRATEGIES

In this section practical implementation of the self-commissioning techniques is detailed. Software and hardware used for the lab tests are described as well as the online and offline post-processing procedures for the obtained data. Sinusoidal current injection and square wave current injection tests are used to identify the flux linkage characteristics as a function of the currents in the rotor reference frame. Then, apparent and incremental inductances are identified using polynomial representations of the flux surfaces. The self-commissioning techniques are applied to two 3 kW SynRMs from different manufacturers. The accuracy of the obtained parameters is evaluated experimentally, running the SynRM drives in torque control mode by the PCC strategy and analysing the error in the prediction of the currents and the THD of the line currents. The selected current injection method is then applied to a 11 kW SynRM which is intended to be used in an electric vehicle in future work.

4.1 Experimental setup

Fig. 4.1 shows a block diagram representation of the equipment used for the self-commissioning tests. These equipments are illustrated in Fig. 4.2. This consist on an autotransformer connected to the grid through a circuit breaker and whose output feeds a three-phase diode-bridge rectifier. A dc-link capacitor connects the rectifier with a three-phase inverter; dc-link includes also a resistive load for protection when deceleration tests and negative torque conditions are produced, since it is not possible to regenerate power back to the grid through the rectifier. The inverter feeds the SynRM through current sensors and a circuit breaker. Gate signals for the inverter are generated by Matlab, with Simulink and dSPACE library, ControlDesk interface programme for dSPACE containing virtual instruments and data acquisition facility. The control scheme is implemented in a dSPACE DS1103 board considering a sampling and control period of $Ts = 60\ \mu$s. The input voltage is regulated between 0 V – 400 V by the autotransformer, while the diode-bridge rectifier leads the dc-link, thus providing an average voltage of 565 V at the 4.7 mF capacitor terminals.

The operation of the control system in the rotor synchronous reference frame requires the measurement of the rotor position, which is obtained from an incremental encoder. At the same time, the controller requires the rotor to be positioned in

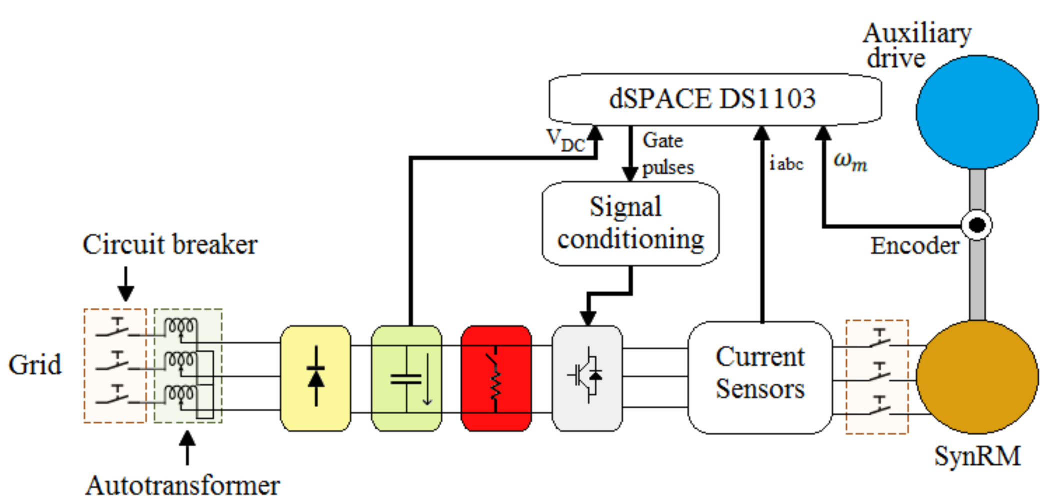

Figure 4.1. Experimental setup block diagram

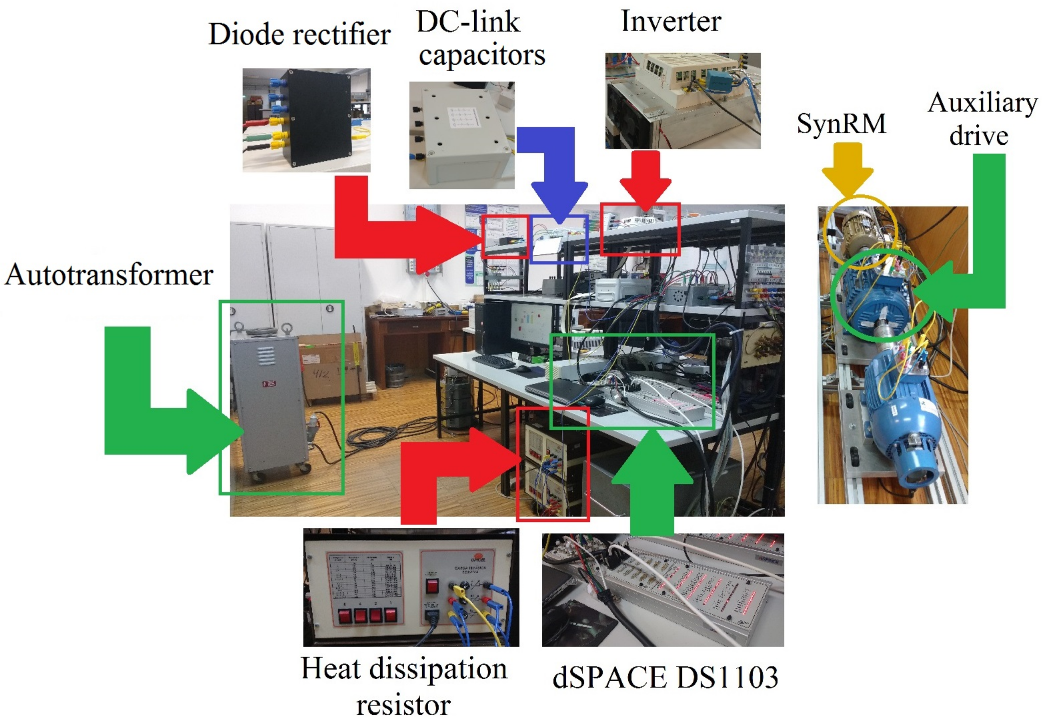

Figure 4.2. Hardware and equipment for experimental tests

an initial angle. Thus, before each test, a constant dc current is injected along machine d-axis during approximately 4 seconds to align the rotor. This technique takes advantage of the saliency in the SynRM by making the flux produced by the injected current to take the least reluctance path, aligning the rotor in the reference or zero position.

In all the commissioning and validation tests, the shaft of the motor is coupled to an induction motor drive. For commissioning tests, this only acts as an additional inertial load, while it works as an auxiliary drive during the validation test. In the latest, the SynRM is operated in torque control mode with an imposed torque reference input; the auxiliary drive then provides speed regulation.

The self-commissioning test is applied to the motors with the nameplate characteristics summarised in table 4.1. It is worth to mention that, given the limitations of the available test rig, only the results for the two 3 kW motors are evaluated experimentally under the same conditions. The results of the 11 kW motor are tested by running it in free-shaft condition. The objective is to "tune" the commissioning

Table 4.1: Nameplate data of tested motors.

Manufacturer	Power (kW)	Speed (rpm)	Voltage (V)	Current (A)	Efficiency (%)
KSB	3	1500	355	7.9	90.4
ABB	3		380	7.1	85.5
ABB	11		380	25.0	89.8

methodology to identify the magnetic parameters of the third motor (11 kW), which is going to be coupled to the power train of an electric vehicle prototype.

Based on the information from table 4.1 different limitations for voltage and current are considered during the software parametrisation. The software in Matlab/Simulink is set to stop any signal transmission to inverter gates when any limit is triggered. This complements the considered hardware protections such as fuses and circuit breakers.

4.2 Self-commissioning applied to a 3 kW KSB SynRM

The first motor under test is the 3 KW – 355 V KSB SynRM with 7.9 A rated current and 1500 rpm rated speed. The motor is shown coupled to the auxiliary drive in Fig. 4.3. Protections are configured to disable IGBT gate signals if the peak value of phase current is greater than 14 A.

In the present commissioning test, the first parameter to be determined is the stator resistance. It is measured by a multimeter Agilent U1253B. For increasing the accuracy of the voltage model, measurement is taken at the input of the circuit breaker, considering also the resistance of the connection cables feeding the motor. The total stator resistance to be used by the control system is thus 1.35 Ω.

As described in chapter 2, the current injection tests are executed using a PCC strategy. The performance of this controller relies on the parameters set offline before the test is done, but to follow a current reference high accuracy is not required and the errors are not significant if a rough estimation of the parameters is available. Here,

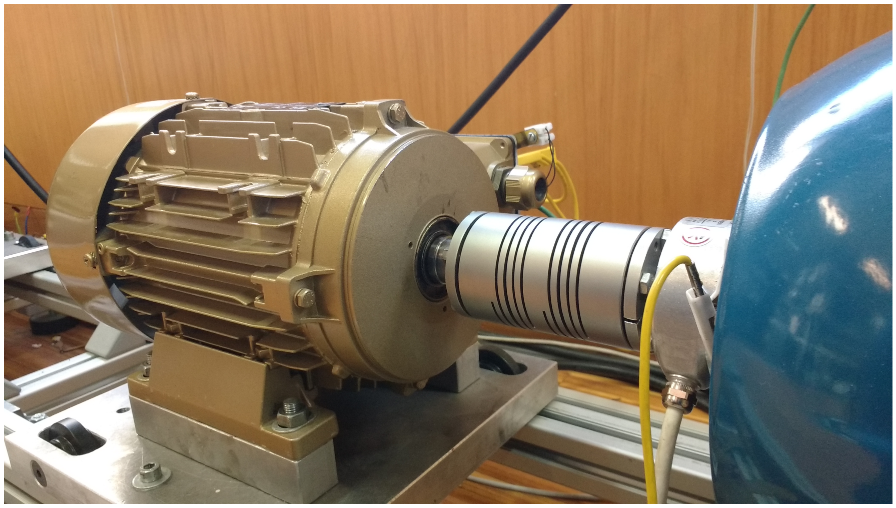

Figure 4.3. 3 kW KSB SynRM

approximate values for apparent and incremental inductances previously estimated in [34] are used. Initial values for apparent inductances are chosen as $L_d = 0.1172$ H and $L_q = 0.0712$ H.

4.2.1 Sinusoidal current injection test

Fig. 4.4 shows the Simulink implementation for sinusoidal current injection test. Sinusoidal waveforms with unit amplitude are set as reference in both d- and q-axes. The sine amplitudes are modified by a multiplication with a constant value which is set

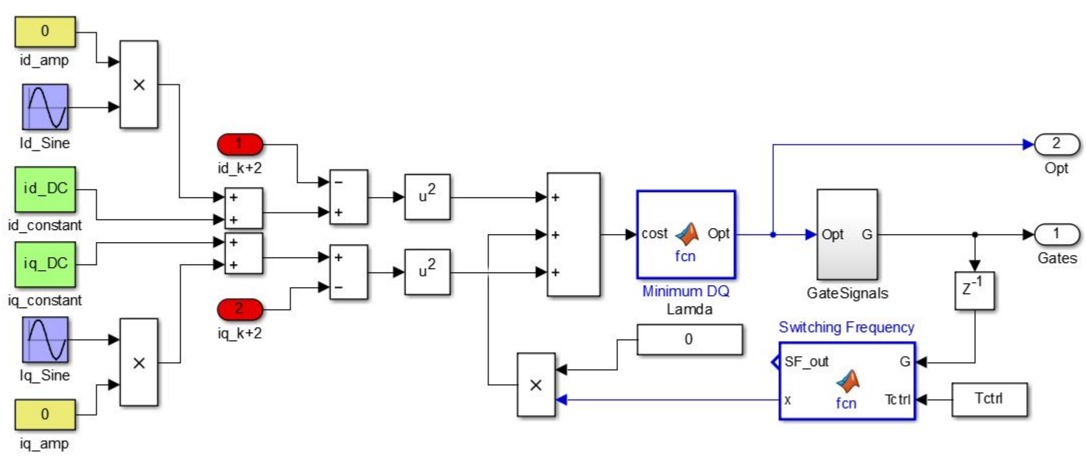

Figure 4.4. Simplified Simulink diagram for sinusoidal and dc current injection

online by the user in the ControlDesk. A dc-current is also set from ControlDesk to be applied in the cross-axis for the cross-saturation identification. Then, the subtraction of the defined reference current (sinusoidal or dc) and the predicted current after unit delay is done. This prediction error is used in the PCC algorithm to follow the reference currents. Fig. 4.5 shows the sinusoidal currents set as reference in the cost function of the PCC system for both, d-axis and q-axis test with $i_q = 0$ A and $i_d = 0$ A, respectively. The amplitude of the sinusoidal waveform per axis is chosen as 80 % of the rated peak current, in this case $0.8 \times 7.9 \times \sqrt{2} = 8.9$ A, and a frequency of 30 Hz. A proper selection of sinusoidal amplitude is needed to define the range of identification of saturation phenomenon [1].

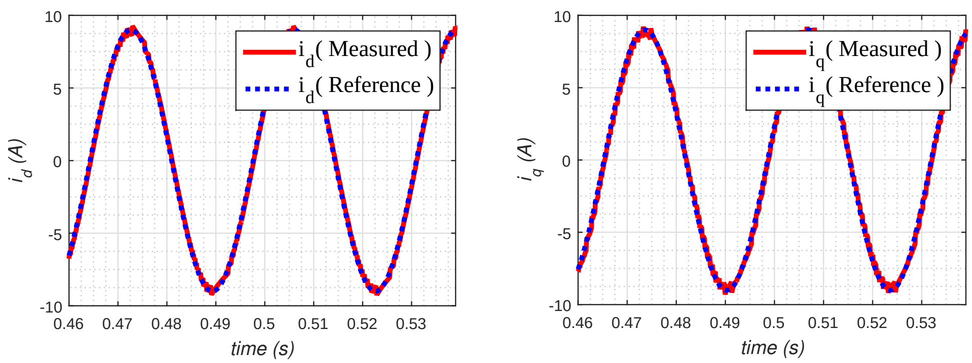

Figure 4.5. Reference and measured currents for d- and q-axis

Fig. 4.6 shows the flux linkage waveform calculated by the flux estimator for the d-axis case at $i_q = 0$. A time window of 1s was chosen to save the data. For the identification of the λ_d vs i_d saturation phenomenon, one complete cycle would suffice, but five cycles were chosen for calculations as the most stable during the acquisition time window. This is done to avoid the processing of data involving a transient behaviour after the current reference value is modified. Fig. 4.6 highlights the five cycles considered for the d-axis test. The procedure is repeated with the same sinusoidal amplitude but setting different values of dc current in the cross-axis (q-axis). The q-axis test follows the same procedure, applying sinusoidal reference for i_q and dc current for i_d.

Fig. 4.6 shows how distortions appear in both, current and flux waveforms. Thus,

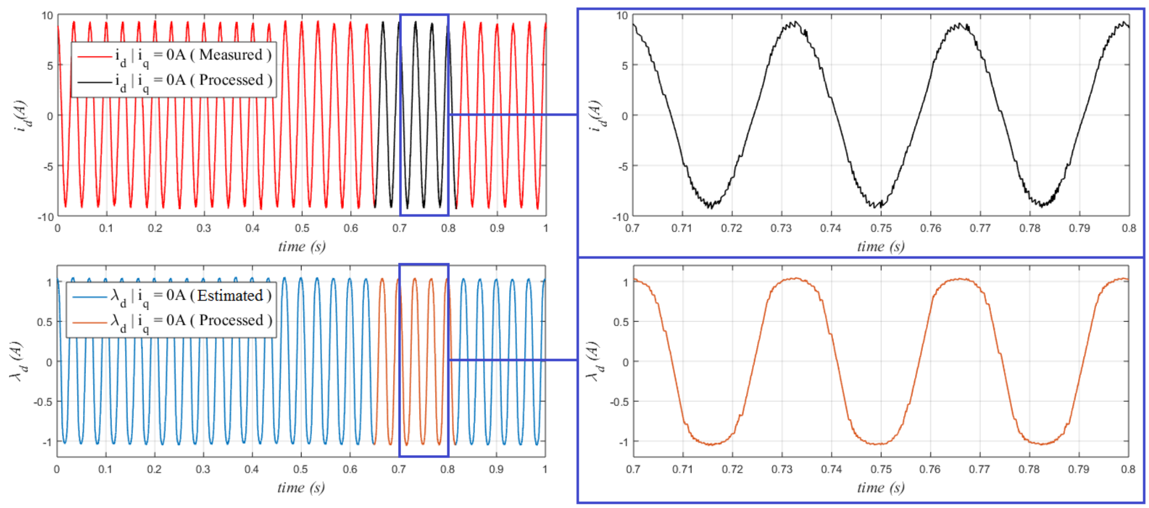

Figure 4.6. Estimated flux linkage, measured currents and selected samples for sinusoidal injection test along d-axis at $i_q = 0$ A.

a second order low pass filter is connected to the output of the calculated flux linkages and the measured currents, as shown in Fig. 4.7. The filter is designed with a butterworth configuration and a cut-off frequency of 80 Hz. This does not interfere with the reference current at 30 Hz, but it eliminates the harmonics with order larger than three.

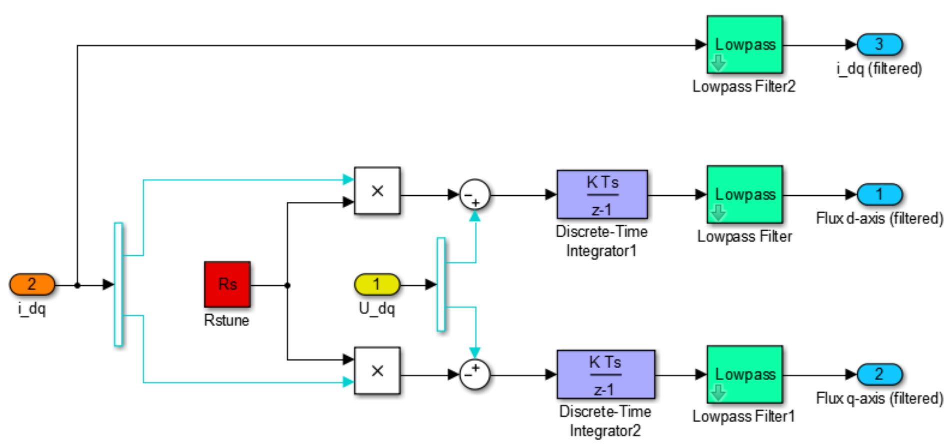

Figure 4.7. Addition of low-pass filters to the stator flux estimator and the measured currents

Fluxes are plotted as a function of the currents in Fig. 4.8. Fig. 4.8(a) shows the magnetisation curve for both d- and q-axis tests with a cross-axis dc current set to 0 A. The two curves almost perfectly overlap, and q-axis magnetisation curve presents a saturation at much lower values of current than the d-axis flux curve.

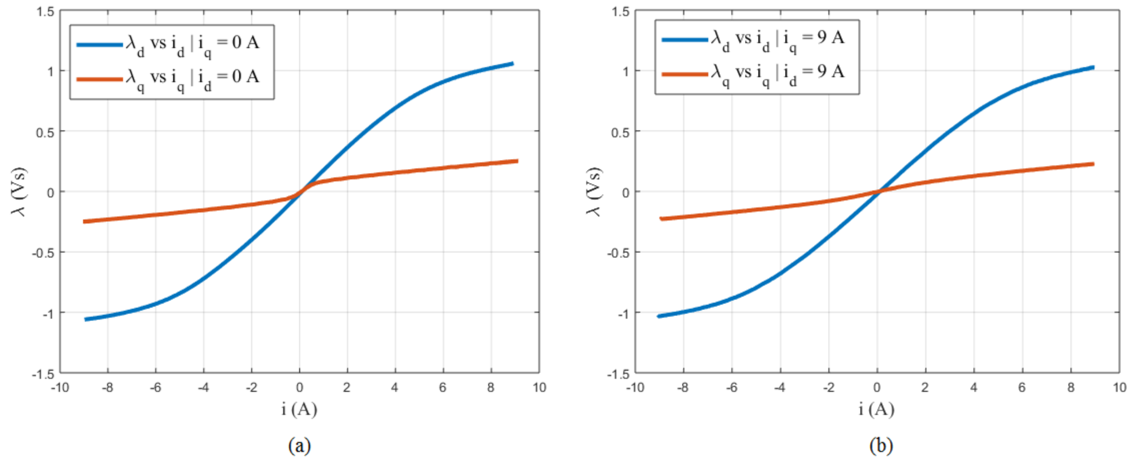

Figure 4.8. Flux curves in d- and q- axis for a dc current along the cross-axis of (a) 0 A and (b) 9 A

For the characterisation of the cross-saturation effect, the sinusoidal injection was done in the self-axis while four values of dc-current reference were injected along the cross-magnetic axis. Then, the flux surfaces can be reconstructed by interpolation between the flux curves at different cross-axis currents. The values of the dc reference signals must cover all the identification range for the cross-axis currents, that is, from $i_q = 0A$ to $i_q = 9$ A in case of the d-axis test and between $i_d = 0$ A and $i_d = 9$ A in case of the q-axis test. The dc-currents were chosen as 0 A, 3 A, 6 A and 9 A defining a set of linearly spaced values large enough to define the surface, but avoiding a high number of tests. Fig. 4.8(b) shows the flux curves considering the case with a maximum reference current in the cross-magnetic axis, i.e., 9 A.

Rotor position variation

Since the cross-saturation test involves the injection of reference currents along both axes at the same time, it produces a non-zero instantaneous electromagnetic torque. Self-commissioning is intended to identify parameters at standstill, therefore the produced torque should have a pulsating nature due to the periodic waveform applied; this should also present a zero-average in order to cause a zero-average speed. Fig. 4.9 shows the electric angle variations, the estimated electromagnetic torque and

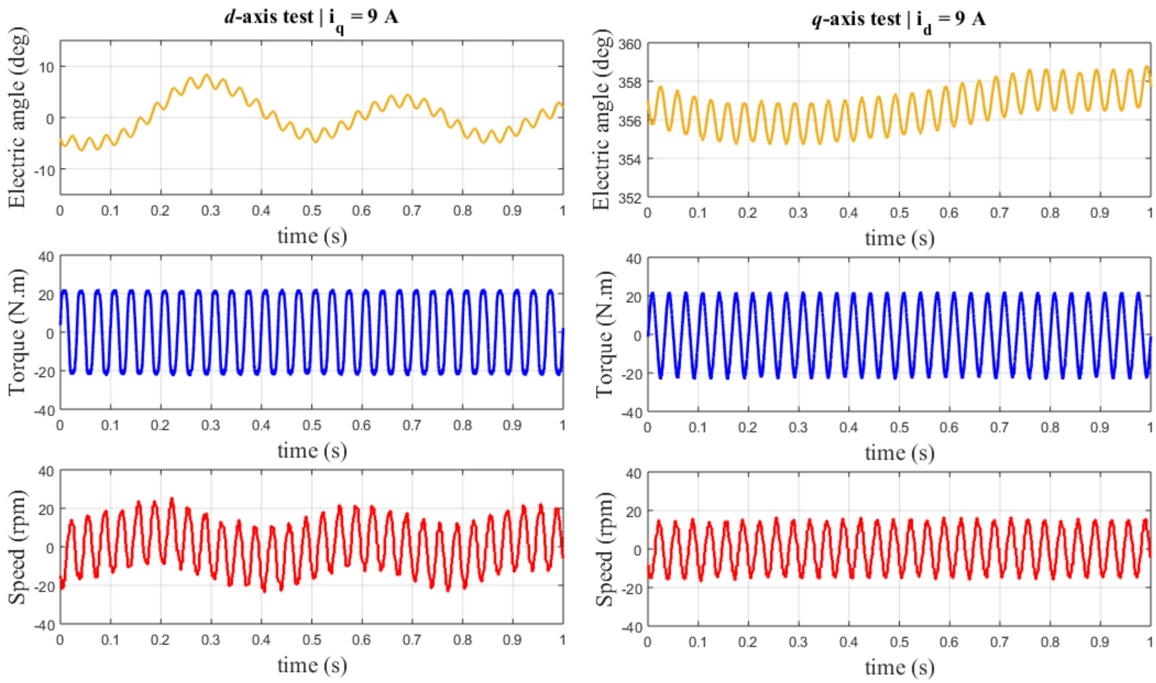

Figure 4.9. Rotor position, estimated electromagnetic torque and speed for the sinusoidal current injection tests

the speed for the current injection tests at the maximum cross-axis currents, the most critical situation for keeping the standstill condition.

For the d-axis test, rotor position varies around 15 electrical degrees while it changes 4 electrical degrees for the q-axis test. Torque and speed presented a pulsating behaviour with peak values of 20 N.m and 20 rpm, respectively. These values are comparable with variation of other commissioning tests obtained in previous works [55, 57].

During the sinusoidal injection tests in this thesis, the motors were coupled to an additional inertial load. However, if the machine is coupled to a low-inertial load or in free-shaft condition, the current steps produced by the change in current reference may lead to considerable rotor displacements. The rotor movement can be decreased or avoided by decreasing the limit i_q and identification will be still accurate since the saturation occurs at low values of i_q, while for higher values it can be approximated as a linear function. In the case of d-axis identification, it is not recommendable to lower the current limit for i_d, instead, the cross-axis current (i_q) can be decreased since the variations in flux curves due to cross-magnetisation are lower.

Frequency of current signal injection

The frequency for the reference currents was set as 30 Hz. Higher frequencies were applied for the self-axis tests, but this caused more violent vibrations and audible noise in the motor. It was decided not to continue with the cross-saturation test under this condition for safety and for preserving the motor. When lower frequencies were applied, the current injection in both axes produced also an electromagnetic torque pulsation at lower frequency; this caused oscillations of the rotor around its zero position and thus inaccuracies in the amplitude and offset of flux linkages. Moreover, this goes against the self-commissioning, intended to reduce the displacement of the rotor position.

Polynomial curve fitting

Once the flux curves for different values of the cross-axis current reference were obtained, apparent, self- and cross-incremental inductances can be computed. As mentioned in chapter 3, the use of an algebraic magnetic model based on a polynomial function reduces the complexity of the self-commissioning process, because it avoids the asymptotic behaviour produced at zero currents when direct division of flux and current is done. The calculation follows the representation in (3.9) to calculate apparent and self-incremental inductances. The effect of cross-saturation is considered by applying surface fitting tool to interpolate the data between the curves obtained at different levels of dc current injection.

Although other fitting methods such as rational functions can give good results when applied to measured data, they could produce vertical asymptotes. One example is shown in Fig. 4.10, where a rational function with order 5 in numerator and 5 in denominator was applied to the measured data.

This asymptotic phenomenon is not present when polynomial fitting is applied; however, the order of the polynomial must be carefully chosen as it relies on the consistency of the data. If the order is too low, inaccuracies in fitting would produce

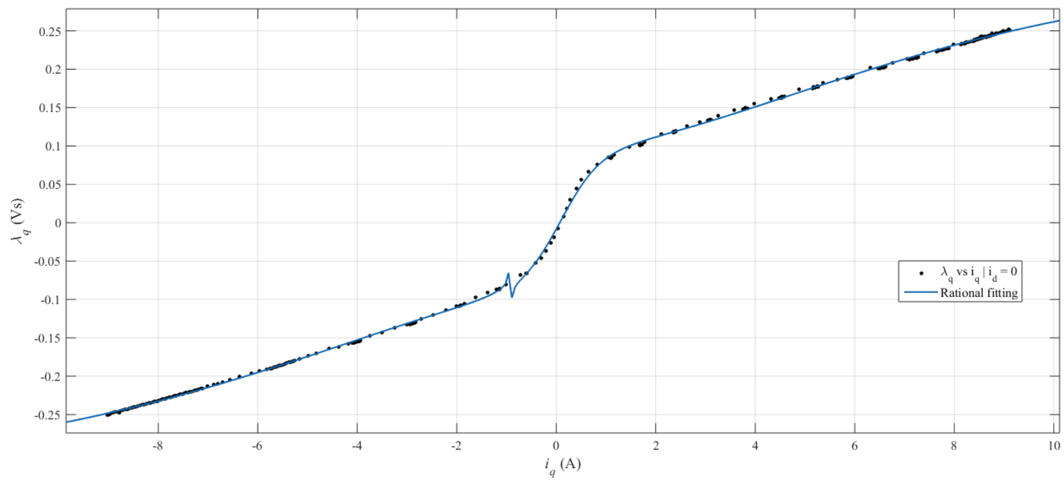

Figure 4.10. Rational fitting applied to the estimated flux in d-axis at $i_q = 0$ A.

significant errors in the flux values, but if it is too high, curve oscillations might appear between points, affecting the computation of derivative-dependent variables such as incremental inductances.

On the other hand, the Matlab polyfit function was initially applied to the estimated flux and current measurements corresponding to the five cycles chosen; however, since ascending and descending curves are present, polynomial curve tended to deviate towards one of the limits as the example shown in Fig. 4.11(b). The ascending and descending curves are caused by the hysteresis presented in the ferromagnetic material, as a consequence of the continuous change in the direction of the

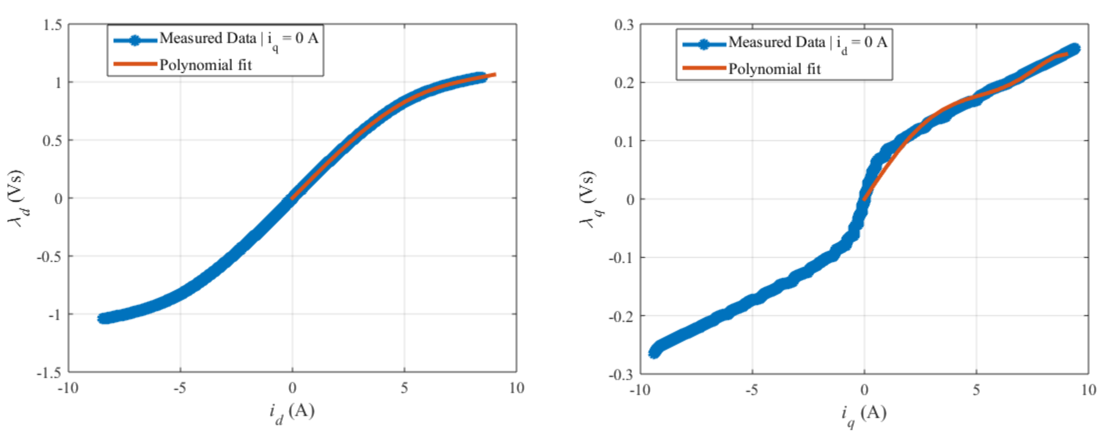

Figure 4.11. Polynomial fit applied to flux curves without averaging

sinusoidal currents. This phenomenon is included in the iron loss resistance in Fig. 2.3. Therefore, data from hysteresis loop must be averaged before its adaptation to the polynomial model, thus representing the steady state condition which bypasses the iron loss resistance in Fig. 4.11(b).

Fig. 4.12 illustrates the polynomial fitting applied to the positive values of obtained flux and currents in d-axis, each with a constant i_q equal to 0, 3, 6 and 9 A. Only positive values are considered for the fitting because the inductances present a positive and symmetrical behaviour for positive and negative values of current, so considering absolute value of currents in the control system allows to reduce the amount of computed data without affecting the results. Fig. 4.12 also presents the original data and the averaged curve superimposed to the fitted model to compare how this represents the average value of the magnetisation curve. In this case, a polynomial order of 7 is adequate to fit the data with enough accuracy. The polynomial is then represented by (4.1).

$$\lambda_d(i_d) = p_1 i_d^7 + p_2 i_d^6 + ... + p_7 i_d + p_8 \tag{4.1}$$

The resulting coefficients are summarised in table 4.2.

Table 4.2: Polynomial coefficients for $\lambda_d(i_d, i_q)$

	p_1	p_2	p_3	p_4	p_5	p_6	p_7	p_8
$i_q = 0A$	2.2575e-08	4.633e-08	2.783e-06	-5.369e-06	-1.34e-03	381.267e-06	0.1969	-19.9e-03
$i_q = 3A$	4.218e-08	3.771e-08	-1.4206e-06	-5.1027e-06	-1.0215e-03	408.679e-06	0.1869	-19.439e-03
$i_q = 6A$	2.880e-08	3.6582e-08	5.354e-07	-4.8307e-06	-1.0883e-03	406.678e-06	0.1847	-21.099e-03
$i_q = 9A$	2.194e-08	1.1855e-08	1.2548e-06	-9.2814e-07	-1.0762e-03	221.095e-06	0.1818	-19.586e-03

Fig. 4.13 shows the analogous result for the flux and currents in q-axis at the same values of constant d-axis current. The self-axis saturation characteristics of the q-axis can be modelled using a lower polynomial order since the effective airgap is larger along this axis [57]. In addition, as it reaches saturation at lower values of self-axis current i_q, an approximate linear behaviour can represent the flux at higher currents, reducing the complexity of the fitting. The model is then represented by

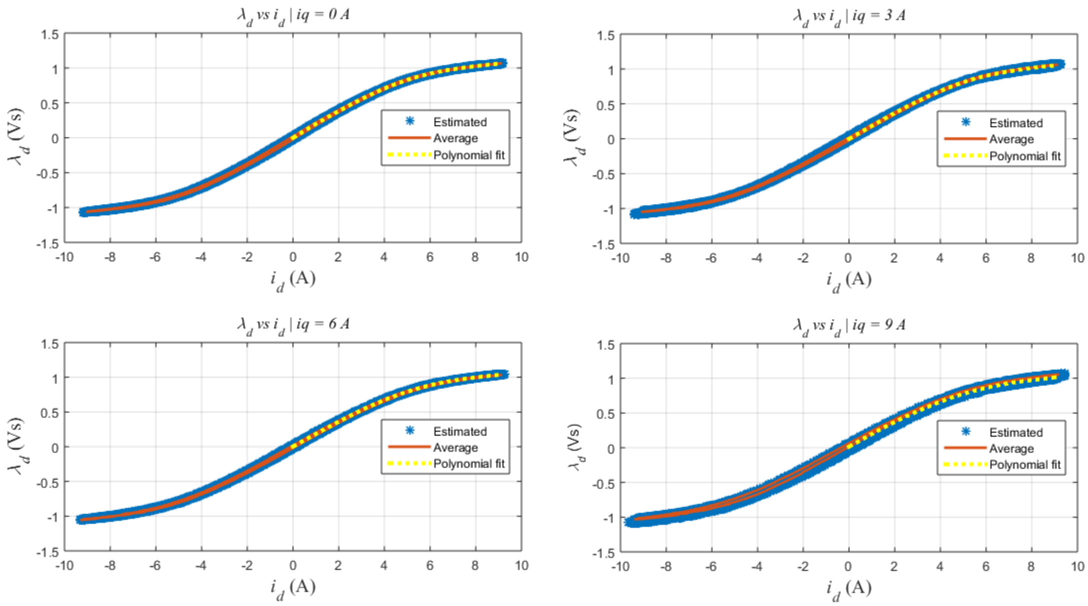

Figure 4.12. Polynomial representing the averaged flux curve for d-axis with $i_q = \{0, 3, 6, 9\}$ A.

(4.2).

$$\lambda_q(i_q) = r_1 i_q^6 + r_2 i_q^5 + ... + r_6 i_q + r_7 \tag{4.2}$$

Table 4.3: Polynomial coefficients for $\lambda_q(i_q, i_d)$

	r_1	r_2	r_3	r_4	r_5	r_6	r_7
$i_d = 0A$	-1.405e-05	421.684e-06	-4.968e-03	29.186e-03	-89.553e-03	0.1557	-8.3117e-03
$i_d = 3A$	-7.167e-06	219.536e-06	-2.674e-03	16.61e-03	-55.938e-03	0.1187	-3.048e-03
$i_d = 6A$	-2.358e-06	7.827e-05	-1.0578e-03	7.4840e-03	-29.276e-03	0.0821	-6.862e-03
$i_d = 9A$	-2.345e-07	5.132e-06	-4.7974e-05	467.951e-06	-4.796e-03	0.0461	-1.921e-03

Fig. 4.14 shows the mesh surfaces, which have been plotted using the different fitted curves for each dc-bias cross-axis current. The Matlab function *surf* was employed to plot the data corresponding to the flux curves at the four dc-current values. The averaged magnetisation curves are also shown to check the fitting given by the chosen polynomial order. It is worth to notice how the cross-saturation has a more significant effect on the q-axis flux vs current behaviour.

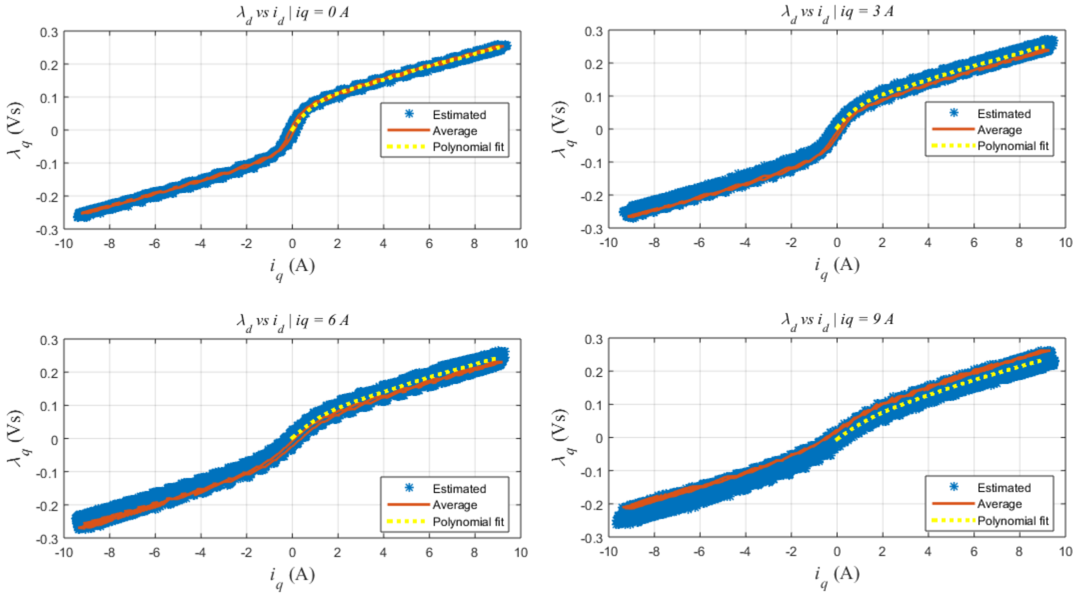

Figure 4.13. Polynomial representing average flux curve for q-axis with $i_d = \{0, 3, 6, 9\}$ A

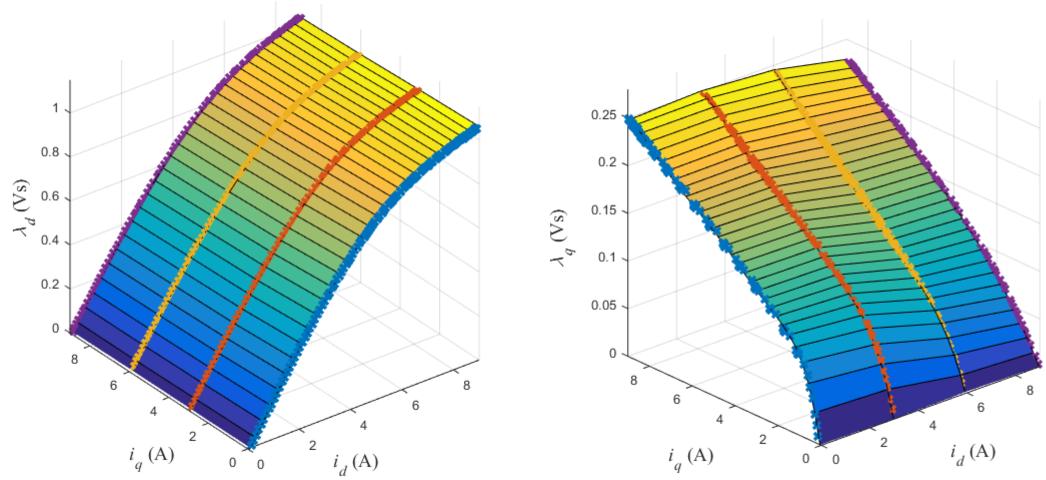

Figure 4.14. Surface representation of $\lambda_d(i_d, i_q)$ and $\lambda_q(i_q, i_d)$ for the KSB motor.

Fig. 4.15 shows the apparent inductances in self-axis for both d- and q-axis. These inductances were computed from the coefficient matrix in table 4.2 and table 4.3, by following the process described in (3.10) and (3.11) in chapter 3. Besides, partial derivatives are obtained from the original coefficient matrices to determine the self-incremental inductances, as shown in Fig. 4.16.

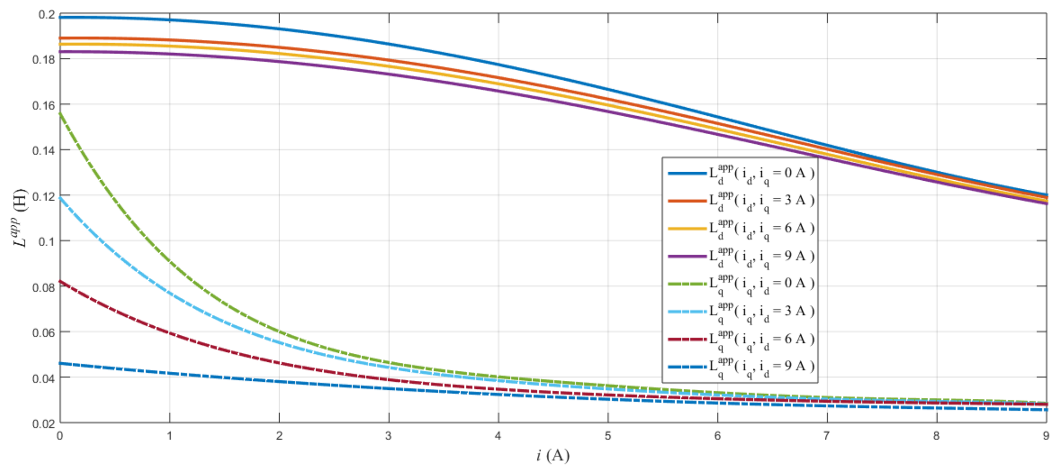

Figure 4.15. Apparent inductances at different cross-axis currents for the 3 kW KSB motor

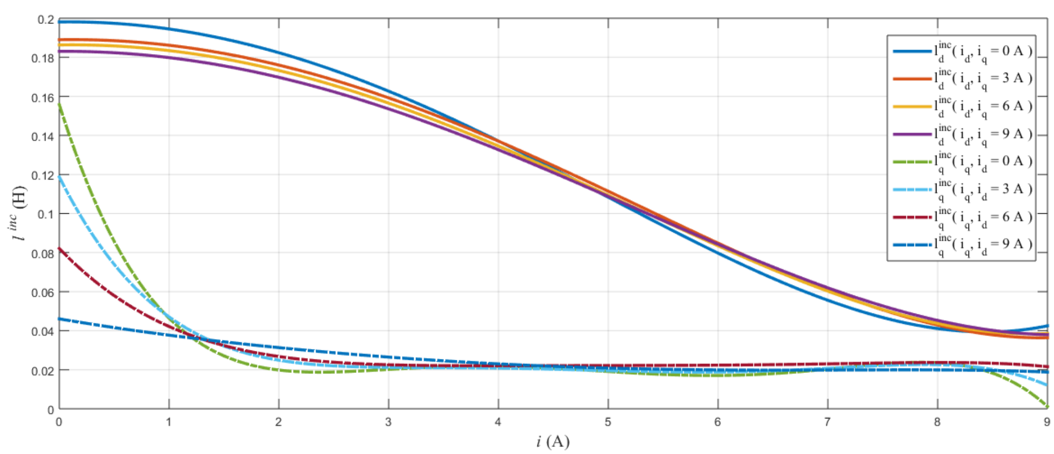

Figure 4.16. Self-incremental inductances at different cross-axis currents for the 3 kW KSB motor

Apparent inductances present an expected behaviour, with L_d starting with a constant trend, representing the linear region in the saturation curve, followed by a decrease due to saturation. Unlike L_d, L_q presents a decrease in the inductance value, for instance at $i_d = 0$ A, from $L_q = 0.16$ H to 50 % of its value for a current $i_q < 2$ A, reaching a steady condition which represents the constant slope after saturation.

In the case of the incremental inductances, it is worth to notice that inaccuracies are present for l_d around the maximum current, with a slightly increasing value, while the values slightly decrease at the maximum i_q for the l_q curves. This is caused by the *polyfit* tool, which "assumes" the trend of the flux curve for higher values of current, beyond the identification window.

Figs. 4.17 and 4.18 show the comparison between the obtained values and the look-up tables previously computed for the KSB motor [34]. In both apparent and self-incremental inductances, the values coincide in trends, but the curves obtained by this test present slightly higher values.

For the calculation of the cross-incremental inductances, the Matlab function *fit* was employed which allows to create a surface fit to the input data. A flux surface was then represented based on the flux curves obtained for different cross-axis currents. Then, the function *differentiate* was applied to the resulting flux surface, and the cross-incremental inductances were computed by finding the derivative of the flux surfaces in d- and q-axis, with respect to the currents i_q and i_d, respectively. Results are shown in Fig. 4.19. In this figure, the value l_{dq} represents the derivative of the flux in d-axis with respect to the current in q-axis. In a similar way l_{qd} represents the change of flux in q-axis with respect to i_d.

The cross-incremental inductances in both plots present negative values because

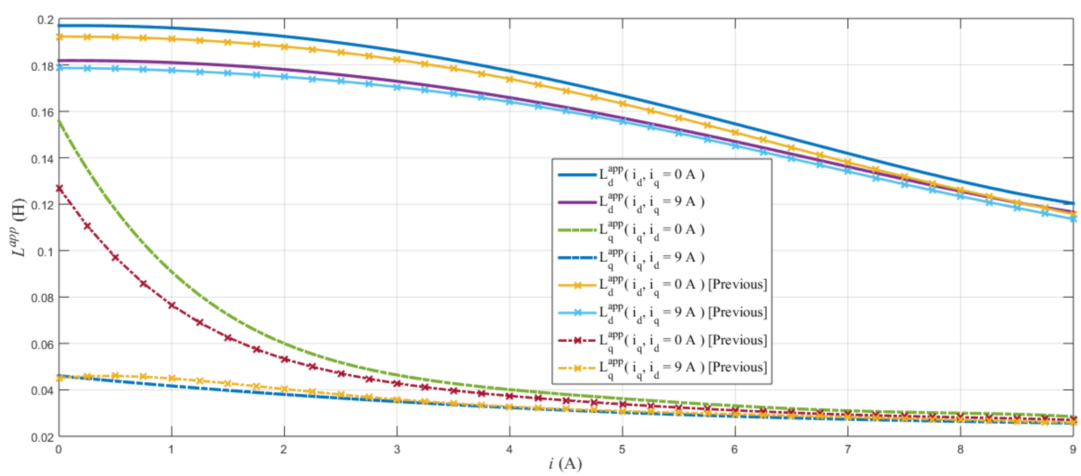

Figure 4.17. Comparison of apparent inductances calculated with sinusoidal test and previous look-up table values

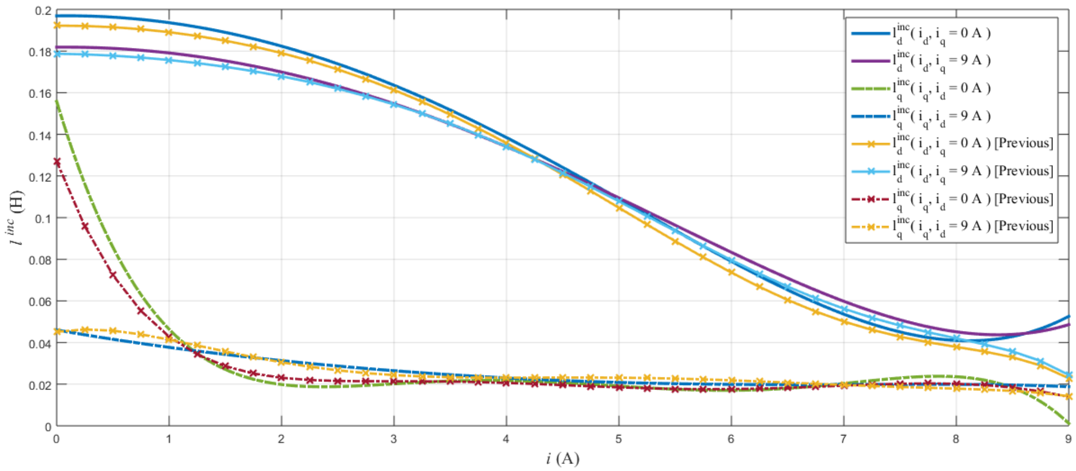

Figure 4.18. Comparison of self-incremental inductances calculated with sinusoidal test and previous look-up table values

the slope of the flux curves tends to decrease at higher levels of cross-axis currents. This happens when the redistribution of flux due to core saturation occurs, caused by the interaction of the currents in the two orthogonal axes through the common ferromagnetic core.

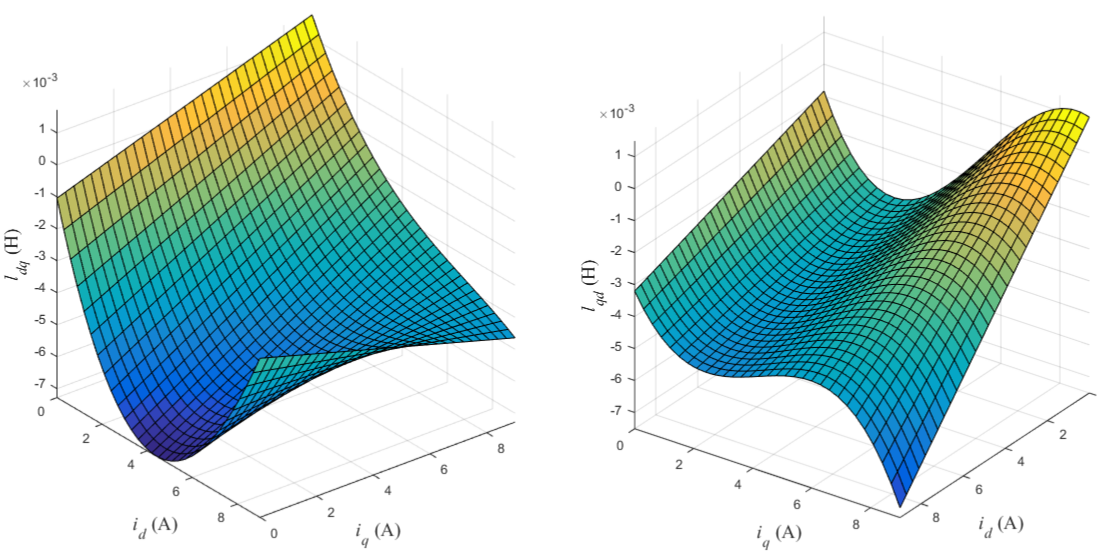

Figure 4.19. Cross-incremental inductances $l_{dq}(i_q, i_d)$ and $l_{qd}(i_d, i_q)$

4.2.2 Square wave current injection test

The flux curves from sinusoidal current injection test in Fig. 4.8 present a loop caused by hysteresis phenomenon. This is an effect of the iron losses, which were averaged in the post-processing to obtain the apparent and incremental inductances. This assumes that iron losses can be neglected in the equivalent circut, and it will not affect the accuracy in the flux estimation. In [27], it is proposed that a square wave current injection test can be applied for self-commissioning considering the iron losses. This test uses the flux curves just after the steady state is reached avoiding inaccuracies produced during transients due to the iron loss resistance. The test is then applied to obtain the apparent and incremental inductances and to compare their accuracy to the ones obtained from sinusoidal current injection. The test was done using the Simulink file as the one in Fig. 4.4, but with a square wave generator instead of sinusoidal one. The other blocks and their operation remained unchanged. Fig. 4.20 shows the square wave currents set as reference for this test. The maximum amplitude set for the square waveform per axis was also chosen as 80 % of the rated peak current, (8.9 A), and the same frequency of 30 Hz was chosen.

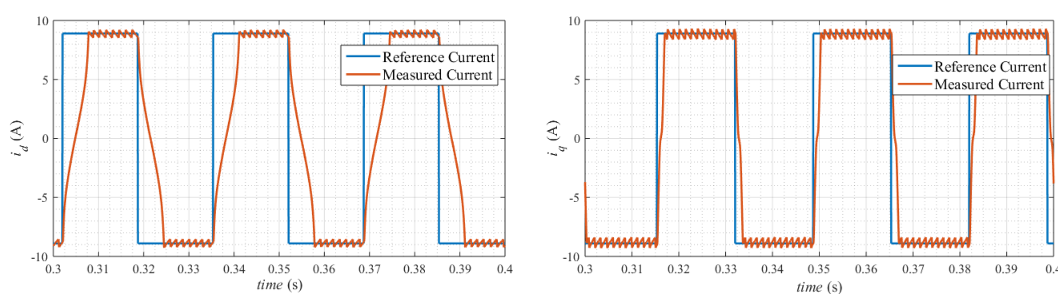

Figure 4.20. Reference and measured currents for square wave injection test

Fig. 4.21 shows the corresponding flux waveforms calculated by the flux estimator when maximum square amplitude is applied. Fig. 4.21(a) shows the measured waveforms of the d-axis test, while Fig. 4.21(b) shows the analogous results for q-axis test, both at $i_q = 0$ and $i_d = 0$, respectively. A time window of 1 s was chosen to save the data, but Fig. 4.21 shows a reduced range to better visualise the waveform shape.

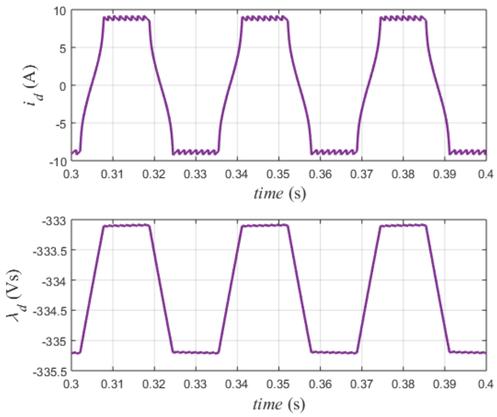

Figure 4.21. Estimated flux and measured current waveforms

Unlike the sinusoidal injection test, different square current waveforms must be injected at different amplitudes to fulfil the current span or range of identification. Since square signals represent current steps, only the steady-state values are considered for computation, as shown in Fig. 4.22.

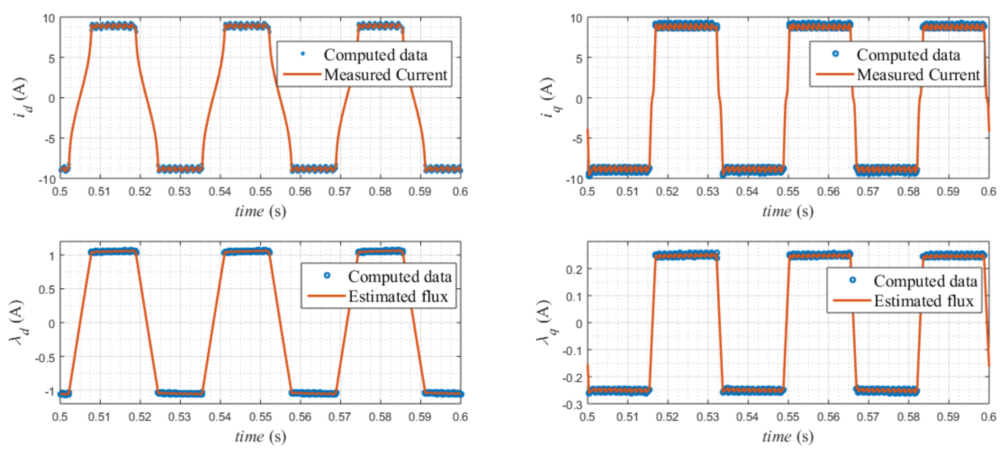

Figure 4.22. Values considered for flux data post-processing

Once the flux linkage as a function of the current is plotted, the processed data represents only discrete points along the saturation curve. Therefore, different amplitudes for the reference square wave signal are considered, and the flux curve is reconstructed by connecting the different points calculated before. The method ensures an accurate computation of the flux linkage without any assumption on the iron losses. This is illustrated in Fig. 4.23 where the polynomial fitting was applied to the group of points in the d-axis test. The amplitudes considered for the d-axis current were 3, 5, 7, 8, and 9 A. The interval between amplitude values was reduced for higher currents because the flux curve presents more appreciable non-linearities for these values, while it can be approximated to a linear function for low values. The polynomial curve spans only cover positive values of the current to reduce the amount of processed data by taking advantage of the symmetrical behaviour of inductances, as it was done for the sinusoidal current injection test.

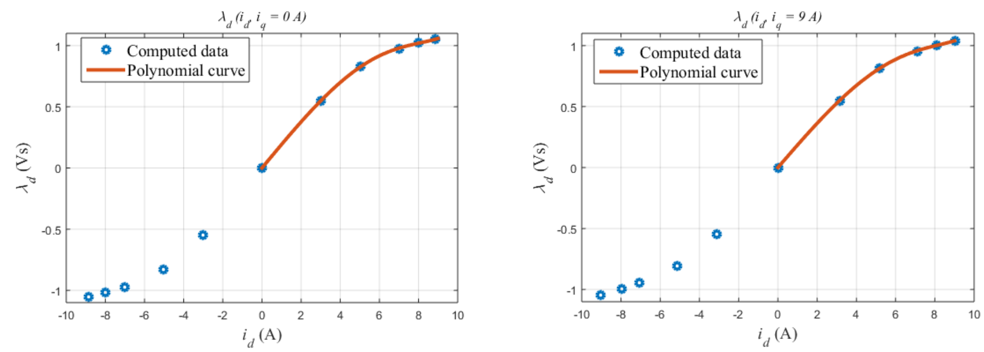

Figure 4.23. Polynomial fit for the d-axis data from square wave current injection tests for two different values of i_q

In the case of q-axis test, since nonlinear behaviour is mainly produced at low currents, the amplitudes of the square wave currents were considered in narrower steps for lower current values. The dc-current values injected in the cross-axis remain the same as for the ones used in the d-axis test. Fig. 4.24 shows the points obtained from the test and the polynomial fitted to the data for $\lambda_q(i_d = 0A, i_q)$ and $\lambda_q(i_d = 9A, i_q)$.

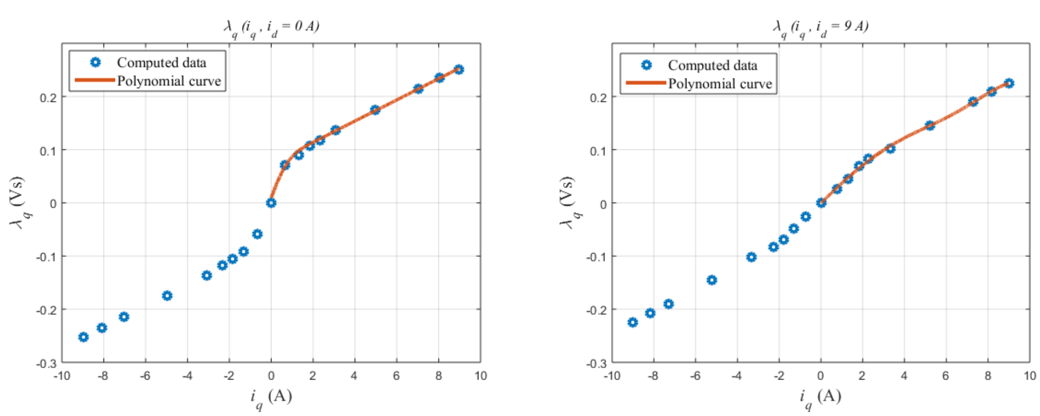

Figure 4.24. Polynomial fit for the q-axis data from square wave tests

Fig. 4.25 shows the flux maps obtained by computing the fitted curves at different cross-axis currents. These flux maps are obtained in the same way as the ones in the sinusoidal current injection test.

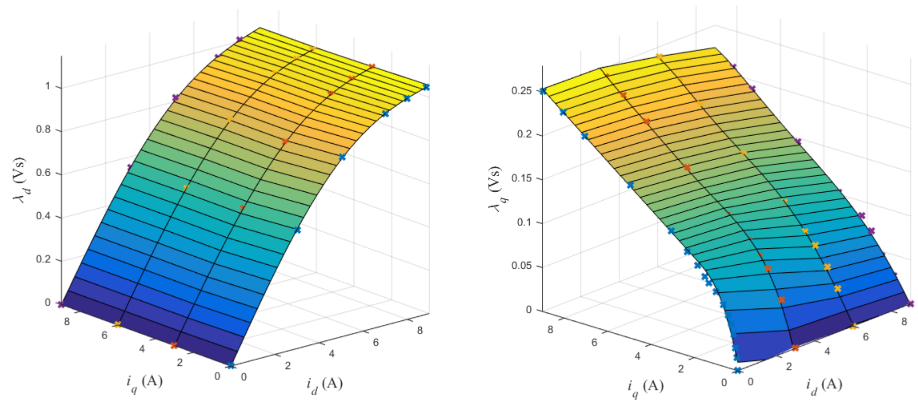

Figure 4.25. Flux maps generated from square wave current injection tests

Once the flux maps are obtained, the same procedure is followed as for sinusoidal current injection tests for calculating the inductances: polynomials of apparent inductances are obtained from the polynomial representation of the flux using (3.11), while self- and cross-incremental inductances are computed by the derivative of the flux with respect to the self-axis current and the cross-axis current, respectively. Figs. 4.26, 4.27 and 4.28 show the apparent, self-incremental and cross-incremental inductances, respectively.

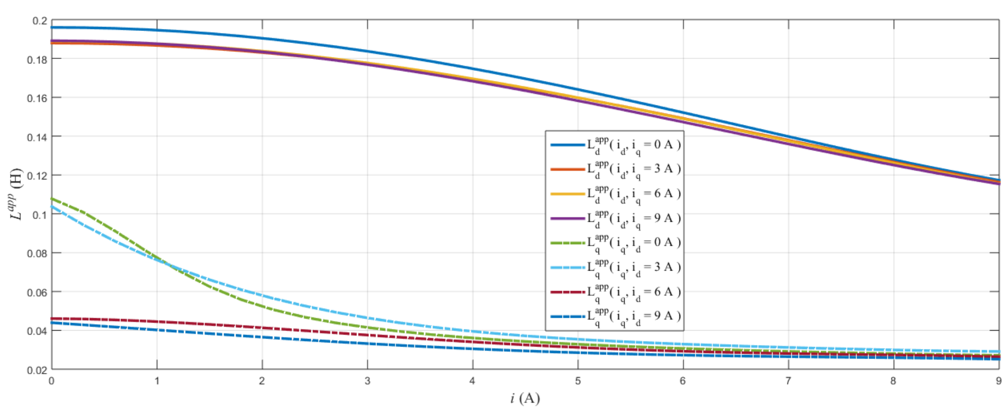

Figure 4.26. Apparent inductances generated from square wave current injection tests

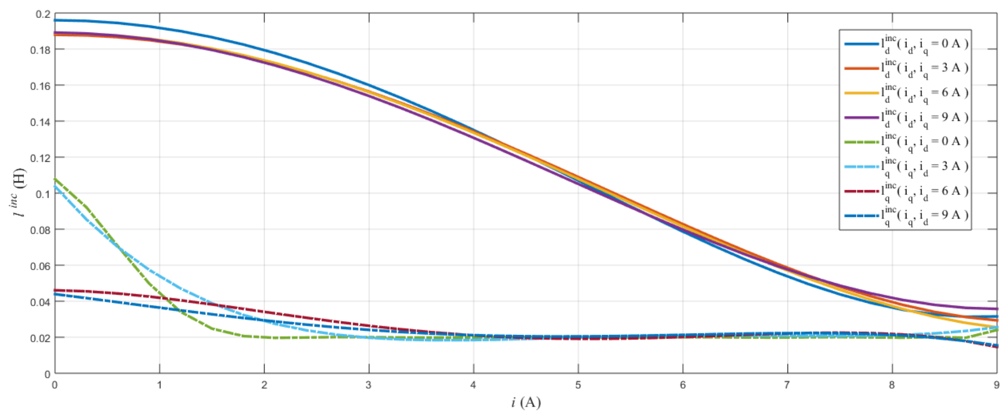

Figure 4.27. Self-incremental inductances generated from square wave injection test

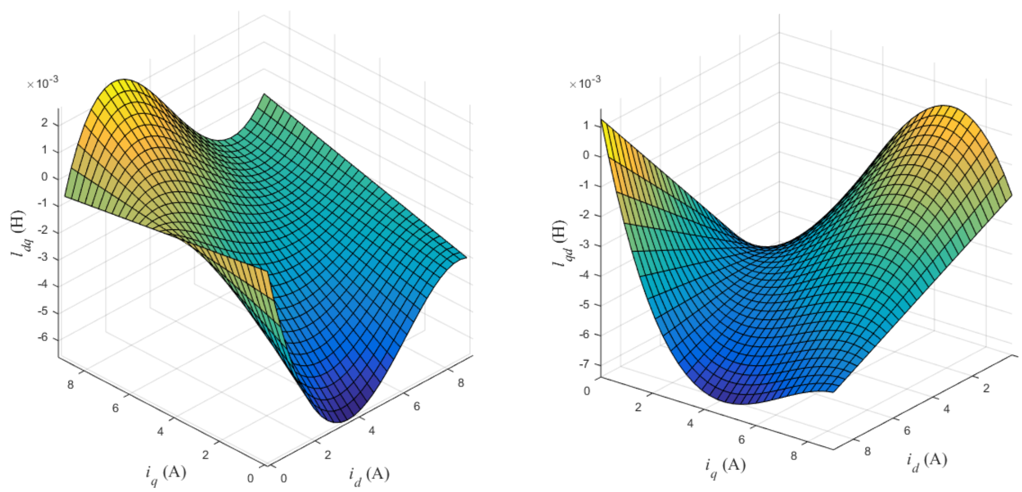

Figure 4.28. Cross-incremental inductances generated from square wave current injection tests

As it was done previously, comparison with the values estimated in previous works is done in Figs. 4.29 and 4.30. Results present an initial value inferior to the one obtained with sinusoidal test, and closer to the inductances previously estimated in LUTs. In addition, unlike the sinusoidal test, the self-incremental inductances in d-axis do not present increasing behaviour at the maximum currents. However, two of the l_q present a positive slope at maximum values of current.

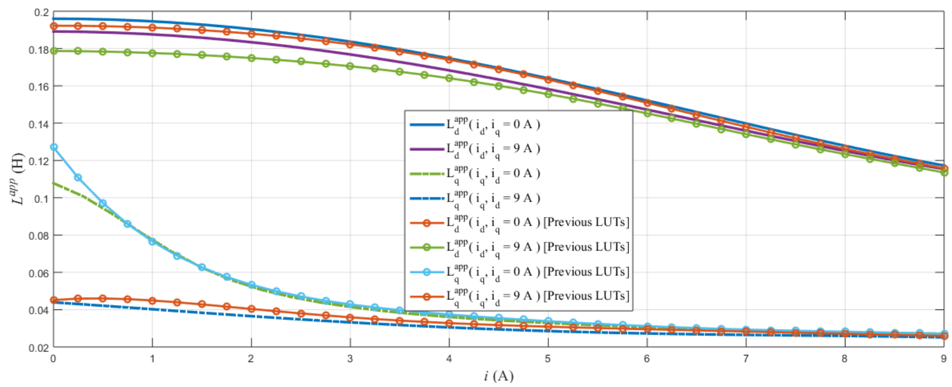

Figure 4.29. Comparison on apparent inductances from previous LUTs and the generated from square wave current injection tests

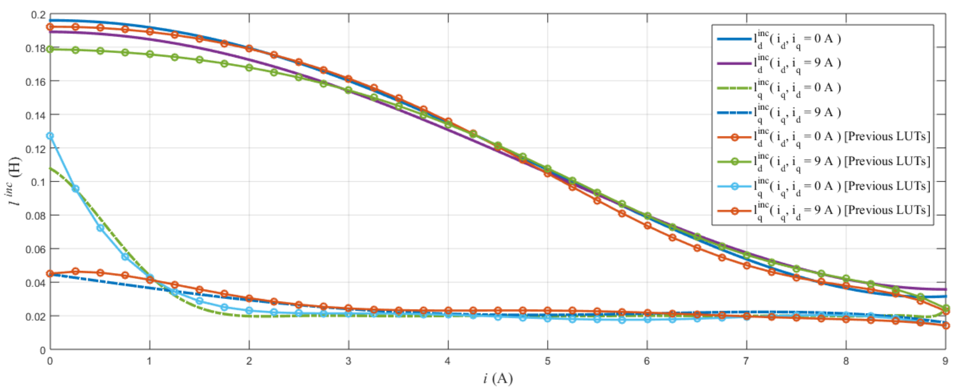

Figure 4.30. Comparison on self-incremental inductances from previous LUTs and generated from square wave injection test

4.2.3 DC-biased AC current injection test

The application of the sinusoidal current injection test assumes that iron losses can be neglected in the estimation of inductances. The results obtained with this assumption would be comparable with the square wave current injection test because the latest considers that iron losses cannot be neglected. Therefore, a test to evaluate how the frequency of an injected sinusoidal signal can affect the estimation of inductances is done.

To prove how the an injected current can affect the obtained flux curves due to the presence of hysteresis loops, a dc-biased ac current injection for self-axis characterisation is applied. This, as proposed in [4, 27], deals with the injection in one axis of a dc current with a superimposed small signal with reduced amplitude. The dc-current fixes an operation point on the flux curve, while the ac-current allows to define the trend of the flux in the vicinity of the operating point. The variation of the ac represents the slope of the flux in the given point, in other words, the incremental inductance. The frequency of the ac-current is increased to explore how the iron losses affect the estimation of the incremental inductances. In addition, the same reference current set for the sinusoidal current injection test is applied, thus generating a flux curve useful to make the comparison between its slope in the operating point at high frequency and the one given during the sinusoidal injection test.

Fig. 4.31(a) shows the results for a dc-biased ac current reference with a frequency of 200 Hz, while Fig. 4.31(b) presents the results with an ac current at 400 Hz. In both cases, the dc current was set as 2 A and the amplitude of the ac-current as 1 A. The Fig. 4.31(a) shows how slope of the flux curve can be considered equal to the one got from sinusoidal injection test. Fig. 4.31(b) shows how only a frequency of 400 Hz causes a deviation in the flux slope and inaccuracies in the inductance estimation. However, this variation is negligible at low frequencies such as the one applied while it deviates more at higher frequency, and the assumption on neglecting the iron losses for the sinusoidal current injection test is acceptable.

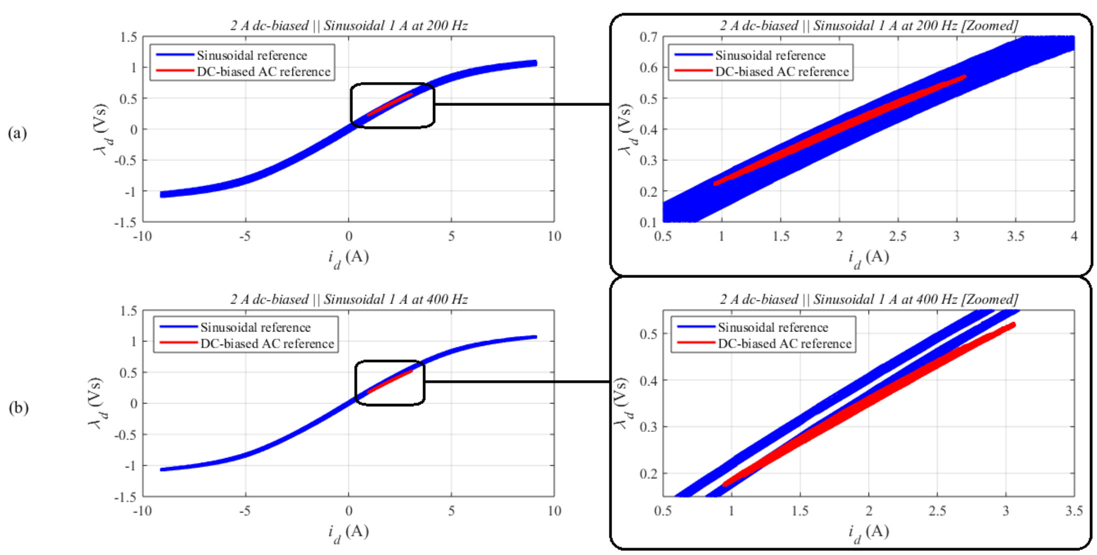

Figure 4.31. Flux curves for dc-biased ac current injection with ac frequency of (a) 200 Hz and (b) 400 Hz

4.2.4 Evaluation of the accuracy of the obtained parameters

The accuracy of the apparent and incremental inductances obtained from sinusoidal and square wave current injection tests were evaluated and compared with inductances previously stored in LUTs for the KSB motor. The evaluation process evidences how the values in the inductances affect the performance of the SynRM drive using PCC. This analysis is based on the response of the current prediction errors and the THD of the line currents. The prediction errors are higher if inductance values are less accurate and vice-versa. Moreover THD tends to be smaller when parameters with high accuracy are used.

The test consists in running the SynRM in torque control mode at a certain operating point, with a constant speed imposed by the auxiliary IM drive running in speed control mode. A RFOC strategy controls the auxiliary drive while the PCC is used in the SynRM with the apparent and incremental inductances from the LUTs previously estimated. Different operating points are tested, defined by a reference speed in the IM drive and a reference torque in the SynRM drive. The prediction error and the THD are determined for each operating point and the overall test is repeated for the inductances obtained from sinusoidal and square wave current injection tests.

The calculation of the current prediction error is done by the comparison between the predicted currents at instant k, for instant *k+1* $(\hat{i}_d(k+1), \hat{i}_q(k+1))$ and the measured currents at instant at instant *k+1* $(i_d(k+1), i_q(k+1))$. This is done during the test by applying a unit delay block in the estimated current and subtracting it from the measured current. The difference between the predicted and measured variables is defined as the current prediction error.

Current and torque references values for MTPA

Prior to the use of the PCC strategy with the obtained inductances, a matrix containing the reference values for i_d i_q and torque is required to provide a Maximum Torque per Ampere (MTPA) trajectory to the controller. This allows the system to minimise the stator copper losses for a given load condition by defining specific reference values for d- and q-current components.

To determine the values corresponding to the MTPA trajectory, the algorithm proposed in [34] is adopted here and represented by the flowchart in Fig. 4.32. The algorithm is executed prior the controller execution, and the resulting data is stored in a reference look-up table.

The initial stator current $i_{s,initial}$ is set as zero while the maximum stator current $i_{s,max}$ is defined from the nameplate current as $7.9 \times \sqrt{2} = 11.17 \approx 11$ A. The algorithm iterates i_s from zero to $i_{s,max} = 11$ A, increasing the current in steps of 0.1 A. For each iteration, the load angle φ is also varied between $\varphi = 45°$ and a

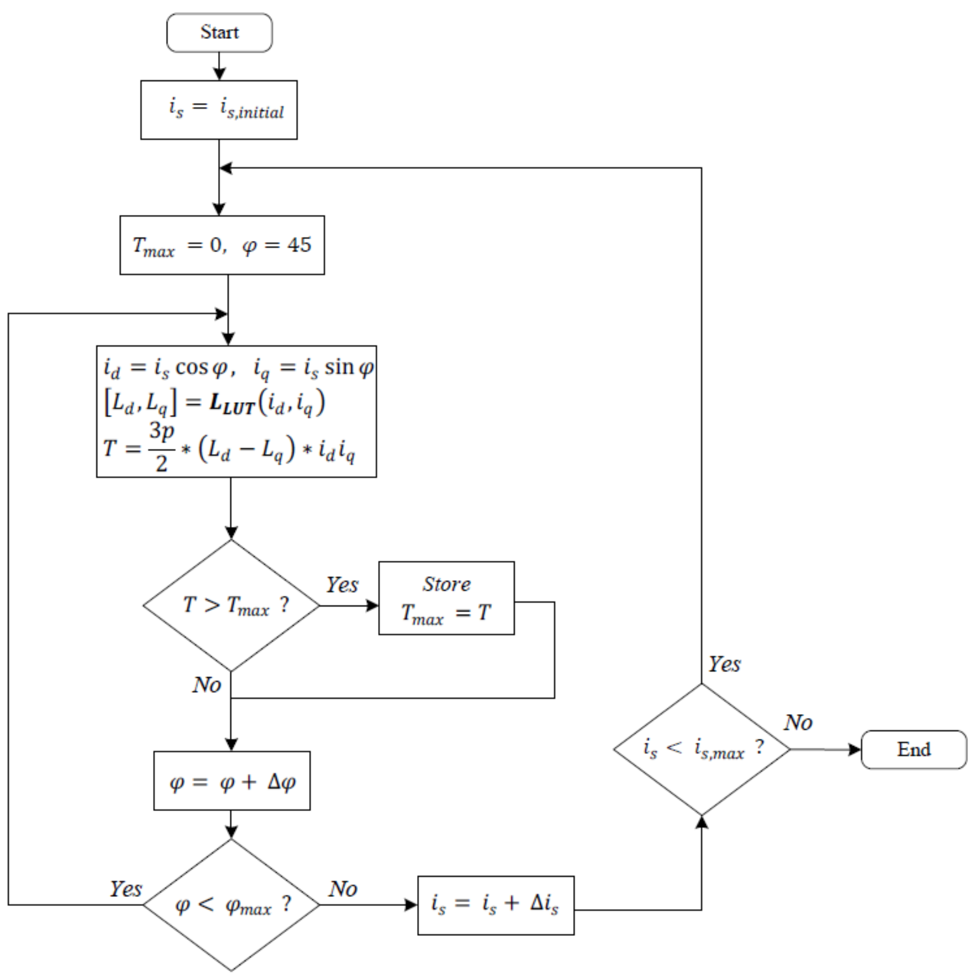

Figure 4.32. Flowchart for offline MTPA approach to define the reference currents i_d and i_q and the reference torque [34]

.

maximum value $\varphi_{max} = 80°$, in intervals of $\Delta\varphi = 0.1°$. Next, within the two cascade iterative loops, the values of i_d and i_q are computed using (4.3). Then, values for i_d and i_q are used in (2.12) while the inductances are used from the obtained apparent inductances. The maximum torque per value of i_s is then stored along with the correspondent values of i_d and i_q. Fig. 4.33 plots the optimal reference currents as a function of the reference torque.

$$
\begin{aligned}
i_d &= i_s \cos\varphi \\
i_q &= i_s \sin\varphi
\end{aligned}
\tag{4.3}
$$

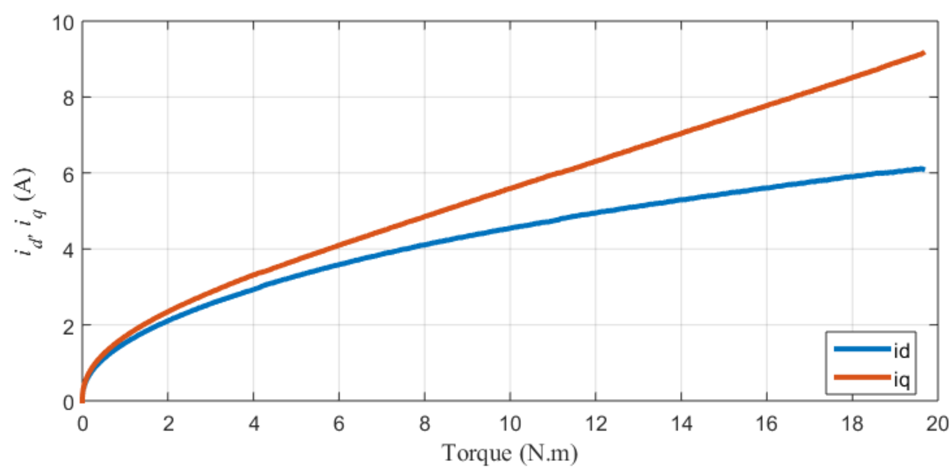

Figure 4.33. Reference currents and torque for MTPA operation of the KSB motor

Operation of the SynRM drive in torque control mode

Once the reference currents and torque are defined, the evaluation tests are done following the aforementioned procedure. An initial operating point was set to evaluate the response of the drive. The system was run at 500 rpm and the torque reference was set as 10 N.m. Fig. 4.34 shows the obtained current waveforms using the inductance values from the previously estimated LUTs and from the sinusoidal and square wave current injection tests. The currents in all cases present a correct sinusoidal shape with minimum distortion. The THD for each case is not greater than 2 % as shown in table 4.4.

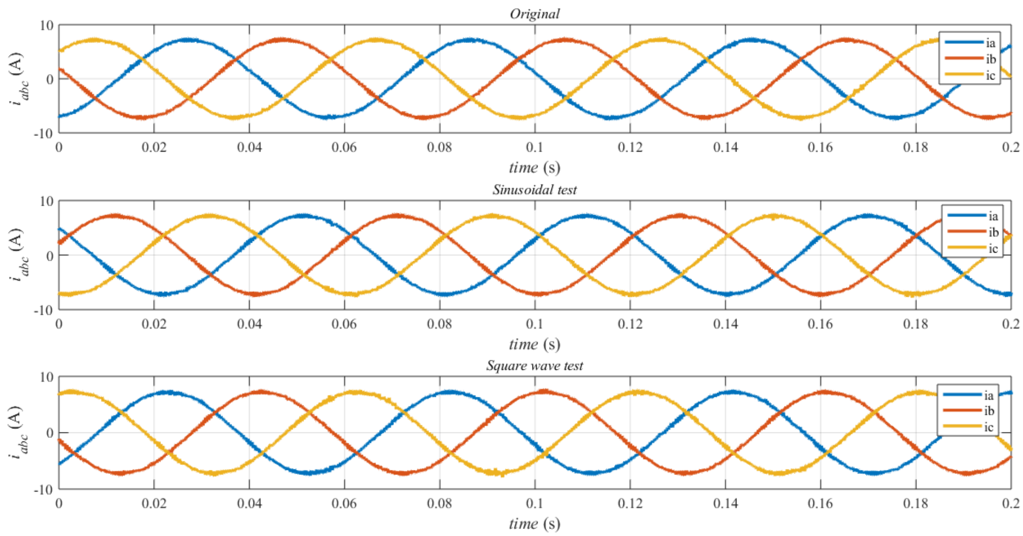

Figure 4.34. Measured currents at using inductances from previous LUTs and sinusoidal and square wave current injection tests. Operating point set as 500 rpm and 10 N.m

Table 4.4: Total current harmonic distortion in the measured currents using the previous LUTs and the obtained inductances

THDi	**Previous LUTs**	**Sinusoidal current injection test**	**Square wave current injection test**
$THD(i_a)(\%)$	1.06	1.10	1.22
$THD(i_b)(\%)$	1.06	1.08	1.22
$THD(i_c)(\%)$	1.10	1.18	1.31

Fig. 4.35 shows the prediction error in both i_d and i_q. In all cases this error remains under 0.5 A, and it is more appreciable for the q-axis current. Inductances from sinusoidal test present a slightly reduced error for i_q prediction while those from square wave injection have higher peaks.

Fig. 4.36 shows the estimated electromagnetic torque and reference torque. In all cases, the controller is able to follow the reference with an acceptable torque ripple. The torque ripple is represented in Fig. 4.37 as a percentage of peak error referred to the average torque. In all cases, ripple remains under 20 %, but it is slightly higher for the results with square wave current.

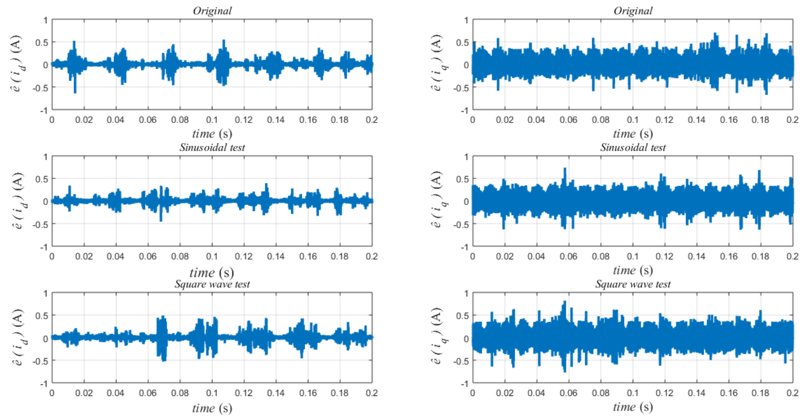

Figure 4.35. Predicted current errors at 500 rpm and 10 N.m

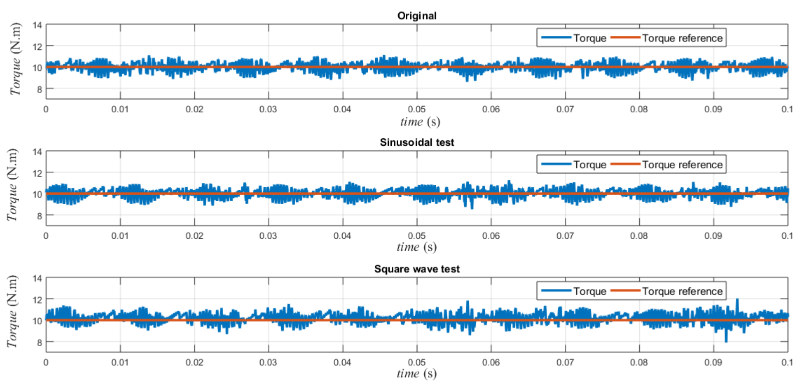

Figure 4.36. Estimated torque for the operation with inductances from original LUTs and from current injection test. Operating point set as 500 rpm and 10 N.m

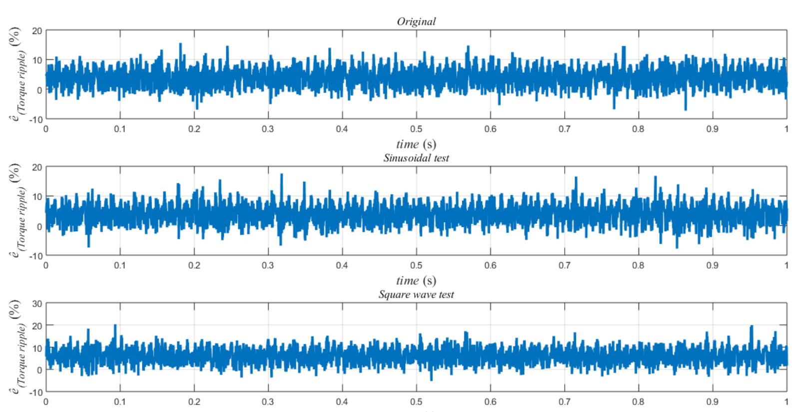

Figure 4.37. Percentage of peak error referred to average torque from original LUTs and from current injection test. Operating point set as 500 rpm and 10 N.m

The test is repeated for different operating points chosen with ω_m = {250, 750, 1200, 1500} rpm and T = {1, 5, 10, 15, 18 } N.m. Prediction errors are computed for i_d and i_q as well as the current THD for each operating point. Fig. 4.38 shows the prediction error in i_d for different operating points. Prediction errors are higher at larger values of torque, but their variation can be negligible for different speeds. Fig. 4.39 shows the prediction errors in i_q for the same operation points. They present the same behaviour as the prediction error in i_d, but with higher values; while prediction errors in d-axis currents are always less than 0.1 A, the errors for q-axis current are given between 0.1 A and 0.6 A.

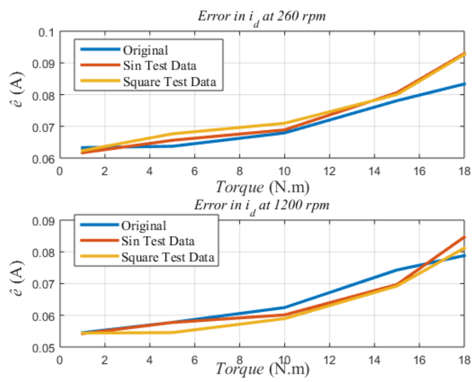

Figure 4.38. Prediction error in i_d for the operation with inductances from original LUTs and from current injection test.

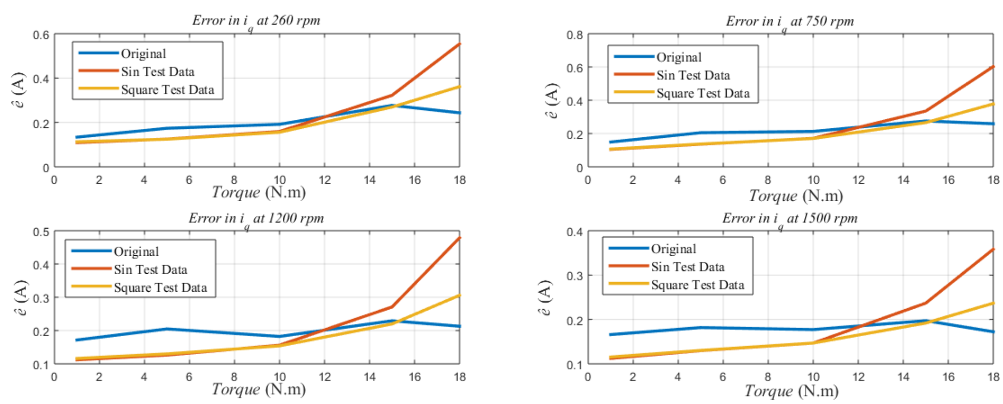

Figure 4.39. Prediction error in i_q for the operation with inductances from original LUTs and from current injection test.

Fig. 4.40 illustrates the current THD for each operating point. In all cases this is less than 8 % and presents lower values for the inductances in previous LUTs during rated torque operation. For reduced torque, inductances obtained from the current injection tests show better performance.

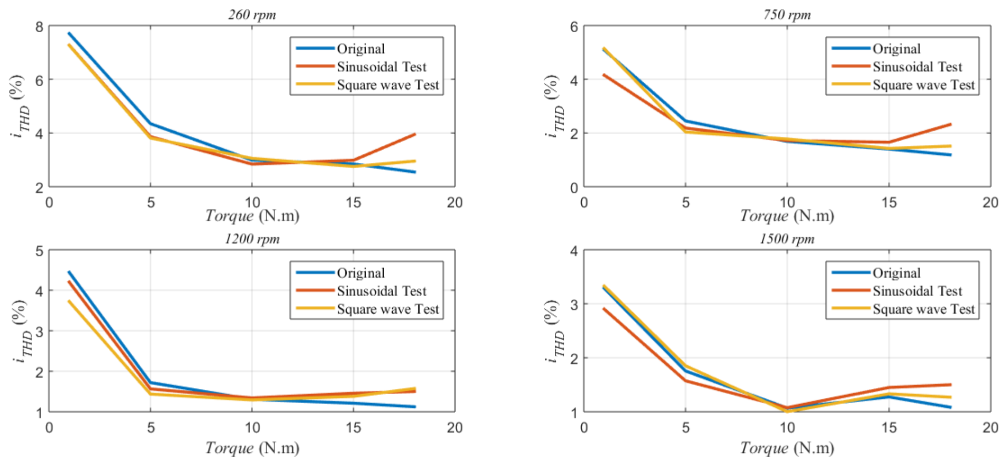

Figure 4.40. THD for line currents of the KSB motor at different operating points

4.3 Self-commissioning applied to a 3 kW ABB SynRM

Fig. 4.41 shows the second tested motor. The 3 kW, 380 V ABB SynRM in the figure is coupled to the auxiliary drive, and the same procedure applied to the first motor is followed considering both the sinusoidal and square wave current injection tests. This motor presents a higher nameplate voltage and thus a lower rated current compared to the 3 kW KSB SynRM. Since it is $7.9 \times \sqrt{2} = 10.04$ A, the software protection is set to disable the IGBT gate signal at instantaneous currents of 13 A. The motor also presents a lower nameplate efficiency (85.5 %), but unchanged rated speed (1500 rpm) and torque (19 N.m), as seen in the table 4.1. The stator resistance is measured in the same way as for the KSB motor, obtaining 1.79 Ω per phase.

To run the PCC it is necessary to set an estimation of the apparent and incremental inductances prior the test, but unlike the KSB motor, in which previously estimated inductance LUTs were available, the 3 kW ABB motor has no information about its inductance profile. Therefore, it is initially used the same LUTs previously calculated

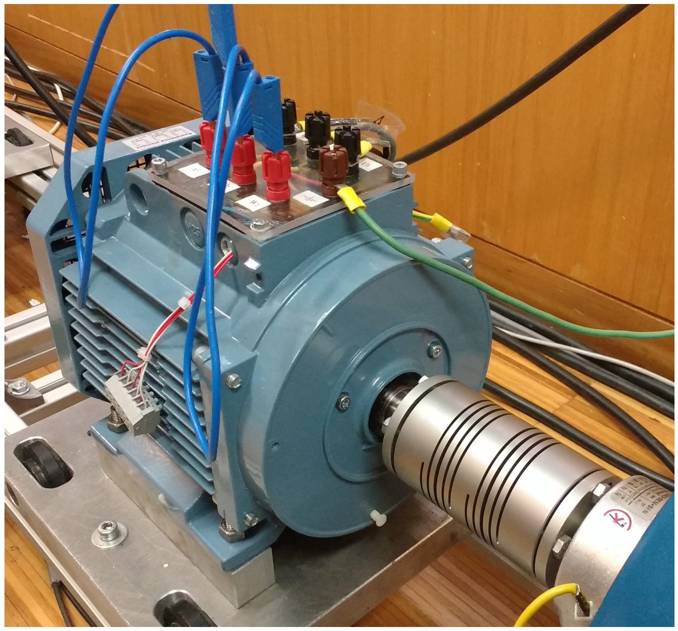

Figure 4.41. 3 kW ABB SynRM coupled to the auxiliary drive

for the KSB as a rough approximation of the required parameters. As stated before, to follow a current reference high accuracy is not required and the produced errors caused by the use of wrong parameters are not significant.

4.3.1 Sinusoidal current injection test

Sinusoidal current injection test follows the same procedure as the one applied to the KSB motor, using the Simulink arrangement in Fig. 4.4. The amplitude for the sinusoidal waveform is set as $0.8 \times 7.1 \times \sqrt{2} = 8$ A. This value is also defined as the limit for the dc reference current to be injected along the orthogonal axis in each d- and q-axis test.

The storage and post-processing of the data follows the same steps as before to obtain the estimated flux linkage and the measured currents: five sample cycles are chosen from the flux and currents and averaged to get one single cycle. Then, flux curves are represented by polynomials using the Matlab *polyfit* on the averaged flux curve. This process is done for both, d- and q-axes. The process is repeated for four values of dc-current (0 A, 3 A, 6 A and 8 A), thus obtaining four different flux curves. Fig. 4.42 shows the estimated data, the average flux curve, and the resulting polynomial fit for both axis, at cross-axis current of 0 A and 8 A.

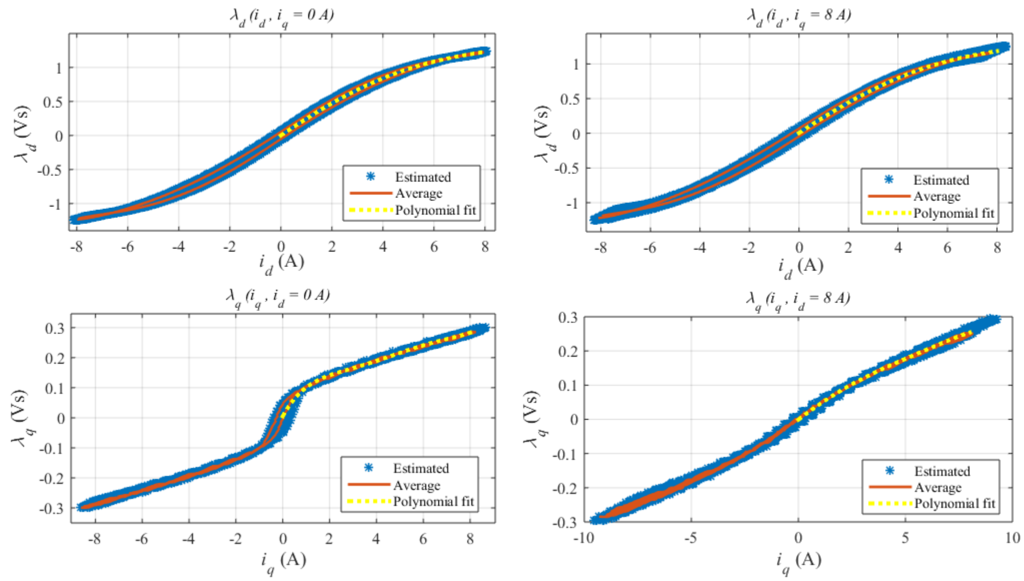

Figure 4.42. Polynomial fitting applied to flux averaged curve of the 3 kW ABB motor

The order of the polynomial which represents the flux curves is chosen empirically, based on the best fitting to the obtained data and the lowest order possible to reduce complexity. In case of d-axis flux curve, a polynomial order 7 was chosen, same as for the KSB motor. On the other hand, the polynomial order for q-axis flux curves were chosen as 5. The obtained polynomials are represented in the tables 4.5 and 4.6.

$$\lambda_q(i_q) = r_1 i_q^5 + r_2 i_q^4 + ... + r_5 i_q + r_6 \tag{4.4}$$

Table 4.5: Polynomial coefficients for $\lambda_d(i_d)$ representation in 3 kW ABB motor

	p_1	p_2	p_3	p_4	p_5	p_6	p_7	p_8
$i_q = 0$	-2.462E-07	8.198E-06	-1.061E-04	7.871E-04	-3.938E-03	-2.325E-03	2.517E-01	6.146E-04
$i_q = 2$	-1.856E-07	7.953E-06	-1.212E-04	9.528E-04	-4.387E-03	-2.288E-03	2.487E-01	-1.226E-03
$i_q = 4$	-6.532E-07	1.884E-05	-2.131E-04	1.284E-03	-4.893E-03	-9.461E-04	2.410E-01	9.850E-04
$i_q = 6$	-2.331E-06	6.454E-05	-6.945E-04	3.715E-03	-1.076E-02	5.004E-03	2.363E-01	2.821E-03
$i_q = 8$	-9.774E-07	2.671E-05	-2.824E-04	1.540E-03	-5.291E-03	5.275E-04	2.312E-01	4.433E-03

Table 4.6: Polynomial coefficients for $\lambda_q(i_q)$ representation in 3 kW ABB motor

	r_1	r_2	r_3	r_4	r_5	r_6
$i_d = 0$	6.234E-05	-1.524E-03	1.398E-02	-5.972E-02	1.429E-01	5.155E-03
$i_d = 2$	3.153E-05	-8.206E-04	8.128E-03	-3.850E-02	1.138E-01	1.872E-03
$i_d = 4$	3.212E-06	-1.396E-04	2.048E-03	-1.405E-02	7.417E-02	-4.977E-05
$i_d = 6$	-1.397E-06	-1.535E-05	7.307E-04	-7.274E-03	5.849E-02	-1.333E-03
$i_d = 8$	-7.842E-06	1.421E-04	-6.997E-04	-1.426E-03	4.742E-02	-8.528E-04

Flux maps are plotted from the obtained flux curves in Fig. 4.43. Flux surfaces follow the same pattern as the maps obtained for the KSB motor in the previous section. The increase in the cross-axis dc current causes a saturation in the self-axis at lower currents due to the core saturation in presence of both orthogonal currents. The effect of the cross-axis current is higher for the q-axis flux distribution because the q-axis is aligned to the path with airgap barriers in the rotor of the SynRM and the reduced amount of ferromagnetic material is saturated faster.

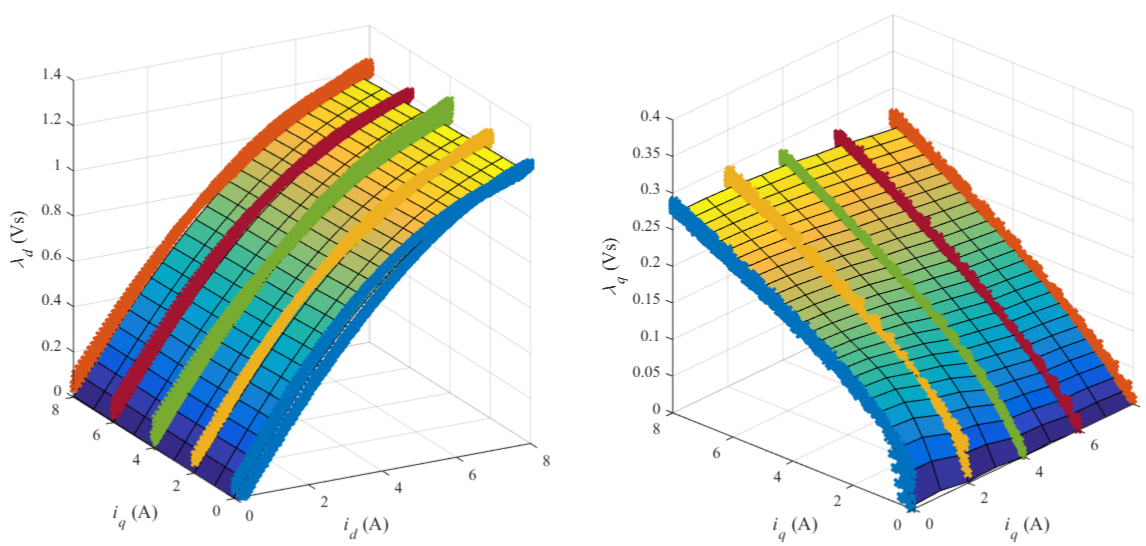

Figure 4.43. Flux maps and estimated flux at different cross-axis currents of the 3 kW ABB SynRM.

The flux surfaces represented by polynomials are processed following the same process as for the KSB motor. This results in the apparent inductances, shown in

Fig. 4.44. The inductance profile for the d-axis inductances is higher than the one presented for the KSB motor. The slope also decreases at lower rate when current increases, being not less than 0.14 H at rated current. For the q-axis inductance a similar pattern is observed with respect to the KSB motor, with an initial value around 0.1 H tending to constant value at maximum current. The self-incremental inductances in d- and q-axis are plotted in Fig. 4.45. Unlike the self-incremental inductances in the KSB motor, these present less oscillations around the maximum currents.

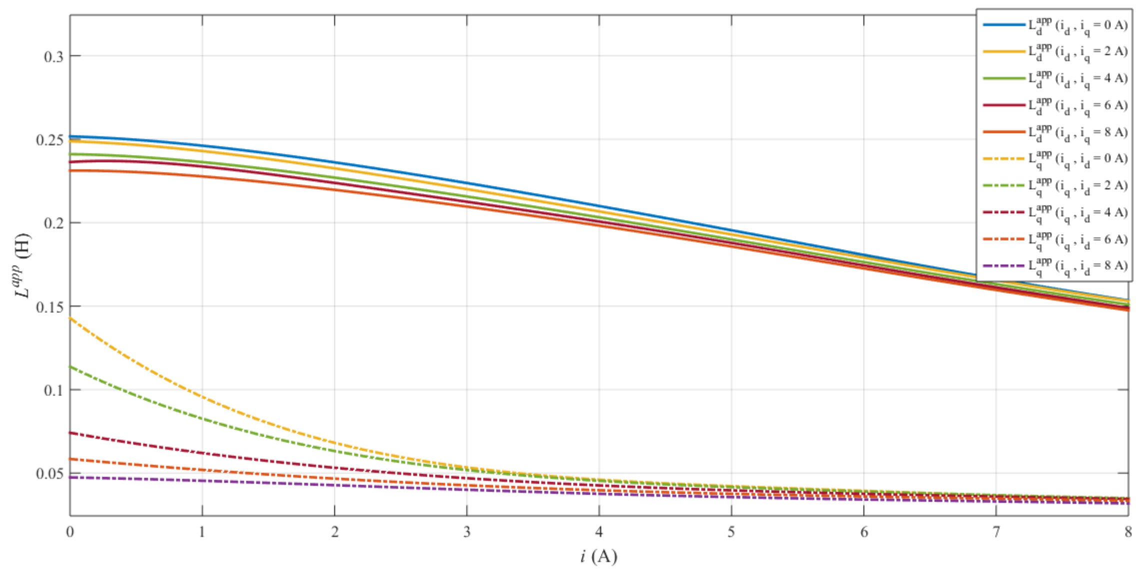

Figure 4.44. Apparent inductances for the 3 kW ABB SynRM.

Cross-incremental inductances are presented in Fig. 4.46. These surfaces represent how the slope of the flux curves changes with respect to the cross-axis current. The value of l_{qd} represents the change in the flux linkage in q-axis with respect to the d-axis current, while l_{dq} is the change of flux in d-axis with respect to q-axis. In both cases the values are negative since the cross-magnetisation causes a decrease in the flux curves values; this effect is higher or lower depending on the d- and q-axis currents.

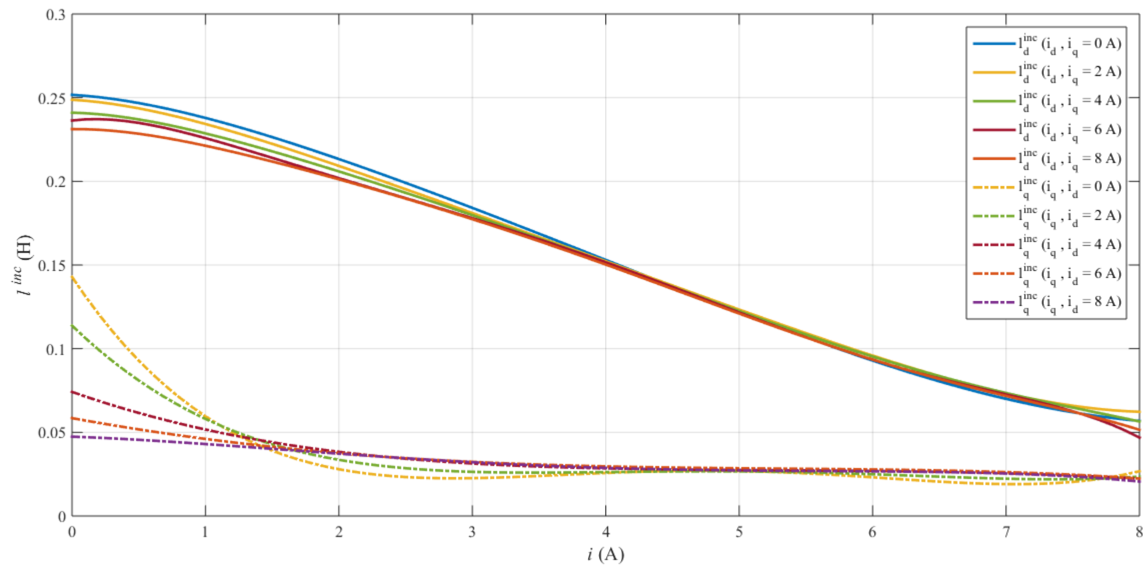

Figure 4.45. Self-incremental inductances for the 3 kW ABB SynRM

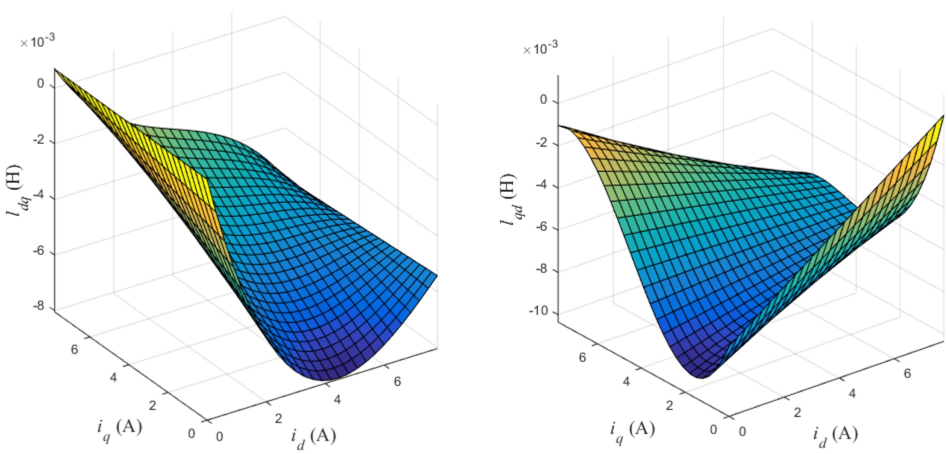

Figure 4.46. Cross-incremental inductances for the 3 kW ABB SynRM

Rotor position variation

Fig. 4.48 shows the rotor angle, estimated electromagnetic torque and speed during the sinusoidal injection test at maximum cross-magnetisation current. The electric angle presents oscillations around the initial rotor position, but these are not larger than 2.5 electrical degrees. During the post-processing it was noticed that the rotor position plot changed around zero degrees, thus producing values close to zero and 360°. To better understand this variation, the rotor angle is operated according to the Fig. 4.47. Result presented in Fig. 4.48 corresponds to the Torque and speed present the expected behaviour, with a pulsating periodic waveform with zero-average value.

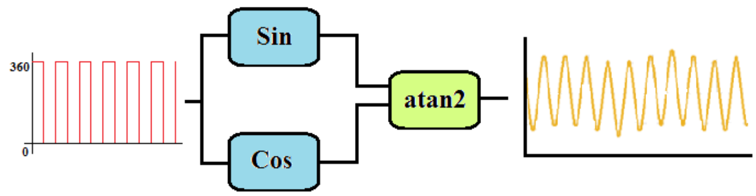

Figure 4.47. Post-processing of rotor position data to better visualise its variation

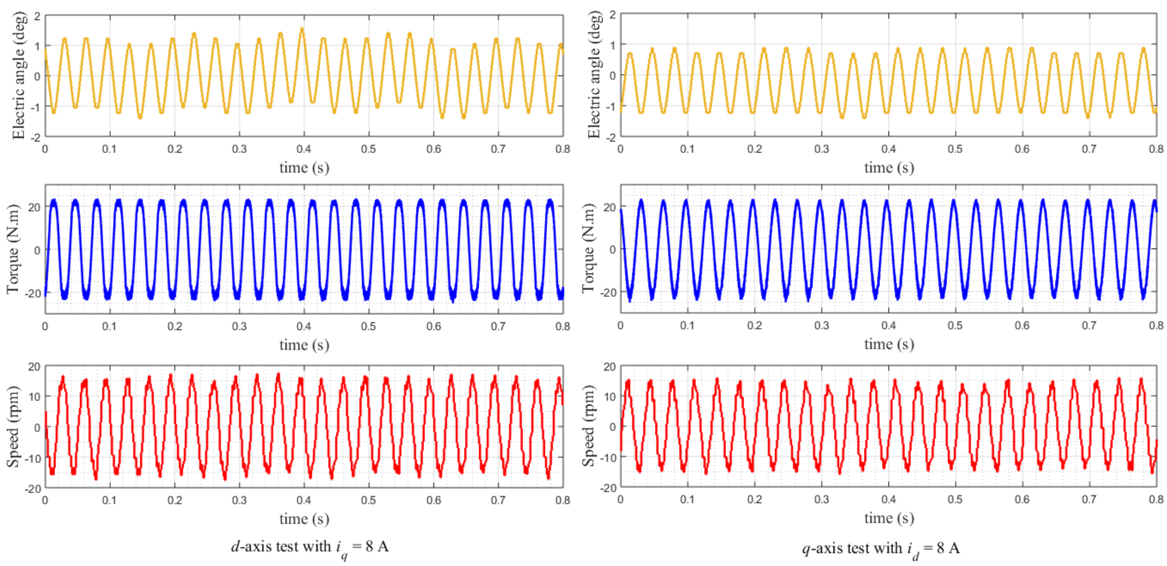

Figure 4.48. Rotor position, torque and speed during sinusoidal injection test for the 3 kW ABB SynRM

4.3.2 Square wave current injection test

Square wave current injection test is applied to the 3 kW ABB motor following the same procedure done for the KSB motor. The objective is to compare the accuracy of the inductances of the 3 kW ABB motor obtained using square wave injection with respect to the ones obtained by the sinusoidal current injection test. A significant improvement in the accuracy of the parameters with the square wave injection in terms of prediction errors and total current harmonic distortion would mean that iron losses cannot be neglected and their presence affect the accuracy of the results. In the case of the KSB motor, the results did not present significant differences because the high efficiency of the motor. In case of the 3 kW ABB SynRM, the reduced efficiency could lead to appreciable differences.

The setup and protections for the test are kept unchanged with respect to the sinusoidal current injection test, but the sinusoidal reference is replaced by the square wave current reference. These waveforms are set as the ones used in the previous square wave injection test in Fig. 4.20, with a frequency of 30 Hz but a maximum amplitude according to the nameplate current of the motor under test, that is $0.8 \times 7.1 \times \sqrt{2} = 8$ A.

The square wave current injected will produce a square-like waveform in the estimated flux. Thus, the steady state values are considered to get an average value of the flux linkage at the amplitude of the square wave current reference. These values represent discrete points along the saturation curve. Therefore, to fulfil the range of identification of the flux curves, the amplitudes of the square waveforms are changed. For the d-axis test the amplitude of the reference current is set as $i_d = 3$, 6, 7 and 8 A. The test is repeated for four values of the cross-axis current $i_q = 0$, 3, 6, 8 A and the flux curves at each value are plotted defined by the discrete points. Fig. 4.49 shows the polynomial fitting applied to the group of points in the d-axis test with a cross-axis current of 0 A and 8 A.

In case of the q-axis test, the amplitude of the square wave currents injected in the self-axis must be different given the different shape of the flux curve, with more variations at low currents. This requires a reduced step in the amplitude of the reference current at lower values. The values for the self-axis currents were $i_q = 1$, 2, 5, 8 A. The dc-current values injected in the cross-axis remain the same as for the ones used in the d-axis test. Fig. 4.50 shows the averaged points obtained from the test with cross-axis currents of $i_d = 0$ A and $i_d = 8$ A.

The Fig. 4.50 shows that the polynomial fit was not applied to the obtained data. Given the amount of points stored from the test, it was not possible to define a clear

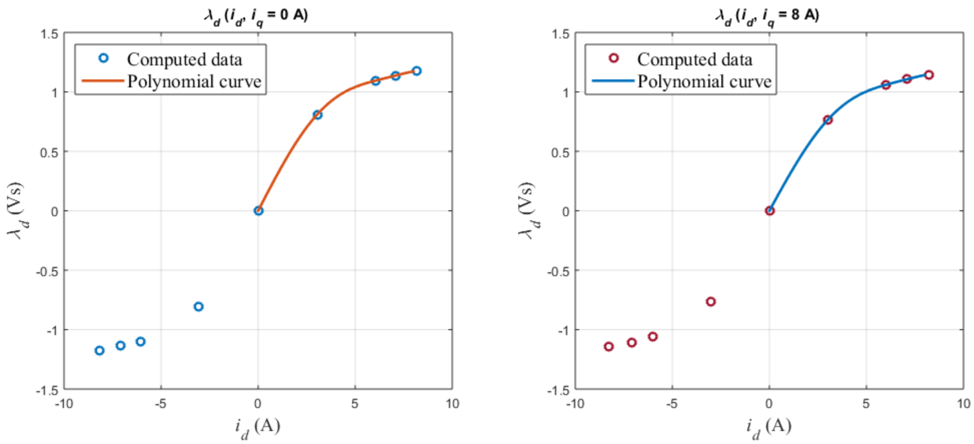

Figure 4.49. Polynomial representation of flux curves in d-axis as a function of i_d at two different cross-axis currents from the square wave current injection test.

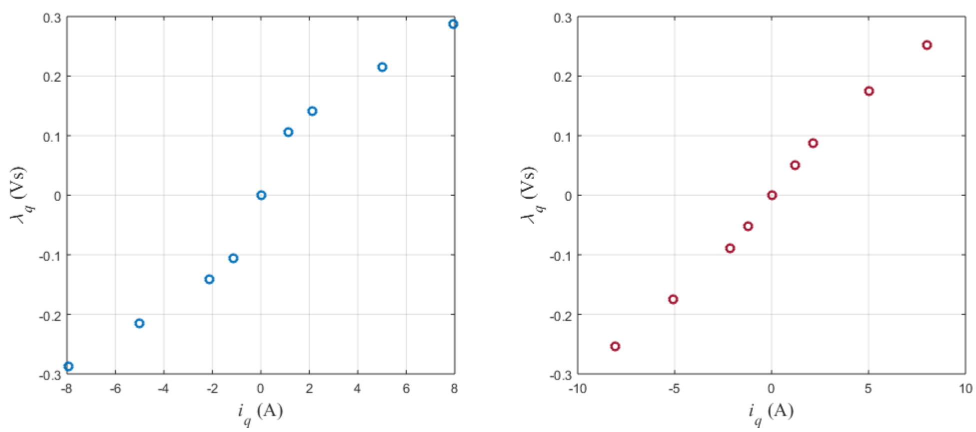

Figure 4.50. Averaged points of flux linkage in q-axis as a function of i_q at two different cross-axis currents from the square wave current injection test.

path, and the *polyfit* tool gave wrong results. This happened due to the high initial slope of the flux, that is, at currents close to zero, a small increase in the current produces higher increase in the flux. When current is further increased, saturation in q-axis causes the non-linear behaviour with a change in the slope. This phenomenon occurs at values of current less than 1 A. In order to identify the trend in that zone of the flux curve, square wave currents with amplitude values less than 1 A must be applied. However, as shown in Fig. 4.51, the small current would cause that the measurements and the estimation become noise-sensitive, and high distortion is present in the results. As a solution, the results from sinusoidal current injection test

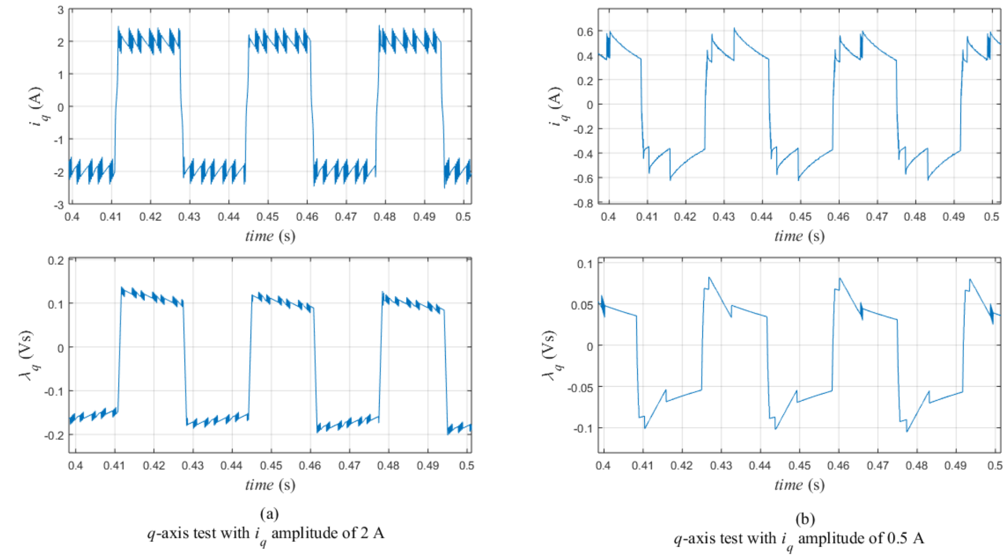

Figure 4.51. Measured current and estimated flux at zero cross-axis current and self-axis square wave current with (a) 2 A amplitude and (b) 0.5 A amplitude.

can be used to define the initial part of the flux curve, as continuous data is obtained from that test. Then, it can be concatenated to the curve obtained by the square wave current injection test. Fig. 4.52 shows the results from the proposed approach.

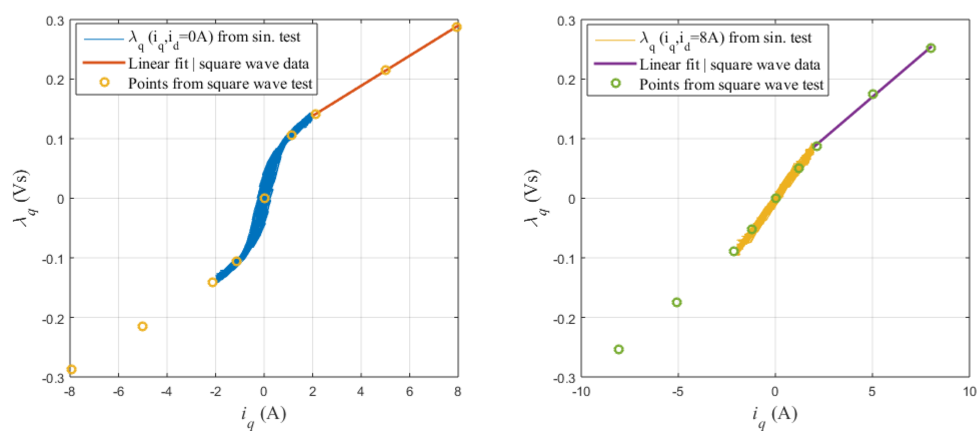

Figure 4.52. Polynomial representation of flux curves in q-axis as a function of i_q at two different cross-axis currents obtained with sinusoidal and square wave current injection tests.

Fig. 4.53 shows the flux maps obtained by computing the fitted curves at different cross-axis currents. These flux maps are obtained in the same way as the ones in the sinusoidal current injection test.

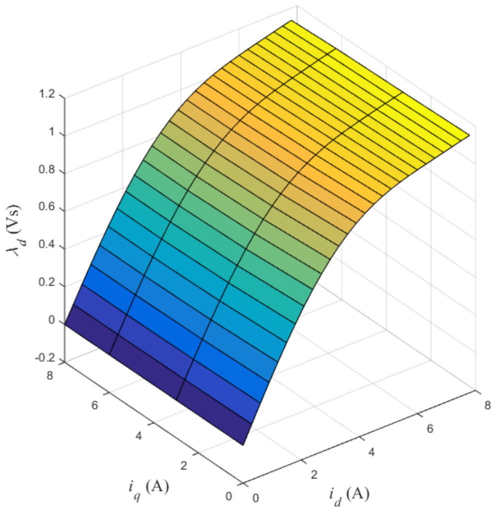

Figure 4.53. Flux maps obtained from the square wave current injection test for the 3 kW ABB SynRM

Apparent, self-incremental and cross-incremental inductances are obtained following the same procedure as in previous chapters, and they are shown in the figs. 4.54, 4.55 and 4.56, respectively. The profile obtained for L_d^{app} in the square wave current injection test presents higher initial values than the ones obtained with sinusoidal current injection, but they present approximately the same values at the maximum current. For the self-incremental inductance l_d^{inc}, its initial value is also higher than the one given from sinusoidal current injection test, but they are lower for currents

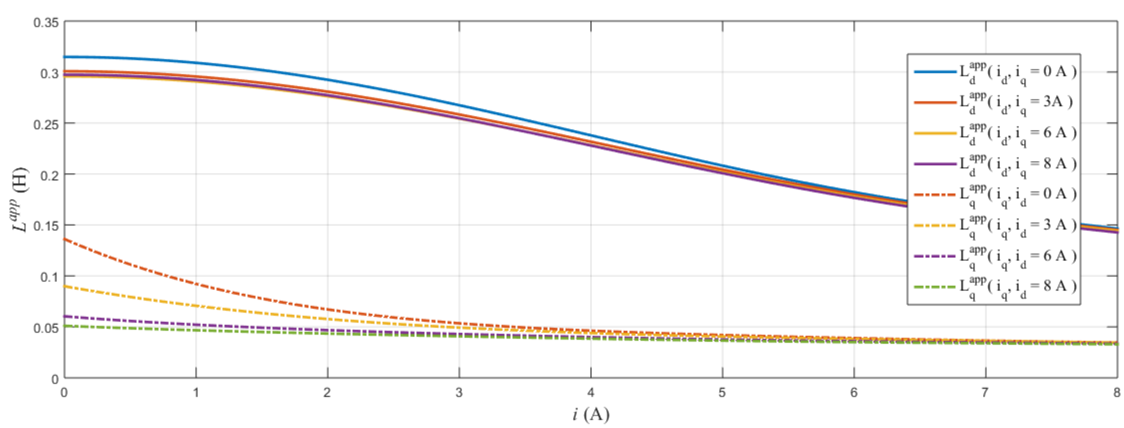

Figure 4.54. Apparent inductances obtained from the square wave current injection test for the 3 kW ABB SynRM

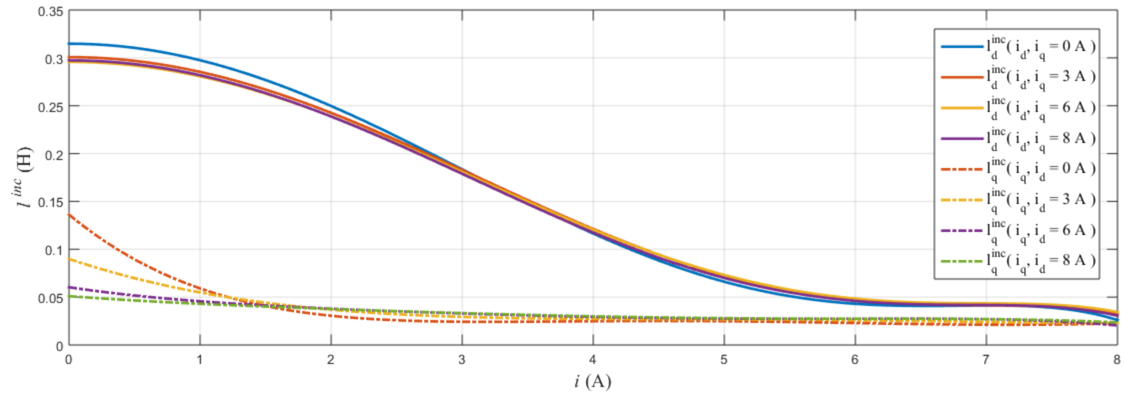

Figure 4.55. Self-incremental inductances obtained from the square wave current injection test for the 3 kW ABB SynRM

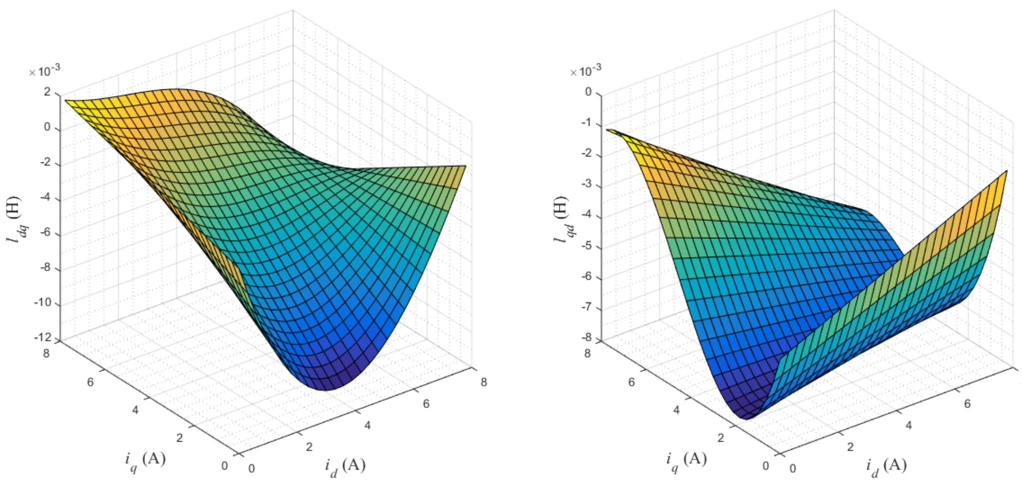

Figure 4.56. Cross-incremental inductances obtained from the square wave current injection test for the 3 kW ABB SynRM

larger than 5 A. There is not significant difference in the inductance profile for L_q^{app} and l_q^{inc} for both current injection tests, and the cross-incremental inductances follow a similar pattern.

Variation in the rotor position

Fig. 4.57 shows the rotor angle, estimated electromagnetic torque and speed during the square wave current injection test at maximum self- and cross-axis current values (8 A). The rotor angle is computed following the same procedure as in Fig.

4.47, and it presents oscillations around the initial rotor position, but these are not larger than 2.5 electrical degrees. Torque and speed present the expected behaviour, with a pulsating periodic waveform with zero-average value.

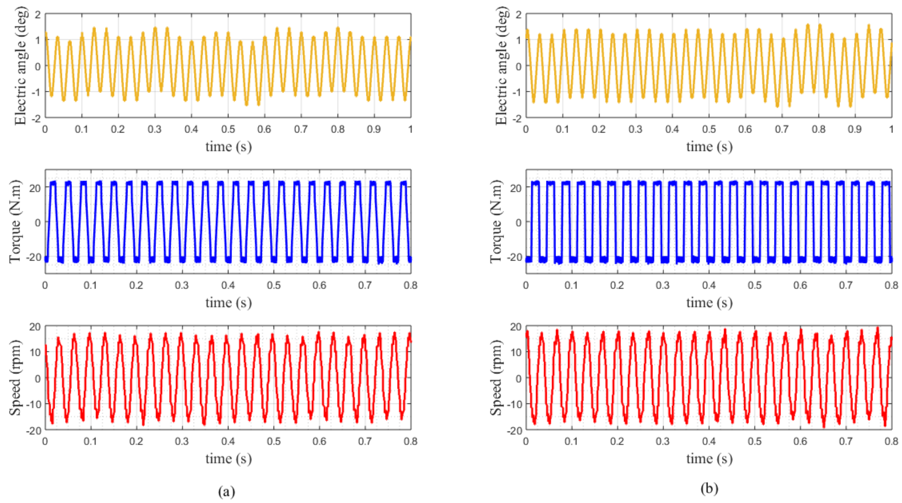

Figure 4.57. Variation in the rotor position, torque and speed during the square wave current injection test at self-axis current of 8 A and cross-axis current of 8 A.

4.3.3 Evaluation of the accuracy of the obtained inductance profiles

The accuracy of the inductance profiles obtained by both current injection tests is evaluated in laboratory conditions. The experimental test follows the same procedure as the one applied to the KSB motor. First, reference currents for MTPA are computed with the algorithm from Fig. 4.32. Then, the auxiliary IM drive is set in speed control mode while the 3 kW ABB SynRM is driven in torque control mode with a PCC strategy. The PCC is set using the apparent and incremental inductances obtained from each current injection test and the prediction error and current THD are obtained. A reduced prediction error and THD represents a better performance in the predictive control and thus a higher accuracy in the parameters.

Generation of reference currents

The algorithm from Fig. 4.32 is applied using $i_{s,initial} = 0$ A, $i_{s,max} = 7.1 \times \sqrt{2} = 10.04 \approx 10$ A and $\Delta i_s = 0.1$ A. For the load angle $\varphi_{initial} = 45°$, $\varphi_{max} = 80°$ and $\Delta\varphi = 0.1°$ were used. Fig. 4.58 shows the reference i_d and i_q currents as a function of the torque for the 3 kW ABB motor.

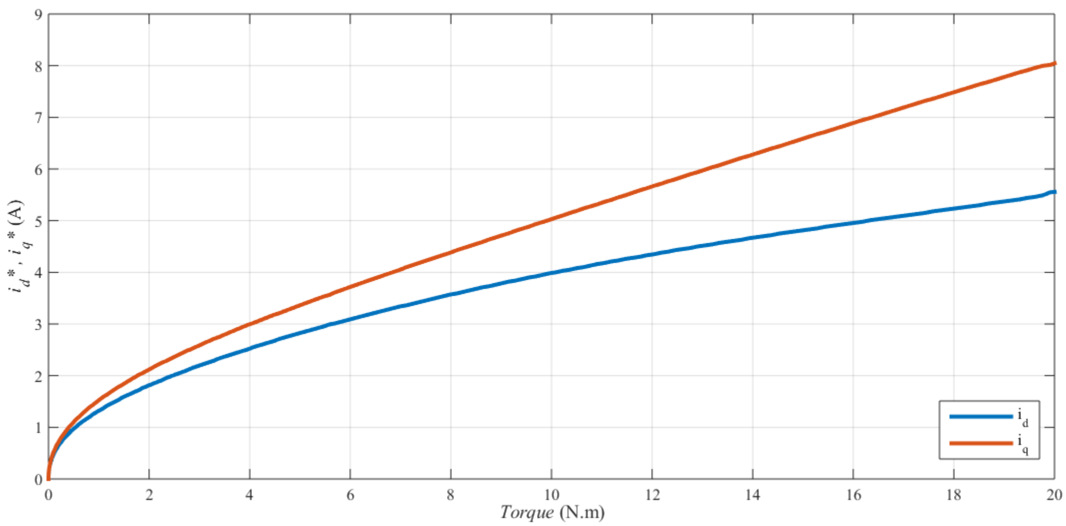

Figure 4.58. Reference currents of the MTPA for the 3 kW ABB SynRM

Motor operation in torque control mode

Once the values of the reference currents i_d and i_q are set in the PCC with the calculated inductances, an initial operating point was set in the motor load to evaluate the response of the drive. The system was run at 1200 rpm and a torque reference of 18 N.m. Fig. 4.59 shows the measured currents, estimated electromagnetic torque and prediction errors using the inductance profile from the sinusoidal and square wave current injection tests. The currents in all cases present a correct sinusoidal shape with minimum distortion. The THD for each case is not greater than 2.5 % as shown in table 4.7. The prediction error in i_d remains under 0.5 A for the operation with the inductances from both current injection tests, but the error in i_q reaches peaks up to 0.5 A, and higher peaks around 0.7 A in the operation with inductances obtained in square wave current injection test. However, this result is acceptable for the PCC operation. The estimated torque follows the reference set for the operation with both inductance profiles with a slightly higher torque ripple based on the inductances from square wave current injection.

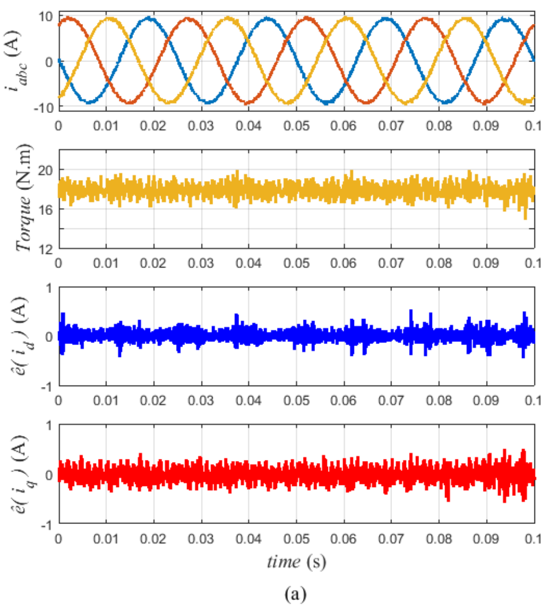

Figure 4.59. Measured line currents, estimated electromagnetic torque and prediction errors at 18 N.m and 1200 rpm using the inductance profile obtained from (a) sinusoidal current injection test and (b) square wave current injection test - 3 kW ABB SynRM

Table 4.7: Total current harmonic distortion in the measured currents using the obtained inductances in current injection tests

THDi	Sinusoidal current injection test	Square wave current injection test
$THD(i_a)(\%)$	1.86	2.27
$THD(i_b)(\%)$	1.90	1.97
$THD(i_c)(\%)$	1.99	1.98

For testing different operating points, the torque reference was set as $T = \{1, 5, 10, 15, 18\}$ N.m, while the auxiliary drive was driven at different speeds $\omega_m = \{250, 750, 1200\}$ rpm. Fig. 4.60 shows the error in estimated current for d- and q-axes. The difference in estimated d-axis current increases with the load as the case given for the KSB motor, but it is inferior than 0.15 A for all operating point. The q-axis current presents estimation errors no larger than 0.25 A. These results represent a good match between estimated and measured currents.

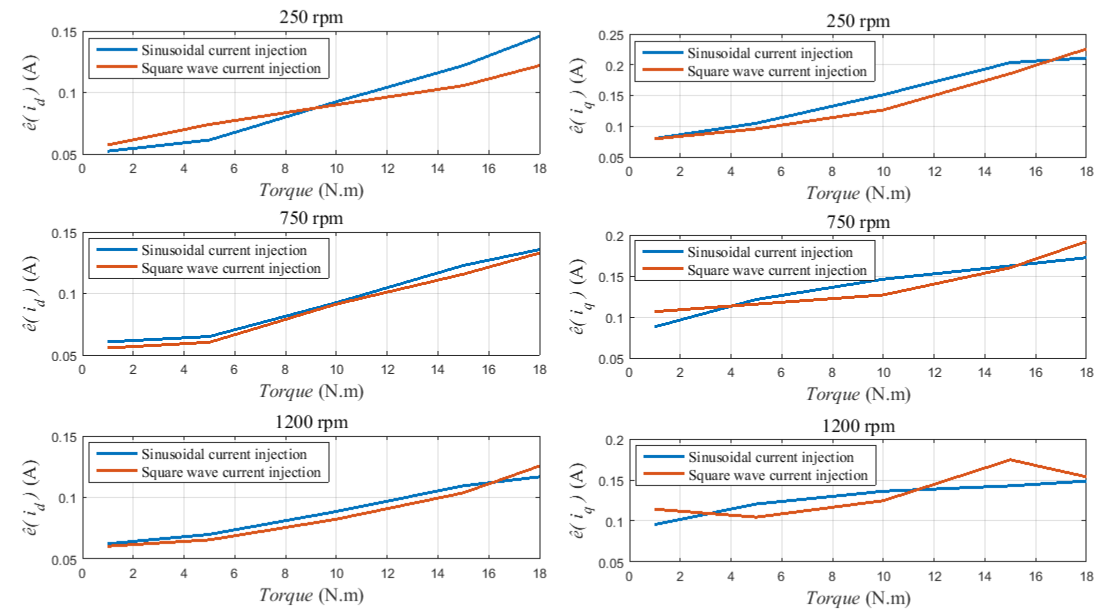

Figure 4.60. Prediction error in d- and q-axis currents— 3 kW ABB SynRM

The THD at different operating points are presented in Fig. 4.61. As before, the distortion has larger effects for low speed low torque operation, with values up to 7 % in the lowest speed, but reaching no more than 2.5 % for higher values.

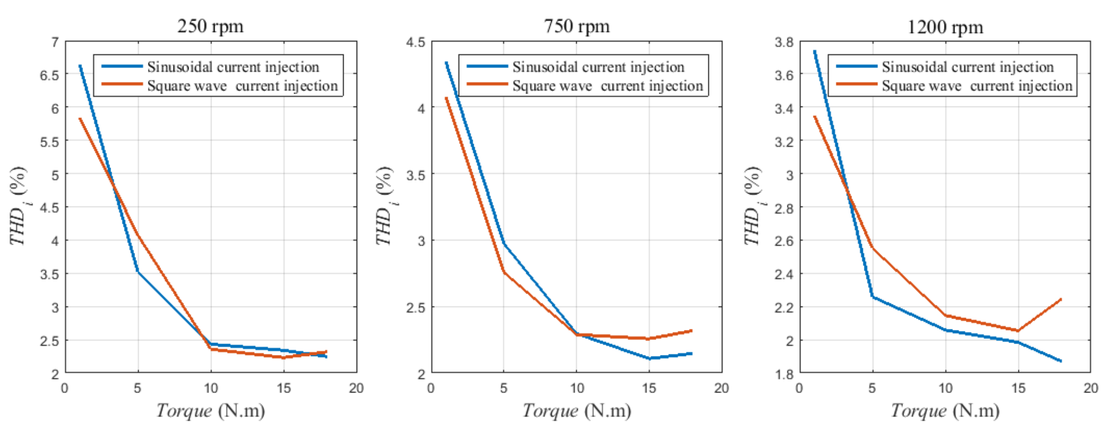

Figure 4.61. THD of current — 3 kW ABB SynRM

Selection of the self-commissioning method

From the obtained results, it is possible to conclude that both tests produce similar outputs with no appreciable impact on the operating conditions and performance of the drive system. Square wave current injection test produced slightly better results for the KSB SynRM, however, the test itself required the injection of 48 signals considering the different square wave amplitudes at each cross-axis current. This causes a longer time with pulsating signals being injected into the machine, requiring also a higher computational memory for storing all the files from test to do the post-processing analysis.

In case of the 3 kW ABB motor, results for inductances from square wave current injection did not produce a much better performance. Although the prediction error was slightly reduced, the torque ripple and current THD at higher reference speed and torque were higher. Besides, the amplitudes of square wave current references were not enough to define the flux curve in the q-axis test, requiring additional data taken from sinusoidal current injection test. Despite the test allows to represent the flux curves in d-axis easily, its complexity for the q-axis post-processing and during the test itself does not compensate the slight increase in the accuracy of the results.

Unlike square wave test, sinusoidal test required the injection of 8 signals, saving memory storage space and producing a smoother response regarding vibrations and audible noise. The accuracy in the results are comparable to the square wave current injection test, requiring less time for the test. It was decided that sinusoidal injection through PCC strategy is the method to apply in the remaining motor since results are accurate enough, the test is faster and allows the machine to work under less stress caused by the pulsating step-like currents.

4.4 Self-commissioning applied to a 11 kW ABB SynRM

The 11 kW ABB SynRM is shown in Fig. 4.62. Given its larger dimensions, it cannot be mounted in the test rig or coupled to the auxiliary drive, therefore the test is done for a free-rotor condition.

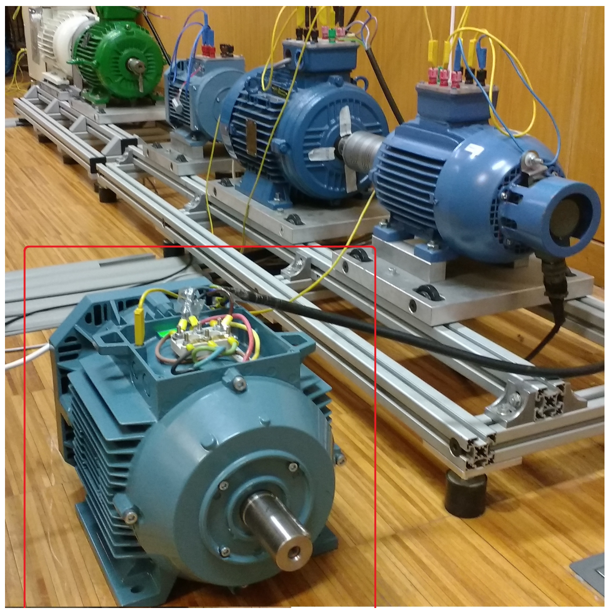

Figure 4.62. 11 kW ABB SynRM not coupled to the auxiliary drive

The stator resistance is measured following the same procedure as in previous sections, resulting in a resistance value per phase of 0.392 Ω.

4.4.1 Restrictions and limitations

According to the motor nameplate, the amplitude of the rated current is $25\times\sqrt{2} = 35.35$ A, therefore, a current protection around that value should be included in the test. However, the maximum current that the available protection devices and equipment can withstand is close to 20 A, limiting the maximum injected current for this test.

The solution here adopted is the application of sinusoidal current injection test for self-commissioning up to the maximum allowable current value. Then, extrapolation can be applied following the same pattern as previous results, especially for the 3 kW ABB motor, which is from the same manufacturer. Results can be partially validated by operating the motor in speed control mode at free-shaft condition. The commissioning results would require an update before using the motor under full load condition, but its operation will be guaranteed up to the tested values.

4.4.2 Sinusoidal current injection test

Sinusoidal current with a frequency of 30 Hz is set as a reference in the PCC following the set-up in Fig. 4.4, as it was previously done for the two 3 kW motors. The amplitude of the sinusoidal waveform applied to each axis should be chosen around 80 % of the rated current amplitude, that is $0.8 \times 25 \times \sqrt{2} = 28.28$ A. However, given the hardware limitations of the test, this amplitude has to be lowered to avoid line currents over 20 A. The maximum amplitude for the reference sinusoidal current and the cross-axis dc current is chosen as 15 A. Moreover, the inductances are totally unknown, making the PCC to work with the inductances calculated for one of the previous tests. This adds an extra limitation because the polynomials generated for other motors only guarantee a stable behaviour under the current range defined for themselves. For instance, if the inductances from the 3 kW ABB motor were used, currents above 8 A should be avoided.

As a consequence, a preliminary test must be done. This consist on the application of sinusoidal injection test up to the limit defined by the inductances employed. This allows to identify an initial value for the apparent and incremental inductances, considering a linear flux behaviour for low current operation. The PCC is then configured with a constant value equal to the identified initial value for the apparent and self-incremental inductances, while the cross-incremental inductances are set as zero. Then, the sinusoidal current injection test can be done setting the sinusoidal amplitude up to the limit restricted by the protections. If no hardware limitation were present, it should be repeated until the applied self- and cross-axis currents would cover the full identification range (28 A in sine amplitude and dc-current).

The initial inductances were found to be $L_d^{app} = l_d^{inc} = 0.1$ H and $L_q^{app} = l_q^{inc} = 0.05$

H. Fig. 4.63 shows the estimated flux curves using constant values for apparent and self-incremental inductances. The test was performed with a sinusoidal amplitude of 15 A as reference current in the self-axis and dc values of {0, 5, 10, 15} A in the cross-axis current reference. Fig. 4.63 shows the plots for sinusoidal injection tests at cross-axis currents of 0 A and 15 A. In the case of q-axis test, this value is more than enough to define the whole flux curve at a given cross-axis current because the saturation occurs at very low current values, followed by an approximately constant slope curve. For the d-axis flux curves, however, it requires a full current range to totally identify its behaviour. To complete the curve, some virtual points are added to give an assumed path to the Matlab *polyfit* tool. Fig. 4.63 illustrates also the curves from polynomial fitting covering the identification range.

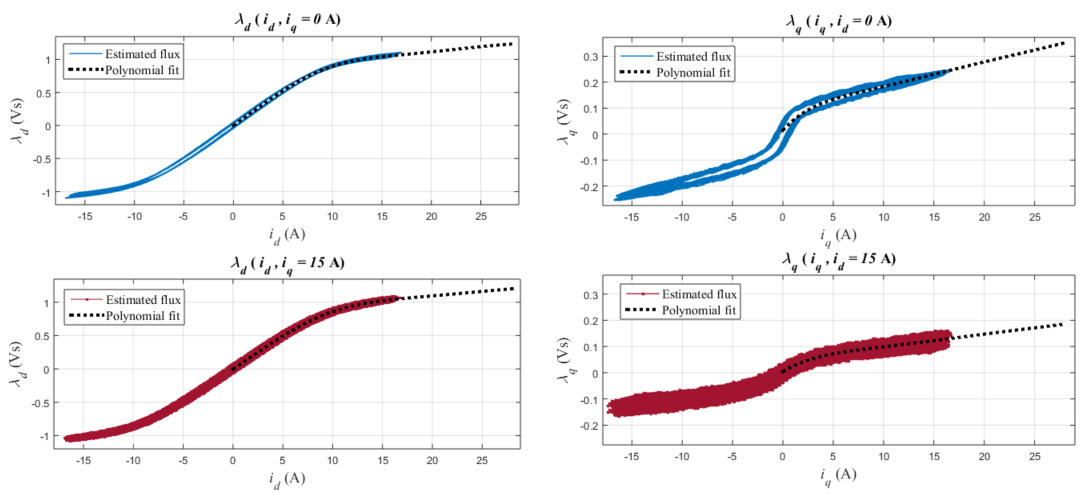

Figure 4.63. Polynomial fitting in d-axis and q-axis at different dc currents for the 11 kW motor

Based on these fitting results, the equations of the flux curves are represented by polynomials order seven, as the one presented in 4.1. Tables 4.8 and 4.9 show the resulting coefficients.

Flux maps are plotted in Fig. 4.64 using the obtained polynomial representation of flux curves and the Matlab tool *surf*. It is worth to notice that the flux surfaces are not extrapolated with respect to the cross-axis current. For instance, in case of $\lambda_d(i_d, i_q)$, the extrapolation covered all the range until $i_d = 28$ A, but it only reached the tested $i_q = 15$ A. This was not done because the motor is not planned to be

Table 4.8: Coefficients for polynomial representation of $\lambda_d(i_d)$ of the 11 kW ABB SynRM

	p_1	p_2	p_3	p_4	p_5	p_6	p_7	p_8	p_9
$i_q = 0$ **A**	-7.34E-11	1.00E-08	-5.38E-07	1.42E-05	-1.78E-04	7.77E-04	-1.48E-03	1.07E-01	9.26E-04
$i_q = 5$ **A**	-7.08E-11	9.74E-09	-5.31E-07	1.43E-05	-1.88E-04	9.54E-04	-2.51E-03	1.07E-01	-5.50E-03
$i_q = 10$ **A**	-6.45E-11	8.85E-09	-4.82E-07	1.30E-05	-1.71E-04	8.54E-04	-2.26E-03	1.05E-01	-3.83E-03
$i_q = 15$ **A**	-4.06E-11	5.69E-09	-3.15E-07	8.51E-06	-1.07E-04	4.01E-04	-7.56E-04	1.02E-01	-4.17E-03

Table 4.9: Coefficients for polynomial representation of $\lambda_q(i_q)$ of the 11 kW ABB SynRM

	r_1	r_2	r_3	r_4	r_5	r_6	r_7	r_8
$i_d = 0$ **A**	5.29E-11	-9.69E-09	7.00E-07	-2.59E-05	5.30E-04	-5.96E-03	4.33E-02	1.44E-02
$i_d = 5$ **A**	3.31E-10	-4.36E-08	2.33E-06	-6.51E-05	1.02E-03	-9.05E-03	4.97E-02	6.21E-03
$i_d = 10$ **A**	1.93E-10	-2.54E-08	1.37E-06	-3.93E-05	6.50E-04	-6.25E-03	3.76E-02	2.36E-03
$i_d = 15$ **A**	1.33E-13	-1.38E-09	1.73E-07	-8.64E-06	2.18E-04	-2.88E-03	2.36E-02	4.17E-03

driven at such levels of current given the hardware restrictions.

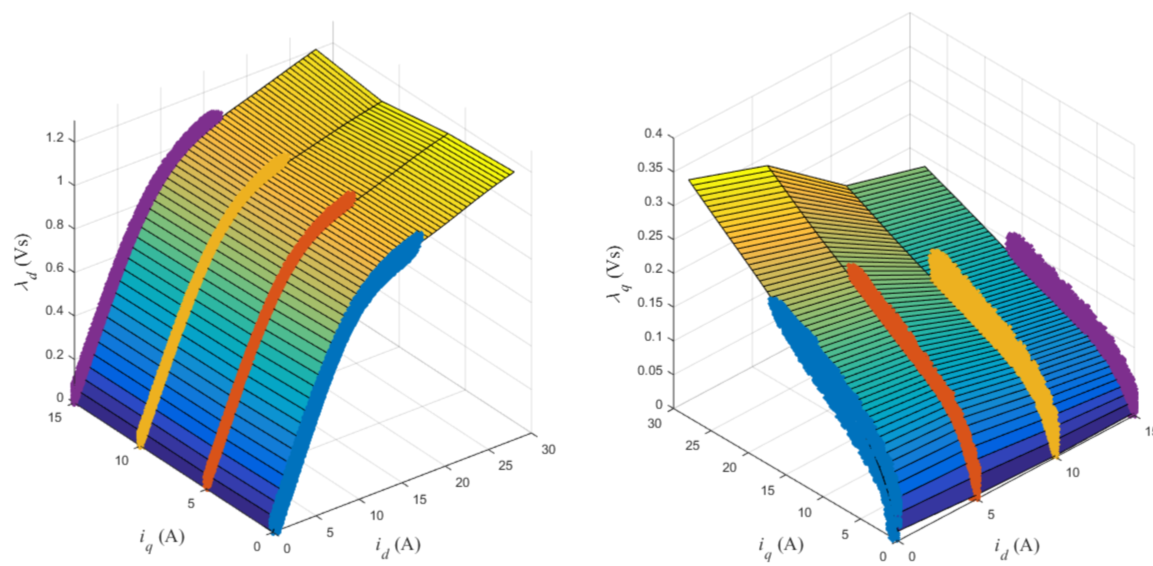

Figure 4.64. Estimated Flux Maps for the 11 kW SynRM

The same procedure as in previous cases is applied: process in (3.10) and (3.11) is done between the polynomials representing the flux curves and the self-axis currents to find the apparent inductances, shown in Fig. 4.65. These inductance profiles follow the expected behaviour based on those obtained with the other motors. The initial value for L_d is approximately 0.105 H, lower than the one computed in the KSB motor

(0.18 H), and the maximum $L_q \approx 0.04$ H, much lower than the homologous case in the previous motors.

The polynomials are then differentiated with respect to the self-axis current to obtain the self-incremental inductances, represented in Fig. 4.66. For q-axis, these inductances present a similar behaviour than L_q^{app}, but the l_d^{inc} curves have a faster decrease until the maximum measured current, then they tend to be constant. This happens due to the approximation chosen by adding virtual points in the polynomial fitting process; given that is not possible to estimate the flux beyond 15 A, the values of inductances are considered constant in the remaining range.

Cross-incremental inductances are computed within the tested current range since their value depends on the differentiation with respect to the cross-axis current. The obtained profiles are shown in Fig. 4.67.

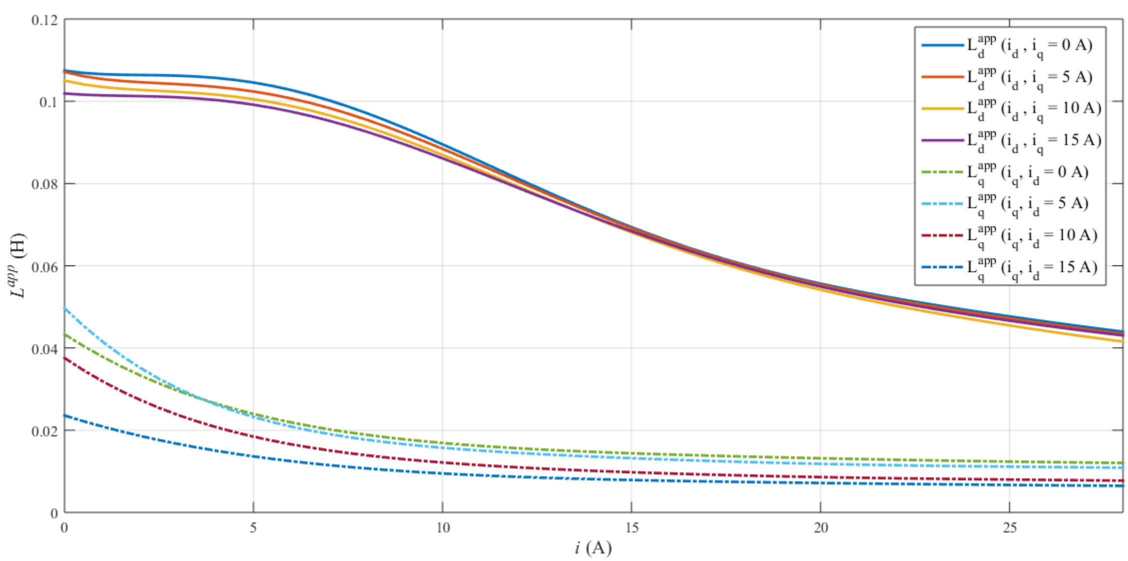

Figure 4.65. Apparent inductances for the 11 kW SynRM

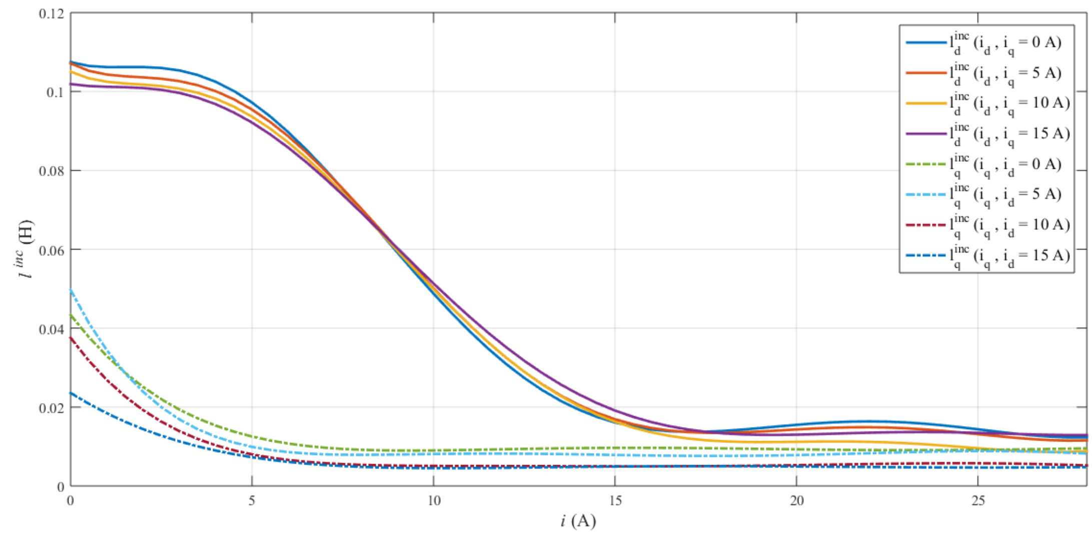

Figure 4.66. Self-incremental inductances for the 11 kW SynRM

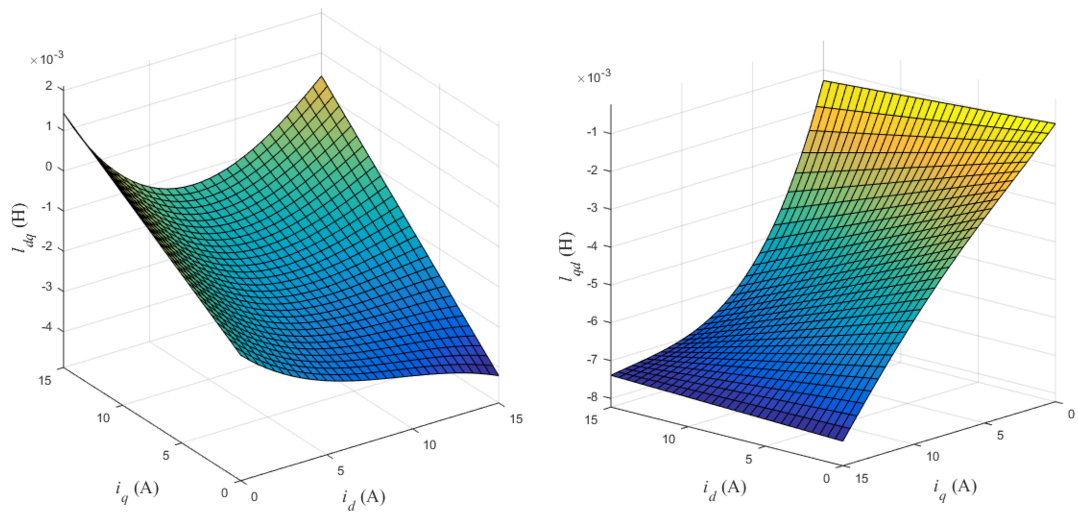

Figure 4.67. Cross-incremental inductances for the 11 kW SynRM

Fig. 4.68 shows the rotor displacement, the estimated electromagnetic torque and the speed during the current injection test. In case of d-axis test at maximum cross-axis dc current, the displacement was around 30 electrical degrees. This value is higher than the ones obtained in previous test but acceptable considering that the 11 kW motor was tested in a free-shaft condition.

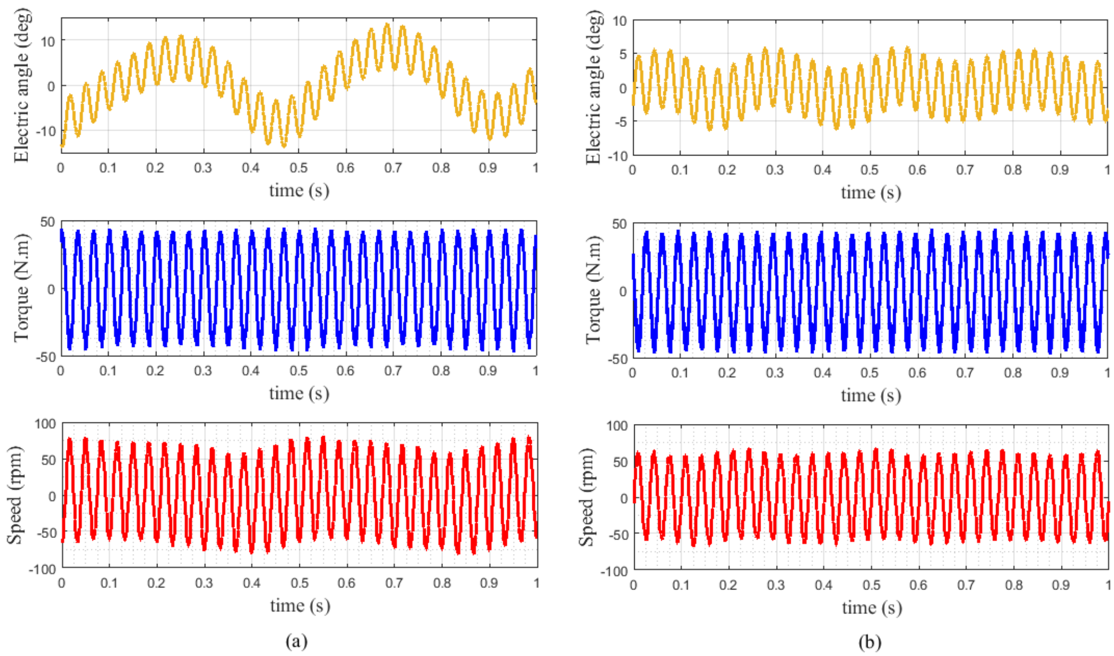

Figure 4.68. Rotor position variation, estimated electromagnetic torque and speed of the 11 kW motor during sinusoidal current injection test for (a) d-axis test with $i_q = 15$ A and (b) q-axis test with $i_d = 15$ A.

4.4.3 Preliminary evaluation of the accuracy of the obtained inductances

Accuracy evaluation of the obtained parameters is not possible by applying the same torque control mode as in previous sections because the motor remains under no load condition. A preliminary test is then applied to evaluate the behaviour with the calculated inductances, at least, within the range defined during the sinusoidal current injection test.

In this case, the SynRM drive and PCC are configured to operate in speed control mode. Speed reference tracking and transient behaviour are evaluated under no-load condition. Current limitations are kept as for the commissioning test, limiting the torque-producing capacity of the motor.

As before, first step consist on the generation of reference currents. Fig. 4.69 shows the reference currents for i_d and i_q as a function of the torque, which were generated following the same procedure in Fig. 4.32 with $i_{s,initial} = 0$ A, $i_{s,max} = 25 \times \sqrt{2} =$

$35.35 \approx 35$ A and $\Delta i_s = 0.1$ A. For the load angle $\varphi_{initial} = 45°$, $\varphi_{max} = 80°$ and $\Delta\varphi = 0.1°$ were used.

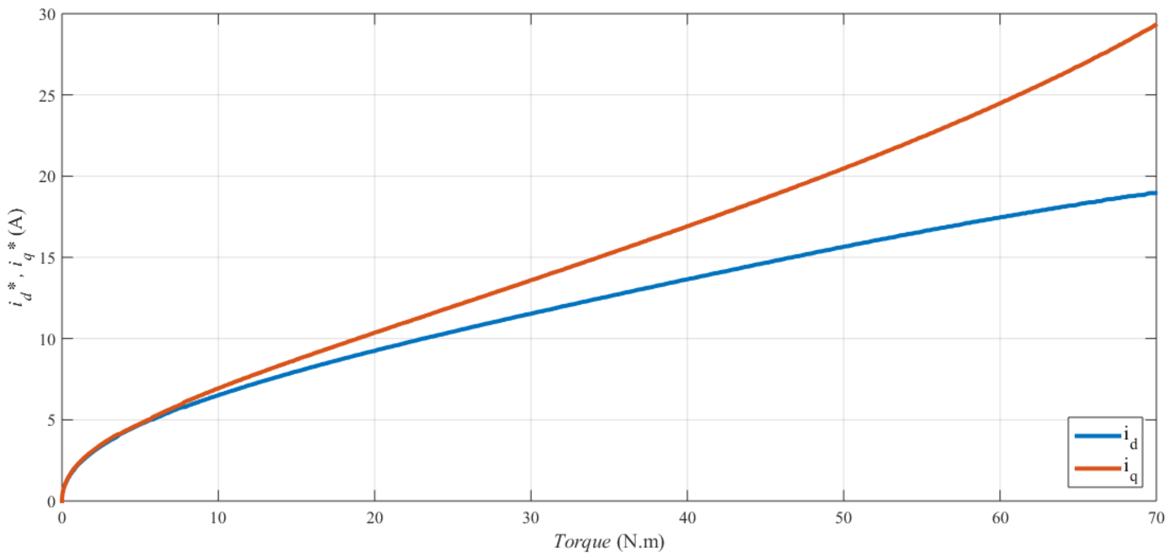

Figure 4.69. Reference currents for MTPA operation on the 11 kW ABB SynRM

Current references and obtained inductances are then set in the PCC. An initial reference speed of 500 rpm is defined to evaluate the starting of the motor. Fig. 4.70(a) shows the results for the acceleration test to 500 rpm. It is shown how the waveforms of the line currents present a smooth sinusoidal shape. The speed follows the reference without overshoots and it takes around 0.2 s to reach the steady state value. Torque, *d*- and *q*-axis currents are also shown in the figure, illustrating an adequate behaviour for the acceleration.

Next, acceleration to 1000 rpm is tested. Fig. 4.70(b) shows how the currents keep a smooth behaviour, and the speed reaches the requested value. However, torque presents a flat behaviour when it reaches 20 N.m. This is caused by the limitation in the currents. The same figure shows how i_q follows the same patter as torque. This means that, under no limitations, the torque produced in acceleration test tend to be higher, causing a faster speed response.

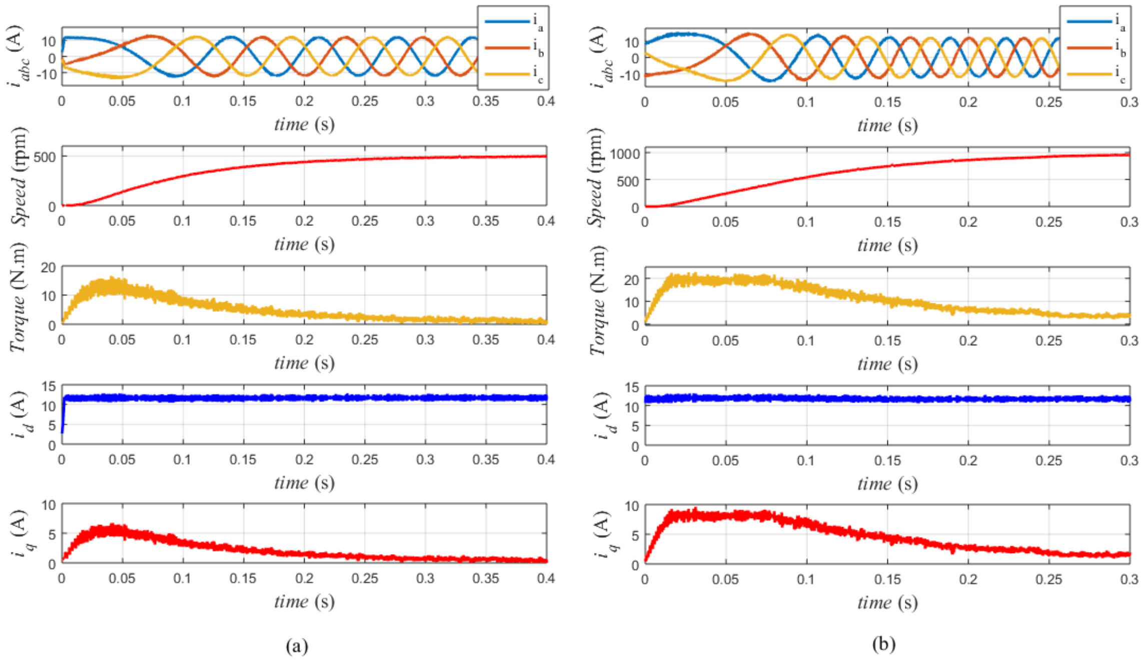

Figure 4.70. Results for acceleration test of the 11 kW motor at (a) 0 to 500 rpm (b) 0 to 1000 rpm

Finally, speed-reversal test was performed. The motor is run at 800 rpm with a step reference set to -800 rpm. After steady state is reached, the reference is changed again to 800 rpm. Fig. 4.71 shows the results. Again, the currents present a smooth sinusoidal shape, while the torque and q-axis current increase up to a limited value to generate the change in the speed. The measured speed reaches its steady state value in around 0.35 s. This transient response could be faster if the motor was able to operate under rated conditions, reaching up to its maximum torque of 70 N.m.

Although preliminary results are satisfactory, the 11 kW motor cannot be run under more challenging conditions, since its characterisation is limited to the current window here exposed, and the evaluation of accuracy only considered speed control in no-load condition. Prior the operation in torque control mode, the sinusoidal current injection test must be repeated considering the full range, and inductance profiles must be updated in the PCC setup.

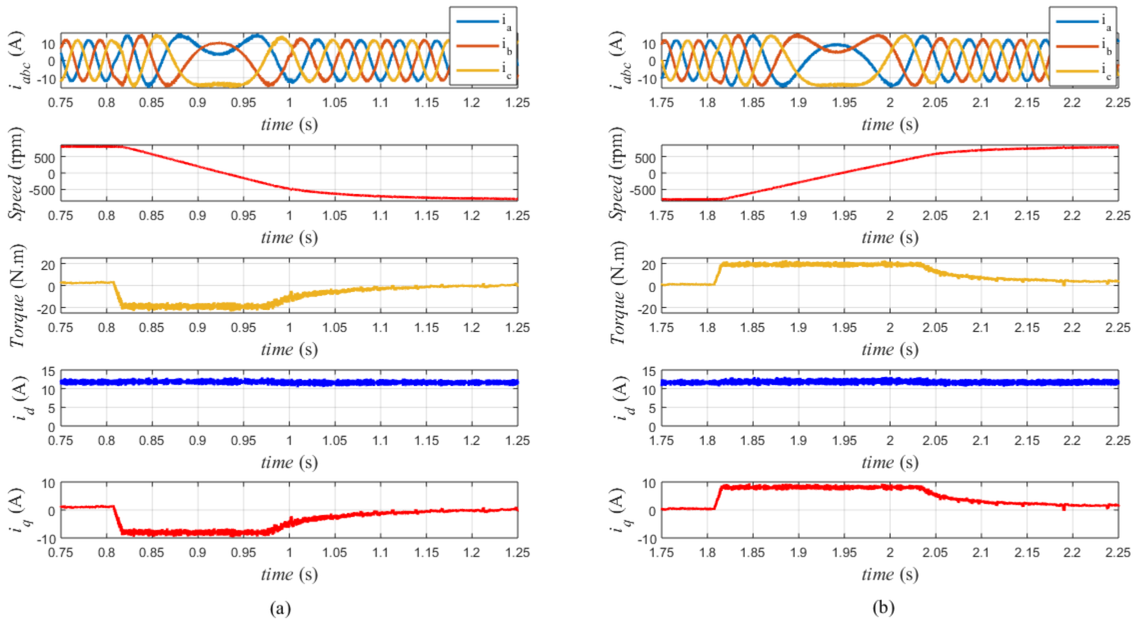

Figure 4.71. Results for acceleration-deceleration test of the 11 kW motor (a) 800 rpm to -800 rpm (b) -800 rpm to 800 rpm

.

Chapter 5

CONCLUSION AND FUTURE WORK

5.1 Conclusion

The self-commissioning of SynRM drives was studied in this thesis work. The major goal was the analysis of standstill identification strategies of the magnetic model of SynRMs. Two identification techniques were adopted for the calculation of the apparent and incremental inductances considering saturation and cross-saturation effects. The sinusoidal and square wave current injection techniques were applied to two 3 kW SynRMs from different manufacturers with a control strategy based on predictive current control algorithm. The motors were fed by an inverter with a sequence of sinusoidal and square wave current pulses that were first applied to the rotor d- and q-axes separately at different dc currents on the q- and d-axes, respectively. The stator flux linkages were estimated by integrating the induced voltages. Using the current and flux samples, a polynomial representation of the flux was defined, thus allowing to calculate apparent and incremental inductances from the polynomial function. The same procedure was applied to a 11 kW SynRM considering only sinusoidal current injection test.

The current injection tests for the drives based on PCC required the setting of the motor parameters, most of them taken from the nameplate data. Only stator resistance and inductance profile must be identified prior the test. However, if the information about the parameters is not available, prediction errors will not be significant if a rough estimation is done, i.e., apparent and self-inductances can be assumed as constant, but still producing a current reference tracking of the PCC system. For the inductance profile, apparent and self-incremental inductances can be initially assumed as constants while cross-incremental inductances can be neglected. In the case of the 3 kW motors, parameters previously estimated for one of the motors were used while constant values were assumed for the 11 kW motor given its higher rated current.

Regarding the sinusoidal current injection test, sinusoidal reference current with an amplitude of 80 % of the motor rated current was applied along the d-axis, with four values of dc current applied in the q-axis. The same procedure was repeated with the same sinusoidal amplitude along q-axis and dc currents along d-axis. This method allowed to identify the flux curves in both d- and q-axes neglecting the effect of iron losses. Only 8 injection tests and reasonable memory and computational resources were used. It is worth to highlight that this technique produced a quasi-standstill condition in the motors under test, with a rotor displacements no higher than 30 electrical degrees for the test in the 11 kW motor, whose shaft was uncoupled from any mechanical load.

Square wave current injection tests considered the simultaneous application of square wave currents in the self-axis and dc currents in the cross-axis. Unlike sinusoidal current injection test, this technique does not make any assumption over the iron losses in the SynRMs because the constant-like interval of the square wave current produces a steady-state condition along the inductance in the equivalent circuit of Fig. 2.3. This allowed to compute the flux linkage in an operating point given by the amplitude of the square waveform. Thus, the reference current must be set at different amplitudes, each of them representing a discrete point of the flux curve, which is reconstructed by joining the points. As for the sinusoidal current injection technique, flux curves are represented by polynomials, and apparent and incremental inductances were computed from the resulting polynomial. To improve the curve fitting, it is important to consider a proper interval between the points, i.e. between the values of the amplitude of the square wave currents; a narrower step would improve the fit and accuracy in inductance calculation, but it would require to perform more tests injecting current, thus increasing the stress in the motor caused by pulsating currents (and torque). In the case of the two motor tested in this thesis, the steps were chosen depending on the axis under identification: for the d-axis test, a narrower interval was considered for high values of current (more than 50 % of maximum current) due to the nonlinear behaviour of the curve at those values, while only a couple of points were enough to define the flux curve at low currents because it can be approximate to a linear function. For the q-axis test, conversely, flux curve could be assumed as linear at high currents, while it presented a change in the slope at low currents, requiring a narrower step. The process for obtaining the q-axis flux curves presented a challenge in the 3 kW ABB SynRM because the discrete points at low currents were not close enough to define a path for the polynomial fitting tool. Since the use of lower currents would make the estimation noise sensitive, the information from the sinusoidal current injection test was taken to fulfil the identification range at those currents.

The accuracy of the obtained inductances for the 3 kW motors was evaluated experimentally in a test rig, running the SynRM drives in torque control mode by the PCC strategy. The performance of the drives set with the parameters from the two self-commissioning strategies were compared based on the prediction error of the currents and the THD of the line currents. It was found that the inductances obtained from the square wave current injection test did not produce more accurate results, i.e., the results were not considerably different with both inductance profiles, but the test and post-processing were more challenging using square waveforms. The latest required up to 48 injection tests, increasing the memory, computational resources and time the motors withstood pulsating currents and torque. Therefore, sinusoidal current injection test was chosen as the most convenient technique for inductance calculation with a good accuracy for predictive control based SynRM drives.

5.2 Future work

The scope for future work to build upon the present work is listed as follows:

- The concept of self-commissioning is intended to accurate identify the parameters of the machine connected to it without any user intervention or additional equipment. However, during the current injection tests in this thesis the amplitudes of the sinusoidal and square wave references as well as the values of the reference cross-axis dc currents were manually set by the user through ControlDesk plattform. In the interest of self-commissioning, an algorithm to inject automatically the current references during the current injection tests can be developed. This would allow to identify the flux curves based on the required cycles with a minimum amount of flux and current samples, thus reducing the the time of the test, the time the pulsating currents are injected in the motor and the required memory capacity to store the generated files.

- The number of dc-bias injected currents on the cross-axis was chosen by a trial and error process. An automatic process to determine this number could reduce the time of the test and the time dc current is injected along the motor windings without affecting the accuracy of the test.

- One of the features of self-commissioning of electric drives is the possibility to perform the parameter identification at standstill. The injection of dc current prior the test to align the rotor along the d-axis to define a zero-position goes against this concept. An algorithm to identify the initial rotor position can be developed to avoid the need of injecting this current prior the tests.

5.3 Quality report

Thesis development at the Instituto de Telecomunicações - Universidade de Coimbra was of a high academic, technical and personal development value. The study of

SynRMs and applied control strategies is on the state-of-the-art of electric drives for applications of high interest such as hybrid and electric vehicles.

The study of the self-commissioning of SynRM drives was possible thanks to a complete set of laboratory equipment and the academic support provided in terms of guidance from the thesis supervisor and the members of the research group. The most remarkable experience was the possibility to work beyond the simulations, understanding and solving practical issues which are not possible to cover during academic lectures.

I would recommend to both sides of agreement to continue this partnership along with the same organisation in terms of academic, administrative or technical issues. This experience would be highly beneficial not only for the enhancement of research topics, but also for the professional development of master students.

Bibliography

[1] S. A. Odhano, *Self-Commissioning of AC Motor Drives.* PhD thesis, Politecnico di Torino, 2014.

[2] Z. Q. Zhu and D. Howe, "Electrical Machines and Drives for Electric, Hybrid, and Fuel Cell Vehicles," *Proceedings of the IEEE*, vol. 95, pp. 746–765, Apr. 2007.

[3] S. A. Odhano, P. Giangrande, R. I. Bojoi, and C. Gerada, "Self-Commissioning of Interior Permanent- Magnet Synchronous Motor Drives With High-Frequency Current Injection," *IEEE Transactions on Industry Applications*, vol. 50, pp. 3295–3303, Sept. 2014.

[4] S. A. Odhano, R. Bojoi, M. Popescu, and A. Tenconi, "Parameter identification and self-commissioning of AC permanent magnet machines-A review," in *Electrical Machines Design, Control and Diagnosis (WEMDCD), 2015 IEEE Workshop on*, pp. 195–203, IEEE, 2015.

[5] H. Schierling, "Self-commissioning-a novel feature of modern inverter-fed induction motor drives," in *Third International Conference on Power Electronics and Variable-Speed Drives*, pp. 287–290, July 1988.

[6] T. Jahns, "Getting Rare-Earth Magnets Out of EV Traction Machines: A review of the many approaches being pursued to minimize or eliminate rare-earth magnets from future EV drivetrains," *IEEE Electrification Magazine*, vol. 5, pp. 6–18, Mar. 2017.

[7] M. Ferrari, N. Bianchi, A. Doria, and E. Fornasiero, "Design of Synchronous Reluctance Motor for Hybrid Electric Vehicles," *IEEE Transactions on Industry Applications*, vol. 51, pp. 3030–3040, July 2015.

[8] G. Pellegrino, T. M. Jahns, N. Bianchi, W. Soong, and F. Cupertino, *The Rediscovery of Synchronous Reluctance and Ferrite Permanent Magnet Motors.* SpringerBriefs in Electrical and Computer Engineering, Cham: Springer International Publishing, 2016. DOI: 10.1007/978-3-319-32202-5.

[9] A. Vagati, G. Franceschini, I. Marongiu, and G. P. Troglia, "Design criteria of high performance synchronous reluctance motors," in *Conference Record of the 1992 IEEE Industry Applications Society Annual Meeting*, pp. 66–73 vol.1, Oct. 1992.

[10] T. Matsuo and T. A. Lipo, "Field oriented control of synchronous reluctance machine," in *, 24th Annual IEEE Power Electronics Specialists Conference, 1993. PESC '93 Record*, pp. 425–431, June 1993.

[11] A. Vagati, M. Pastorelli, G. Francheschini, and S. C. Petrache, "Design of low-torque-ripple synchronous reluctance motors," *IEEE Transactions on Industry Applications*, vol. 34, pp. 758–765, July 1998.

[12] Z. Qu, T. Tuovinen, and M. Hinkkanen, "Inclusion of magnetic saturation in dynamic models of synchronous reluctance motors," in *2012 XXth International Conference on Electrical Machines (ICEM)*, pp. 994–1000, 2012.

[13] A. P. Goncalves, S. M. A. Cruz, F. Ferreira, A. M. S. Mendes, and A. T. De Almeida, "Synchronous Reluctance Motor Drive for Electric Vehicles Including Cross-Magnetic Saturation," in *2014 IEEE Vehicle Power and Propulsion Conference (VPPC)*, pp. 1–6, 2014.

[14] S. Taghavi and S. Taghavi, *Design of Synchronous Reluctance Machines for Automotive Applications*. PhD thesis, Concordia University, Mar. 2015.

[15] M. Bugsch and B. Piepenbreier, "HF Parameter Identification Using Test Current Injection for Sensorless Control of a Synchronous Reluctance Machine (SynRM)," in *18th European Conference on Power Electronics and Applications EPE 2016 ECCE Europe*, (Karlsruhe, Germany), Sept. 2016.

[16] J. K. Kostko, "Polyphase reaction synchronous motors," *Journal of the American Institute of Electrical Engineers*, vol. 42, no. 11, pp. 1162–1168, 1923.

[17] J. Pyrhonen, V. Hrabovcova, and R. S. Semken, *Electrical Machine Drives Control: An Introduction*. John Wiley & Sons, Oct. 2016. Google-Books-ID: zYY9DQAAQBAJ.

[18] J. Faucher, M. Lajoie-Mazenc, and A. Chayegani, "Characterization of a Closed-Loop Controlled Current-Fed Reluctance Machine Taking into Account Saturation," *IEEE Transactions on Industry Applications*, vol. IA-15, pp. 482–488, Sept. 1979.

[19] A. Fratta and A. Vagati, "A reluctance motor drive for high dynamic performance application," *IEEE Transactions on Industry Applications*, vol. 28, pp. 873–879, July 1992.

[20] A. Vagati, "The synchronous reluctance solution: a new alternative in AC drives," in *, 20th International Conference on Industrial Electronics, Control and Instrumentation, 1994. IECON '94*, vol. 1, pp. 1–13 vol.1, Sept. 1994.

[21] S. Morimoto, Shohei Ooi, Y. Inoue, and M. Sanada, "Experimental Evaluation of a Rare-Earth-Free PMASynRM With Ferrite Magnets for Automotive Applications," *IEEE Transactions on Industrial Electronics*, vol. 61, pp. 5749–5756, Oct. 2014.

[22] Haiwei Cai, Bo Guan, and Longya Xu, "Low-Cost Ferrite PM-Assisted Synchronous Reluctance Machine for Electric Vehicles," *IEEE Transactions on Industrial Electronics*, vol. 61, pp. 5741–5748, Oct. 2014.

[23] S. Taghavi and P. Pillay, "A sizing methodology of the synchronous reluctance motor for traction applications," *IEEE Journal of Emerging and Selected Topics in Power Electronics*, vol. 2, no. 2, pp. 329–340, 2014.

[24] N. Urasaki, T. Senjyu, and K. Uezato, "Relationship of parallel model and series model for PMSM including iron loss," in *2001 IEEE 32nd Annual Power Electronics Specialists Conference (IEEE Cat. No.01CH37230)*, vol. 2, pp. 788–793 vol.2, 2001.

[25] K. Yahia, D. Matos, J. O. Estima, and A. M. Cardoso, "Modeling synchronous reluctance motors including saturation, iron losses and mechanical losses," in *Power Electronics, Electrical Drives, Automation and Motion (SPEEDAM), 2014 International Symposium on*, pp. 601–606, IEEE, 2014.

[26] J. A. Santos, D. A. Andrade, G. P. Viajante, M. A. Freitas, F. S. Silva, and V. R. Bernadeli, "Mathematical modeling and computer analysis synchronous reluctance motor," in *Power Electronics Conference and 1st Southern Power Electronics Conference (COBEP/SPEC), 2015 IEEE 13th Brazilian*, pp. 1–5, IEEE, 2015.

[27] G. Zanuso, P. Sandulescu, and L. Peretti, "Self-commissioning of flux linkage curves of synchronous reluctance machines in quasi-standstill condition," *IET Electric Power Applications*, vol. 9, pp. 642–651, Nov. 2015.

[28] W. Xu and R. D. Lorenz, "High-Frequency Injection-Based Stator Flux Linkage and Torque Estimation for DB-DTFC Implementation on IPMSMs Considering Cross-Saturation Effects," *IEEE Transactions on Industry Applications*, vol. 50, pp. 3805–3815, Nov. 2014.

[29] A. Pouramin, R. Dutta, M. F. Rahman, J. E. Fletcher, and D. Xiao, "A preliminary study of the effect of saturation and cross-magnetization on the inductances of a fractional-slot concentrated-wound interior PM synchronous machine," in *2015 IEEE 11th International Conference on Power Electronics and Drive Systems*, pp. 828–833, June 2015.

[30] P. Guglielmi, M. Pastorelli, and A. Vagati, "Impact of cross-saturation in sensorless control of transverse-laminated synchronous reluctance motors," *IEEE Transactions on Industrial Electronics*, vol. 53, pp. 429–439, Apr. 2006.

[31] A. Vagati, M. Pastorelli, F. Scapino, and G. Franceschini, "Impact of cross saturation in synchronous reluctance motors of the transverse-laminated type," *IEEE Transactions on Industry Applications*, vol. 36, no. 4, pp. 1039–1046, 2000.

[32] M. J. Kamper and A. F. Volsdhenk, "Effect of rotor dimensions and cross magnetisation on Ld and Lq inductances of reluctance synchronous machine with cageless flux barrier rotor," *IEE Proceedings - Electric Power Applications*, vol. 141, pp. 213–220, July 1994.

[33] M. N. Ibrahim, P. Sergeant, and E. M. Rashad, "Relevance of Including Saturation and Position Dependence in the Inductances for Accurate Dynamic Modeling and Control of SynRMs," *IEEE Transactions on Industry Applications*, vol. 53, pp. 151–160, Jan. 2017.

[34] A. Varatharajan, "Predictive control of synchronous reluctance machines for traction applications," Master's thesis, University of Oviedo, 2016.

[35] D. Casadei, F. Profumo, G. Serra, and A. Tani, "FOC and DTC: two viable schemes for induction motors torque control," *IEEE Transactions on Power Electronics*, vol. 17, pp. 779–787, Sept. 2002.

[36] P. Cortes, M. P. Kazmierkowski, R. M. Kennel, D. E. Quevedo, and J. Rodriguez, "Predictive Control in Power Electronics and Drives," *IEEE Transactions on Industrial Electronics*, vol. 55, pp. 4312–4324, Dec. 2008.

[37] J. Rodriguez, M. P. Kazmierkowski, J. R. Espinoza, P. Zanchetta, H. Abu-Rub, H. A. Young, and C. A. Rojas, "State of the Art of Finite Control Set Model Predictive Control in Power Electronics," *IEEE Transactions on Industrial Informatics*, vol. 9, pp. 1003–1016, May 2013.

[38] S. Chai, L. Wang, and E. Rogers, "Model predictive control of a permanent magnet synchronous motor with experimental validation," *Control Engineering Practice*, vol. 21, pp. 1584–1593, Nov. 2013.

[39] P. Cortes, J. Rodriguez, C. Silva, and A. Flores, "Delay Compensation in Model Predictive Current Control of a Three-Phase Inverter," *IEEE Transactions on Industrial Electronics*, vol. 59, pp. 1323–1325, Feb. 2012.

[40] H. Yang, Y. Zhang, N. Zhang, P. D. Walker, and J. Gao, "A voltage sensorless finite control set-model predictive control for three-phase voltage source PWM rectifiers," *Chinese Journal of Electrical Engineering*, vol. 2, pp. 52–59, Dec. 2016.

[41] A. Varatharajan, S. Cruz, H. Hadla, and F. Briz, "Predictive torque control of SynRM drives with online MTPA trajectory tracking and inductances estimation," in *2017 IEEE International Electric Machines and Drives Conference (IEMDC)*, pp. 1–7, May 2017.

[42] P. Niazi and H. A. Toliyat, "On-line parameter estimation of permanent magnet assisted synchronous reluctance motor drives," in *IEEE International Conference on Electric Machines and Drives, 2005.*, pp. 1031–1036, May 2005.

[43] G. Ahmad, H. Tsuyoshi, and T. Teruo, "A novel implementation of low speed sensorless vector control of synchronous reluctance motors with a new online parameter identification approach," in *Twenty-First Annual IEEE Applied Power Electronics Conference and Exposition, 2006. APEC '06.*, pp. 7 pp.–, Mar. 2006.

[44] S. Ichikawa, M. Tomita, S. Doki, and S. Okuma, "Sensorless Control of Synchronous Reluctance Motors Based on Extended EMF Models Considering Magnetic Saturation With Online Parameter Identification," *IEEE Transactions on Industry Applications*, vol. 42, pp. 1264–1274, Sept. 2006.

[45] M. Y. Wei and T. H. Liu, "Design and Implementation of an Online Tuning Adaptive Controller for Synchronous Reluctance Motor Drives," *IEEE Transactions on Industrial Electronics*, vol. 60, pp. 3644–3657, Sept. 2013.

[46] S. Decker, J. Richter, and M. Braun, "Predictive Current Control and Online Parameter Identification of Interior Permanent Magnet Synchronous Machines," in *European Conference on Power Electronics and Applications EPE ECCE Europe*, (Karlsruhe, Germany), Sept. 2016. OCLC: 959604364.

[47] G. Pellegrino, B. Boazzo, and T. M. Jahns, "Magnetic Model Self-Identification for PM Synchronous Machine Drives," *IEEE Transactions on Industry Applications*, vol. 51, pp. 2246–2254, May 2015.

[48] N. Bianchi and S. Bolognani, "Magnetic models of saturated interior permanent magnet motors based on finite element analysis," in *Industry Applications Conference, 1998. Thirty-Third IAS Annual Meeting. The 1998 IEEE*, vol. 1, pp. 27–34, IEEE, 1998.

[49] S. Tahi and R. Ibtiouen, "Finite element calculation of the dq-axes inductances and torque of synchronous reluctance motor," in *Electrical Sciences and Technologies in Maghreb (CISTEM), 2014 International Conference on*, pp. 1–5, IEEE, 2014.

[50] B. Stumberger, G. Stumberger, D. Dolinar, A. Hamler, and M. Trlep, "Evaluation of saturation and cross-magnetization effects in interior permanent-magnet synchronous motor," *IEEE Transactions on Industry Applications*, vol. 39, pp. 1264–1271, Sept. 2003.

[51] M. Morandin and S. Bolognani, "Locked rotor characterization tests of IPM/REL synchronous machine for sensorless drives," in *8th IET International Conference on Power Electronics, Machines and Drives (PEMD 2016)*, pp. 1–6, Apr. 2016.

[52] K. M. Rahman and S. Hiti, "Identification of machine parameters of a synchronous motor," *IEEE Transactions on Industry Applications*, vol. 41, pp. 557–565, Mar. 2005.

[53] Jong-Bin Im, Wonho Kim, Kwangsoo Kim, Chang-Sung Jin, Jae-Hak Choi, and Ju Lee, “Inductance Calculation Method of Synchronous Reluctance Motor Including Iron Loss and Cross Magnetic Saturation,” *IEEE Transactions on Magnetics*, vol. 45, pp. 2803–2806, June 2009.

[54] E. Armando, R. Bojoi, P. Guglielmi, G. Pellegrino, and M. Pastorelli, “Experimental methods for synchronous machines evaluation by an accurate magnetic model identification,” in *Energy Conversion Congress and Exposition (ECCE), 2011 IEEE*, pp. 1744–1749, IEEE, 2011.

[55] N. Bedetti, S. Calligaro, and R. Petrella, “Stand-Still Self-Identification of Flux Characteristics for Synchronous Reluctance Machines Using Novel Saturation Approximating Function and Multiple Linear Regression,” *IEEE Transactions on Industry Applications*, vol. 52, pp. 3083–3092, July 2016.

[56] S. A. Odhano, R. Bojoi, S. G. Rosu, and A. Tenconi, “Identification of the Magnetic Model of Permanent-Magnet Synchronous Machines Using DC-Biased Low-Frequency AC Signal Injection,” *IEEE Transactions on Industry Applications*, vol. 51, pp. 3208–3215, July 2015.

[57] M. Hinkkanen, P. Pescetto, E. Molsa, S. E. Saarakkala, G. Pellegrino, and R. Bojoi, “Sensorless self-commissioning of synchronous reluctance motors at standstill without rotor locking,” *IEEE Transactions on Industry Applications*, pp. 1–1, 2016.

[58] M. Seilmeier and B. Piepenbreier, “Identification of steady-state inductances of PMSM using polynomial representations of the flux surfaces,” in *IECON 2013 - 39th Annual Conference of the IEEE Industrial Electronics Society*, pp. 2899–2904, Nov. 2013.